REPUBLIC OF IRAQ
MINISTRY OF HIGHER EDUCATION AND SCIENTIFIC RESEARCH

AL-FURAT AL-AWSAT TECHNICAL UNIVERSITY
ENGINEERING TECHNICAL COLLEGE NAJAF

PERFORMANCE OF RECTANGULAR SINGLE PASS SOLAR AIR HEATER DUCT USING MULTI-TYPES ARTIFICIAL ROUGHNESS

GHAITH MONEEM FADHALA

M. TECH. MECHANICAL ENG. TECHNIQUES OF POWER

2022

PERFORMANCE OF RECTANGULAR SINGLE PASS SOLAR AIR HEATER DUCT USING MULTI-TYPES ARTIFICIAL ROUGHNESS

A THESIS
SUBMITTED TO THE DEPARTMENT OF MECHANICAL ENGINEERING TECHNIQUES OF POWER
IN PARTIAL FULFILLMENT OF THE REQUIREMENTS FOR MASTER OF THERMAL TECHNOLOGIES DEGREE IN MECHANICAL ENGINEERING TECHNIQUES OF POWER (M.TECH.)

By
GHAITH MONEEM FADHALA

Supervisors

Prof. Dr. AHMED HASHIM YOUSEF

AUG/2022

بسم الله الرحمن الرحيم

(هو الذي جَعَلَ الشَّمْسَ ضِيَاءً والقَمَرَ نوراً وَقَدَّرَه مَنَازِلَ لِتَعْلَموا عَدَدَ السِنِينَ وَالحِسَاب مَا خَلَقَ الله ذلكَ إلاَّ بالحقِّ يفصِّل الآياتِ لِقومٍ يَعْلَمونَ (5)) .

(سورة يونس)

3

Disclaimer

I confirm that the work submitted in this thesis is my work and has not been submitted to other organizations or for any other degree.

Signature:

Name: Ghaith Moneem Fadhala

Date: /   /   2022

Acknowledgment

Supervisor Certification

We certify that the thesis entitled " **Performance of Rectangular Single Pass Solar Air Heater Duct Using Multi-Types Artificial Roughness**" submitted by **Ghaith Moneem Fadhala** has been prepared under our supervision at the Department of Mechanical Engineering Techniques of Power, College of Technical Engineering-Najaf، AL-Furat Al-Awsat Technical University, as partial fulfillment of the requirements for the degree of Master of Techniques in Thermal Engineering.

Signature:

Name: Prof. Dr. Ahmed Hashim Yousef

(Supervisor)

Date: / / 2023

In view of the available recommendation, we forward this thesis for debate by the examining committee.

Signature:

Name: Asst. Prof. Dr. Adel Abd Asis Eidan

Head of power mechanic Tech. Eng. Dept.

Date: / / 2023

III

Committee Report

We certify that we have read the thesis entitled " **Performance of Rectangular Single Pass Solar Air Heater Duct Using Multi-Types Artificial Roughness** " submitted by **Ghaith Moneem Fadhala** and, as examining committee, examined the student's thesis in its contents. In addition, that, in our opinion, it is adequate as a thesis for the degree of Master of Techniques in Thermal Engineering.

Signature:

Name: Prof. Dr. Ahmed Hashim Yousef

(Supervisor)

Date: /   / 2023

Signature: Signature:

Name: Asst. Prof. Dr. Akeel A. Muhammed   Name: Asst. Prof. Dr. Muhammed A. Hussain

(Member)   (Member)

Date: /   / 2023   Date: /   / 2023

Signature:

Name: Riyadh Sabah Saleh

(Chairman)

Date: /   / 2023

Approval of the Engineering Technical College- Najaf Signature:

Signature:

Name: Asst. Prof. Dr. Hassanain Ghani Hameed

Dean of Engineering Technical College- Najaf

Date: /   / 2023

IV

Linguistic Certification

This is to certify that this thesis entitled "**HEAT TRANSFER AND PRESSURE DROP OF RECTANGULAR SOLAR AIR HEATER DUCT USING MULTI-TYPE ARTIFICIAL ROUGHNESS** " was reviewed linguistically. Its language was amended to meet the style of the English language.

Signature:

Name:

Date:

Abstract

Solar energy is one of the most important sources of renewable and sustainable energy, as it is one of the sources of clean and environmentally friendly energy, and the source of solar radiation coming to the earth is one of the most important sources of energy that is inexhaustible. The conversion of this radiation into thermal energy and its exploitation in the energy needs of the earth, as the solar air heater is the solar system is one of the important applications in this field.

The thermal performance of a single-pass solar air heater was studied in the presence and absence of artificial roughness experimental and numerically using the ANSYS FLUENT version 17 program. It was arranged inline and staggered to find the best type and the best arrangement.

The duct was designed with dimensions (length * width * height) (2.1* 0.3*0.03) m. Within the Reynolds number range (3000-10000) (3323,5545,7393, and 9241) and by the amount and angle of attack $\alpha = 60 \circ$. The relative roughness length (d/H = 1.33), the relative roughness height (e/H = 0.271), the distance between S (b/H = 0.667) remain constant, and the pitch range p/H= (1.667,3.33,5,6.667) for inline with l/ H=(0.8335, 1.666, 2.5, and 3.335) for staggered and study the effect of the p/H of the arrangement inline and the l/H of the staggered arrangement.

In the numerical study, the ANSYS FLUENT version 17 program was used to simulate the air solar heater within the simple algorithm (SIMPLE) using the method of finite volumes to solve the three-dimensional equations (continuity, energy, momentum) in addition to the equations of the disturbance model (k-ε) and within the same boundary conditions used in experimental side.

Experimental were conducted in the free atmosphere under the sun's rays after building a model of a device that measures the flow and resistance temperatures. The results, with the numerical aspect, were largely identical.

The results showed that the Nusselt number increases with the increase of the Reynolds number, and the friction factor decreases with the increase of the Reynolds number. The best Nusselt number Nu/Nus=7.8 was obtained at l/H=1.667 in the arc shape in successive order, and the coefficient of friction was f/fs=3.8. The thermal performance factor of this arrangement is the best by 3.67 with an efficiency of 74.5%.

Contents

VIII

X

List of figures

XIII

XIV

List of Table

Nomenclature

Symbol	Description	Unit
As	The heat transfer surface area	m²
Ap	The surface area of absorber plate	m²
C_p	Coefficient of specific heat	J/kg .K
e	Rib height	mm
f	Friction factor	-
fs	Friction factor of smooth surface	-
H	Height	mm
h	Heat transfer coefficients	W/m².k
I	Intensity of solar radiation	W/m²

k	Thermal conductivity	W/m.k
L	Length	mm
$\dot{m}$	Mass flow rate	Kg/s
Nu	Nusselt number	-
Nus	Nusselt number of smooth surface	-
p	Pitch	mm
Pr	Prantel number	-
Qu	Useful heat gain	W
Re	Reynolds number	-
TPF	Thermal performance factor	-
T_i	Temperature of the Inlet	K
T_p	Temperature of plate	K
T_{pm}	Mean plate temperature	K
T_o	Temperature of the outlet	K
T_m	The mean temperature $(\frac{T_o + T_i}{2})$	K
W	Width	mm
Greek Symbols		
ρ	Fluid density	kg/m^3
μ	Dynamic viscosity	Pa.s
α	Angle of attack	°
ε	Effectiveness	-
Δp	pressure drop	bar

Abbreviation

symbol	Description
d/H	Length of the relative roughness
e/H	Height of the relative roughness
b/H	Distance between arc shape
p/H	Relative roughness pitch
l/H	Relative roughness length
P/e	Relative roughness pitch
W/w	Relative roughness width
e/D_h	Height of the relative roughness
p/w	Pitch ratio
x/L	Position of the element of contours in duct
SAH	Solar air heater
SP-SAH	Single pass solar air heater
SRVG	S-shape rectangular vortex generator
ARVG	Arc-shape rectangular vortex generator

Chapter One
Introduction

CHAPTER ONE

Introduction

Energy is the primary resource for industrial development and economic growth in every country throughout the globe. Manufacturing uses around 35% of the world's total energy supply. The current predicament is exacerbated by the exponential rise in the usage of fossil fuels[1], which in turn increases pollution levels in the natural world. In comparison to recent years, demand for gasoline is anticipated to increase by a factor of three by 2025. Demand for fossil fuels continues to rise at a faster clip than supply can keep up with. Oil, along with other fossil fuels, is the primary supply of energy for businesses. Because of this, reducing energy use is crucial for both economic and ecological reasons[2][3].

The sun's rays are a clean, renewable source of energy that will never run out[4]. Solar energy may be transferred in the form of thermal energy in a straightforward manner by using solar air heaters . Because of their inexpensive price and easy installation, SAHs have grown in popularity as a type of solar thermal technology. The absorber plate takes up both direct and diffuse solar radiations, transferring their energy to the air passing below. Solar air heaters' effectiveness in generating heat is proportional to the amount of energy the collector fluid contributes to the system. Since air has a relatively poor heat transfer coefficient, a greater proportion of the energy produced is lost to the environment. Laminar viscous sub-layer development over a hot surface is thought to provide thermal resistance to heat transmission. Any passive strategy for improving heat transmission relies on employing surfaces with a certain degree of irregularity to provide turbulence in the flow. Creating artificial roughness in the shape of ribs, grooves, dimples, winglets, baffles, twisted tapes, mesh wires, etc. on the bottom of the absorber plate etc. [5][6]. Is a common passive method of improving heat transfer. Increasing convective heat transmission is the major goal of adopting artificial roughness.

1.1 Solar Energy

Solar energy is an enormous and infinite energy source. The quantity of solar energy received by the earth is around $(1.8x10^{11}$ MW)[7], This is hundreds of times more than its current pace of industrial energy use Solar energy has the potential to provide all of the world's current and future energy needs, making it one of the most promising alternative energy sources. Solar energy benefits from two more elements in addition to its size. It is the most environmentally benign form of energy when compared to fossil fuels and nuclear power. Second, it is available for free and in sufficient quantities in practically all inhabited regions on the planet. However, its use is fraught with complications. The primary concern is that it is a source of low energy. In many applications, large collecting surfaces are necessary, resulting in expensive expenses. A second challenge linked with solar energy consumption is its changing availability throughout time. Daily and seasonal changes in availability are caused by the day-night cycle and the earth's orbit around the sun. [8] Moreover, variations result from the local weather conditions at a particular location. Therefore, it is necessary to store solar energy for usage when the sun is not shining. The necessity for storage significantly increases the cost of any system[9].

1.2 Solar radiation

The sun is a sphere of extremely hot, gaseous matter with a diameter of $(1.39 \ x10^9$ m) at an average distance from Earth of $(1.5x10^{11}$ m) [7]. The sun rotates on its axis every four weeks as seen from Earth. It does not, however, spin like a solid body; the equator rotates every 27 days, while the polar parts revolve every 30 days. The sun's constituent gases comprise a continuous fusion reactor. The distribution of sun irradiation on Earth is seen in Figure (1-1). Solar spectral radiation is the wavelength-dependent energy that enters the earth's upper atmosphere and is refracted into visible light by an electromagnetic short-wave absorber[9].
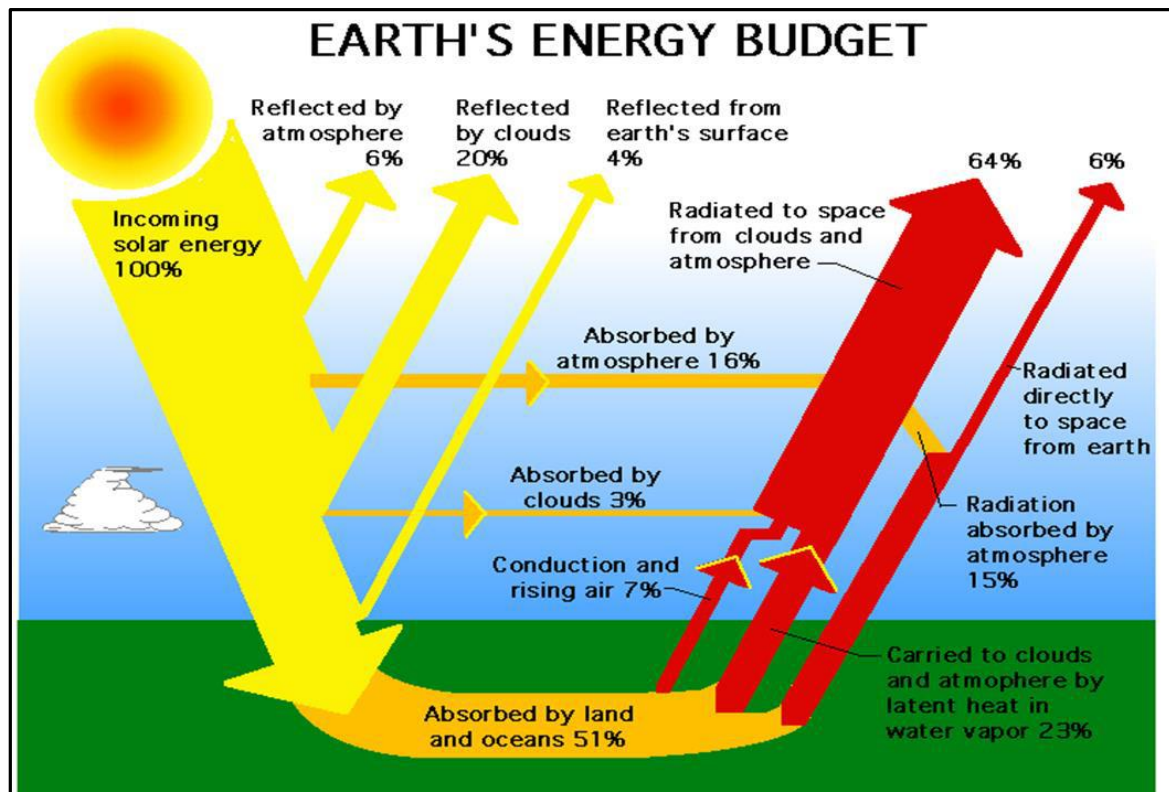
Figure (1-1): Distribution radiation from the sun on Earth's surface [9].

1.3 Flat plate- solar heater

Solar air heaters are the most common thermal devices used to transform solar energy into a useable form. Solar air heaters (SAHs) are chosen over solar water heaters (SWHs) due to their applicability in many technical applications. SAHs are safe to use since they are devoid of filth, corrosion and leakage issues, and they are easy to construct. Conventional SAHs are composed of a smooth, insulated duct through which air absorbs solar energy. Along the collection duct, the air's temperature increases. This gas is utilized in many of the aforementioned technical applications. Plate for heat absorption and back plate. The poor heat tolerance of air, despite its many benefits, limits the use of SAHs in high-temperature operations. [10].

1.3.1 Solar air heaters types

Solar collectors are utilized for thermal conversion to increase the temperature of the fluid that flows through the collector. Water and air are the most widely utilized fluids in solar collectors. Due primarily to the low heat transfer coefficient between the absorber plate and the air passing through the collector, SAH fall into two primary categories: The first segment is contingent on the design of the absorbent surface of the flat plate to maximize the convection area and the turbulence of the airflow with the black plate. The thermal efficiency can be enhanced by the use of artificial roughness. See Figure (1-2a). The number of passageways and the kind of airflow pattern categorizes the second portion. In addition to an optimum design for minimizing losses to the environment. As seen in Figure (1-2b)[11].

There are several flat-plate solar collector designs. The most prevalent varieties are listed below.

❖ Active and passive solar collectors are the two categories of solar energy systems that are available. Passive solar energy is the collection of heat and light; for example, the passive design uses solar energy to increase the energy efficiency of a variety of buildings by reducing the demand for day illumination and the amount of energy required for heating and ventilation. Active solar energy refers to the storage and transformation of this energy into other forms, such as PV electricity or thermal energy [12].

❖ Fins, corrugated, Flat, or grooved collector absorbing plates ,etc. The plate can be combined with the obstructions.

❖ Collectors intended to limit heat losses can be categorized according to the number of covers they can accommodate one , two , or more. Increasing the number of covers decreases heat losses from the cover, but transmits less solar energy to the absorber plate.

❖ As it can transmit up to 90 percent of the incoming shortwave solar irradiance while transmitting almost none of the longwave radiation generated by the absorber plate, glass is commonly employed for glazing solar collectors.
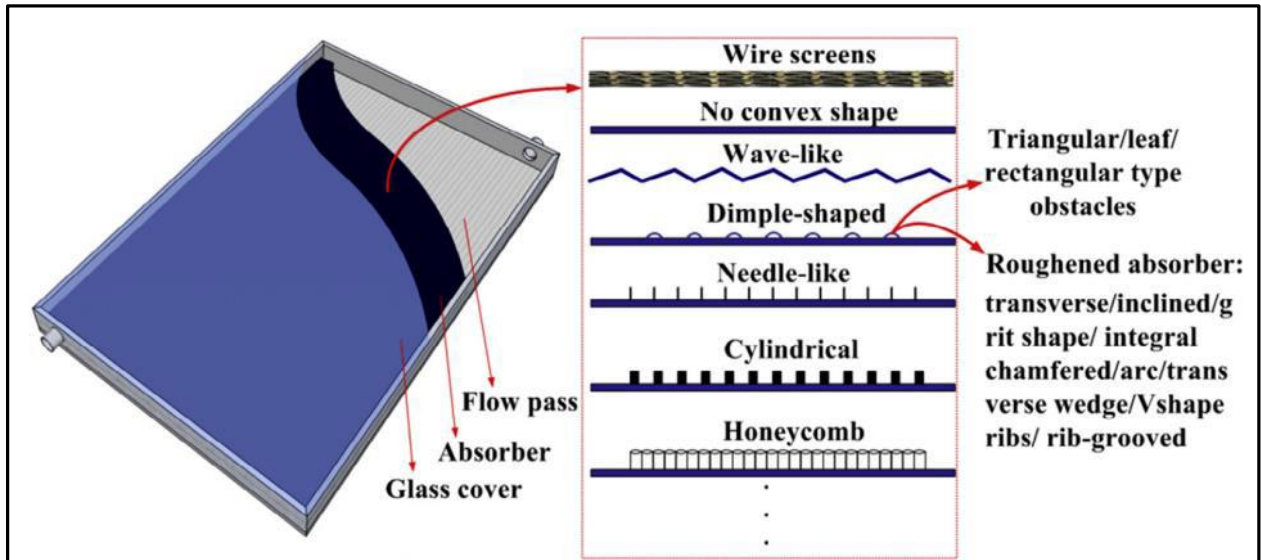
(a)
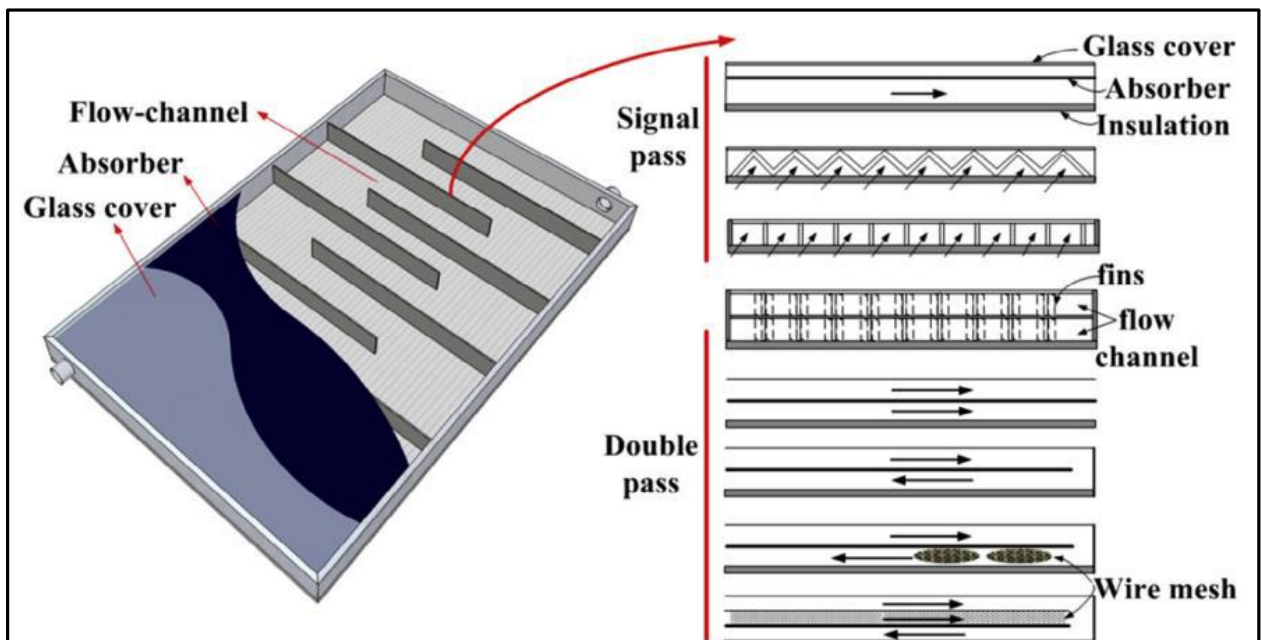
(b)

Figure (1-2) Flat plate-SAHs configurations:(a) Absorber surface design, and(b) Channel flow patterns[11].

SAHs can be classified based on the mode[13], as shown in the Figure below:
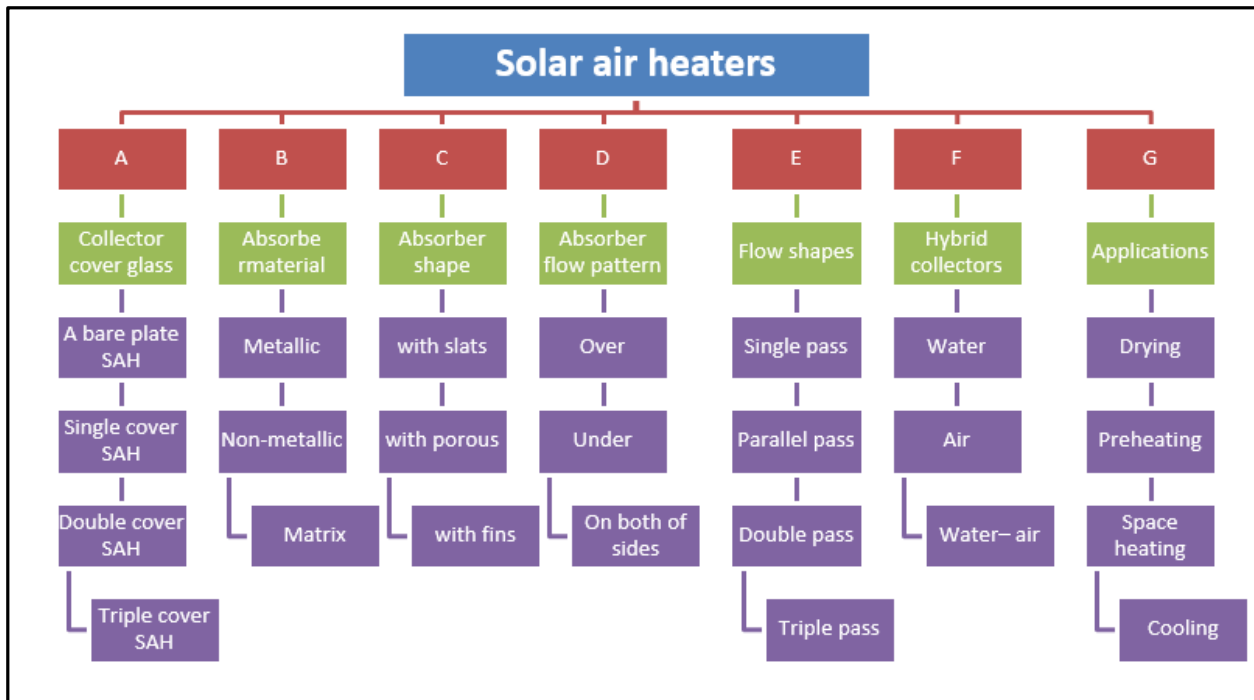
Figure (1-3): Classification of SAHs.

1.3.2 Components of solar air collector

Figure (1-4) illustrates the components of a conventional SAHs, which are described below[7].

1. Glass cover: As it can transmit up to 90 percent of the short-wavelength solar irradiance, one or more sheets of glass are typically employed for glazing solar collectors.

2. Fluid passageway : fins , tubes , or channels that convey or guide the heat transfer stream from intake to output.

3. Absorber plate: This absorber sheet may be grooved, undulating, or flat.

4. Insulation: minimizing heat loss via the sides and base.

5. Container: All collecting components are shielded from environmental harm, such as moisture and dust.
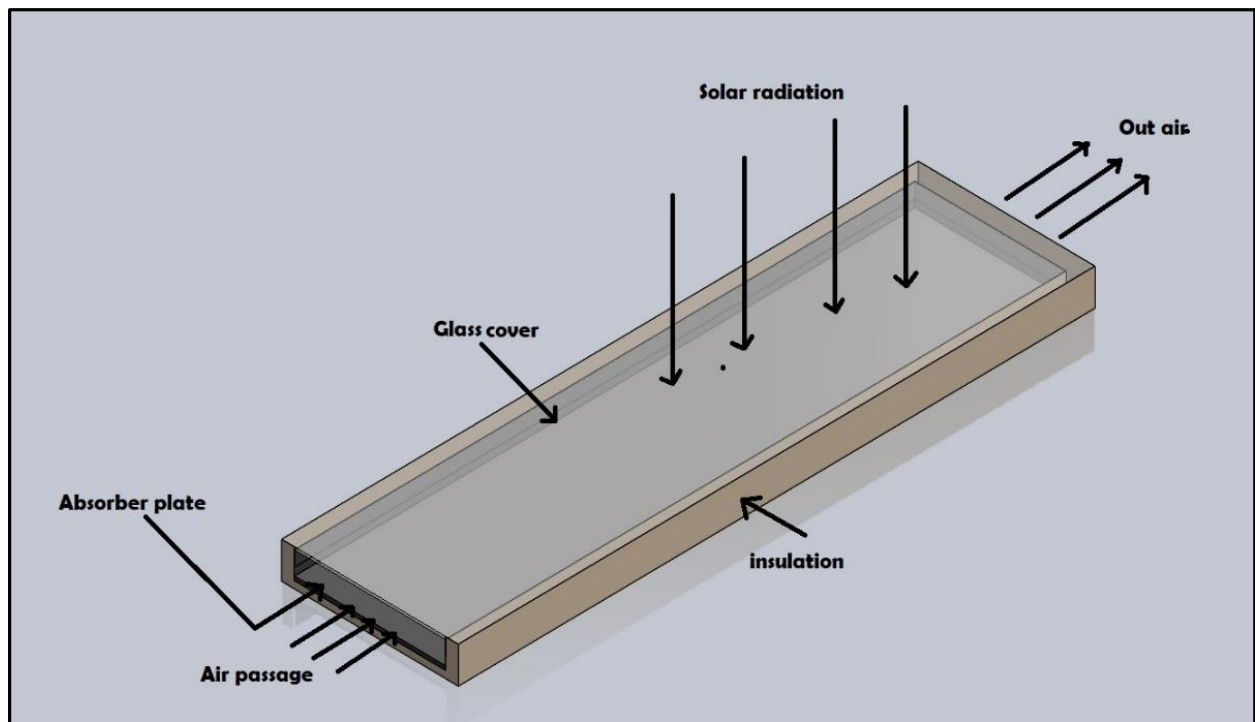
Figure (1-4) component of conventional SAHs

1.4 Problem statement

As stated previously, solar air heating is one application of renewable energy.

➢ The low heat transfer coefficient between the absorber plate and the flowing air creates high thermal resistance in the airside and high absorber plate temperature, hence diminishing the SAH's energy conversion efficiency. Therefore, it is vital to optimize the heat transfer performance in the SAH duct in order to increase energy and efficiency.

➢ One of the most promising methods for the enhancement of heat transfer rate, which has been proposed recently, is the artificial roughness technique.

➢ The use of artificial roughness in the test area on the absorbent plate leads to the formation of turbulent flow that increases heat transfer.

1.5 Objective of the work

The specific aims of this thesis may be summed up in two sections as follows:

(I)   Experimental approach

The purpose of the study is to increase heat transfer to the moving fluid by strategically positioning two types of impediments and flow vectors to achieve the maximum amount of heat transfer while minimizing losses to the greatest extent feasible. The research will be applicable. In addition, we employ two forms of surface roughness (S shape and arc shape) and two ways of arrangement for these shapes (inline and staggered).

a) Manufacture and testing of a SP-SAH in outdoor environments with and without artificial roughness using a solar simulator.

b) Examining how particular factors, such as solar flow density and airflow rate, influence the increase in air temperature and the effective thermal efficiency of a single pass-SAH with and without artificial roughness.

(II)   Numerical Approach

The investigation will be conducted numerically using the simulation software Ansys Fluent version 17.0. For the actual experiment, the same conditions will be employed. To compare numerical findings to experimental results and to obtain optimal convergence and accurate outcomes.

Chapter Two
Literature review

Chapter Two

Introduction

This chapter presents a group of experimental and numerical studies that have improved the low coefficient heat transfer for solar air heaters using artificial roughness, as present address studies using the artificial roughness rib and vortex generators, as well as ailerons and fins, etc.

2.1 Studies on the artificial roughness of rib

Many investigations depend on the design of roughness that helps boost heat transfer with minimal pressure loss.

Sahu et al.[14] experimental, study on, the heat, transfer rate and friction, factor, of SAH using artificial, roughness, in the form of broken ribs at $\alpha = 90^\circ$. The roughness wall has roughness with pitch (P) ranging from 10-30 mm, height of rib of 1.5 mm and aspect ratio w/h = 8 with a value of Re= 3000-12000 where the value of Nu was found, at, p = 20 mm and the maximum thermal efficiency was obtained by 83.5%.

Saini et al.[15] Experimental investigation presented to study the rate of heat transfer and the f for SAH. Using an artificial roughness in the form of dimples that leans on the absorbent plate with parameters of e /D_h = 0.018-0.037, p / e = 8 to 12 and Re = 2000-12000 where Nu was chosen with the change of parameters and found that the highest value at e / D_h = 0.037, p / e = 10 and frication factor at e/D_h = 0.0289.

Alam et al.[16] The researchers investigated the number of SAH, that stands out with the sides of the conical protrusion on the Nu and the friction factor with different parameters of Re=(4000-16000). By conducting a numerical simulation using the program of the solar intensity of 1000 W / m^2, where at

e /D_h = 0.0289, p/e = 10. Thermal efficiency are found as 69.8% and enhancement factor 1.346%. As shown in figure (2-1).
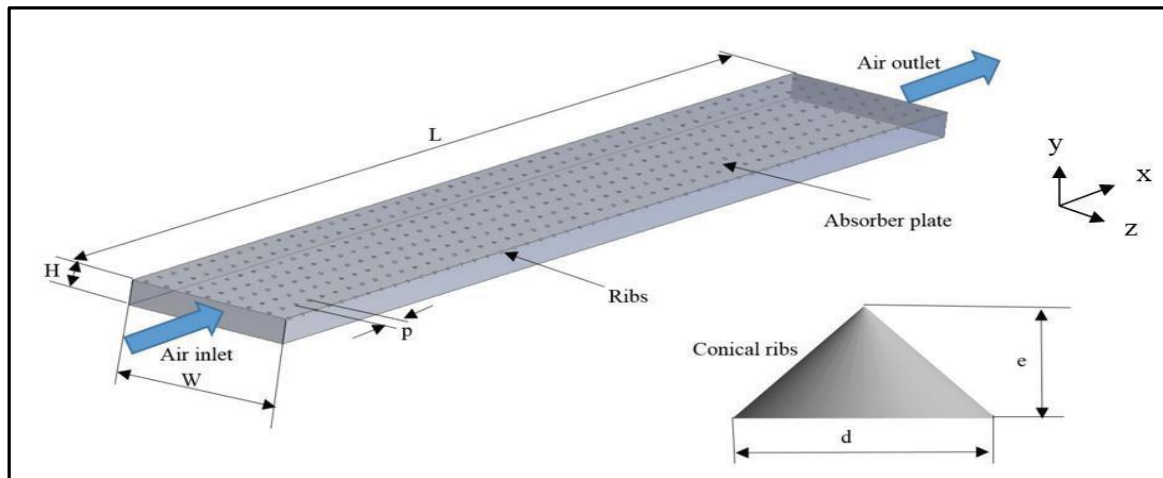
Figure (2-1): Geometry artificial roughness[16]

Ghritlahre et al.[17] illustrates experimental study to shown the effect of using the arc shape of the shadow on the performance of the SAH with a practical achievement and the rate of heat transfer, as he used a wire under the curved arc in the form of an arc. p/e = 10 parameters were used and attractive angle α = 60° and e / D_h = 0.039 where the best thermal performance at the level of solar Intensity 853.3 W/m² is for upstream apex = 72.2% and for down apex = 63.1% compared to smooth.

2.2 Studies using Fins and Baffles / Vortex Generators

Zhou et al. [18] Experimental work present performance of SAH and characteristics of heat transfer by using curved trapezoidal winglet type vortex generators with parameters α=20° , $\beta = 0° - 15°$,b/a=1/2 , and Re=3000-27000. They found the ratio of Nu=2.56 and f=3.18 was obtained when using parameters $\beta = 0°, α = 20°, Re = 18000$.Where the thermal-hydraulic performance was highest 1.3 at Reynolds No. 18000 As shown in figure (2-2).
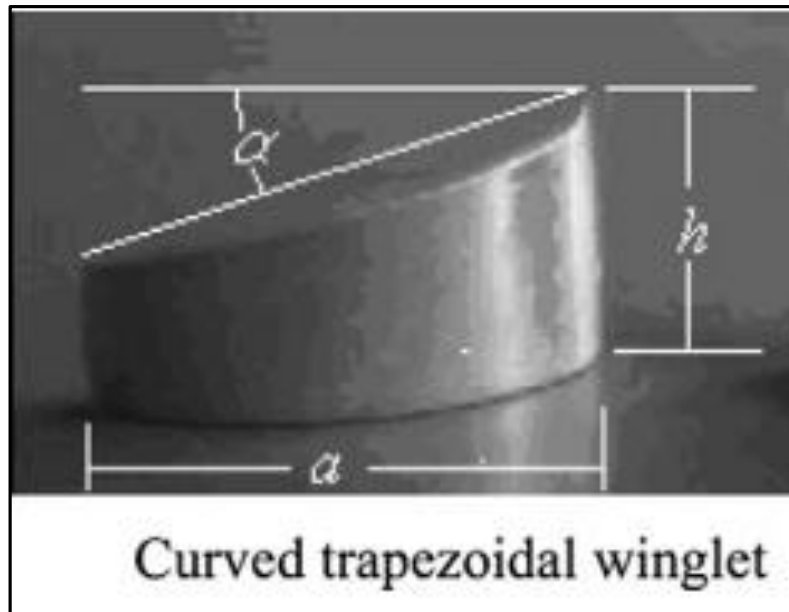
Figure (2-2): Curved trapezoidal winglet type vortex generators [18]

Yadav et al. [19] Numerical investigation present using square sectioned transverse rib roughness on absorber plate of solar air heater to study performance and flow characteristic with parameters e/D_h = 0.02-0.042 , $p/e = 7.14 - 35.7$, α= 60°, and Re = 3800-18000 that found The best optimization of the Nusselt number was obtained at parameters p/e = 7-17,e/D_h=0.042, Nu = 2.860. as shown in figure (2-3).

Figure (2-3): Square transverse ribs[19]

kumar et al.[20] The researcher presented an experimental and numerical investigation to study the effect of using sinusoidal corrugated artificial roughness as shown in figure (2-18) with parameters of Re= 4000-15000, p/e=10-18, e=1mm on thermal performance and heat transfer coefficient. These parameters found that the thermal performance factor is 2.05.

Figure (2-18): Sinusoidal corrugated artificial roughness[20]

Chabane et al.[21] Experimental study of heat transfer and thermal performance was conducted on the use of a longitudinal fin on a solar air heater and its effect on the heat transfer coefficient , as it was discovered that at a mass flow rate of (0.012-0.016) kg/s, The values of thermal efficiency at the mass flow rate of 0.012 and 0.016 kg/ s with and without using fins varied from 40.02% to 51.50% and from 34.92% to 43.94%, respectively. As shown in figure (2-4).
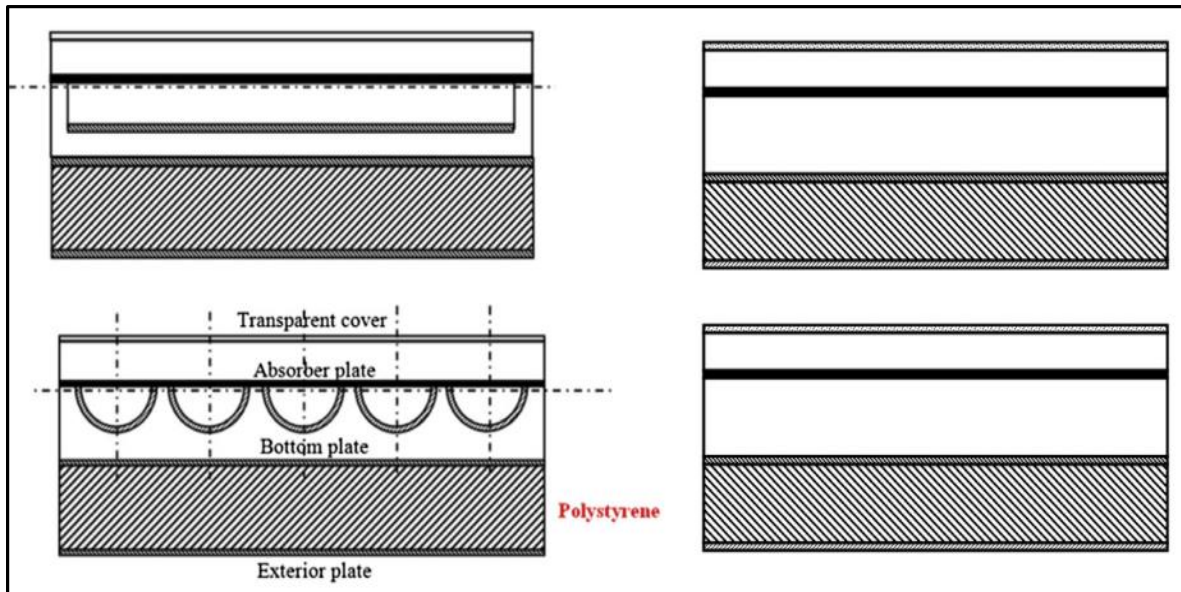
Figure (2-4) longitudinal fin on a solar air heater. [21]

Skullong et al.[22] illustrates negative ways of enhancing heat transfer SAH is artificial roughness, and one of the things that enter into the calculation of artificial roughness is the effect of the size of the ribs and their arrangement on heat transfer as shown in figure (2-5). Therefore, the research presented a practical investigation on the effect of the size and arrangement of the ribs for a SAH with the parameters of Re=5000-24000 where it was used square and thin ribs 90° with three arrangements that shows the effect of these parameters on heat transfer and friction losses on a smooth surface. was obtained that the inline rib array provides the maximal heat transfer while staggered thin ribs show the highest thermal improvement factor whereby obtained Nu/Nu_o=2.13 - 2.16.
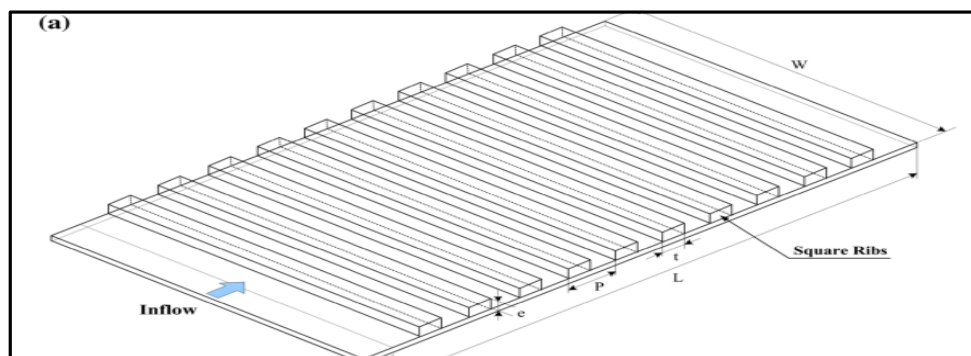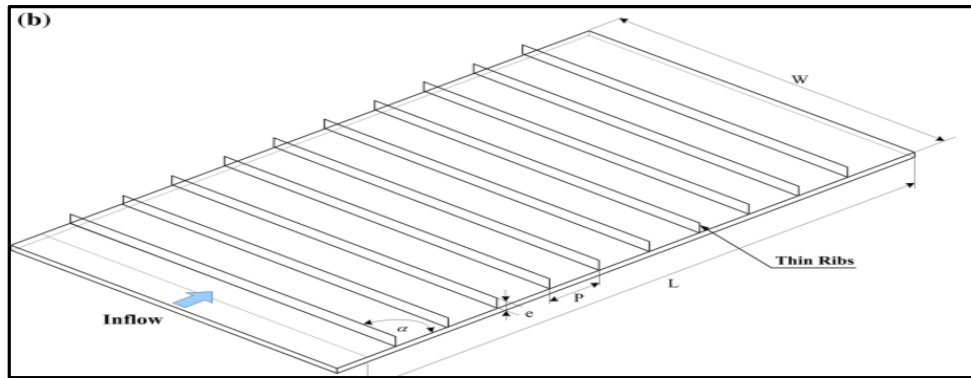
Figure (2-5): (a) Square and (b) Thin ribs 90 º artificial roughness[22]

Skullong et al.[23] An experimental investigation on thermal performance improvement in a solar air heater channel with combined wavy-groove and delta-wing vortex generator (WVG) placed on the absorber plate having a uniform wall heat-flux is carried out. With parameter as $g/h = 0.4\text{-}1$, $\alpha = 45°\text{-}60°$, and $Re = 4800\text{-}23000$. A thermal improvement factor of 2.24 is obtained when such a coarseness is used with a ratio $Nu/Nuo = 5.74$, $f/fo = 17.01$. as shown in figure (2-6).
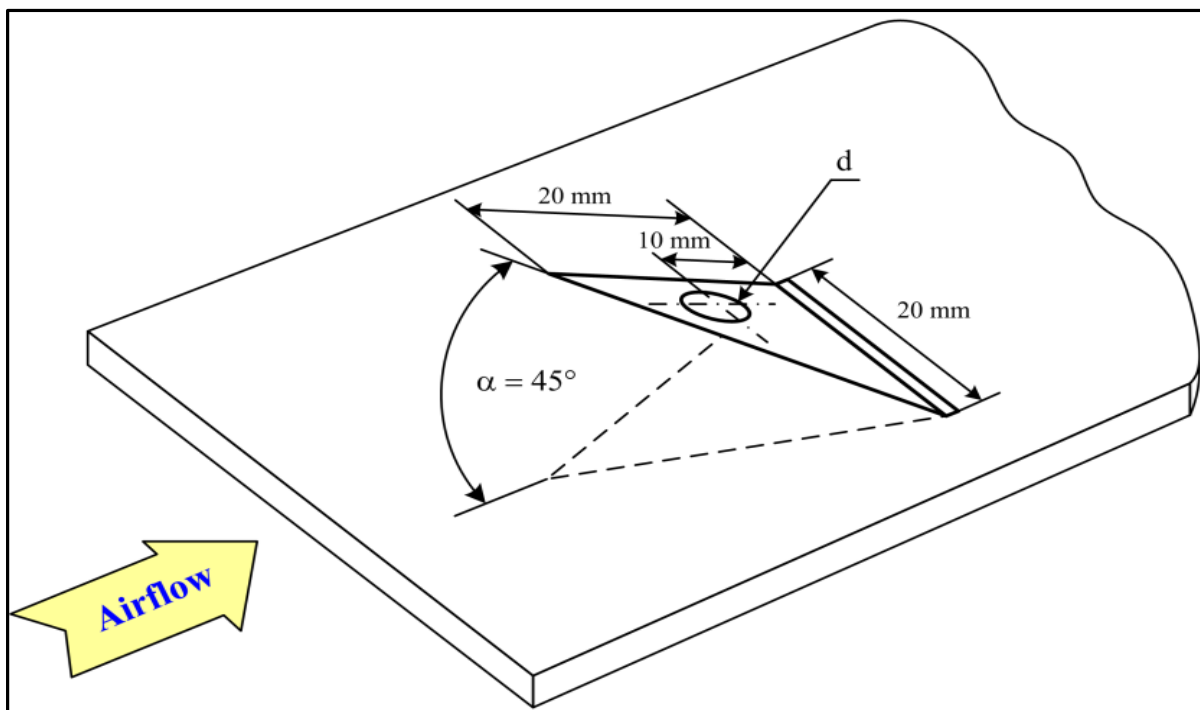
Figure (2-6): Wavy groove combined with perforated delta wing. [23]

Singh et al. [24] The present study investigates the heat transfer and pressure drop characteristics of a two-pass channel (AR = 1) featuring ribs-alone, dimples-alone and combination of ribs and dimples. using V-shape cylindrical dimples as shown in figures (2-7). For parameters of Reynolds number ranging from 19500-69000, e/D_h=0.125, P/e=16, where they found the thermal performance factor equal to 1.65.
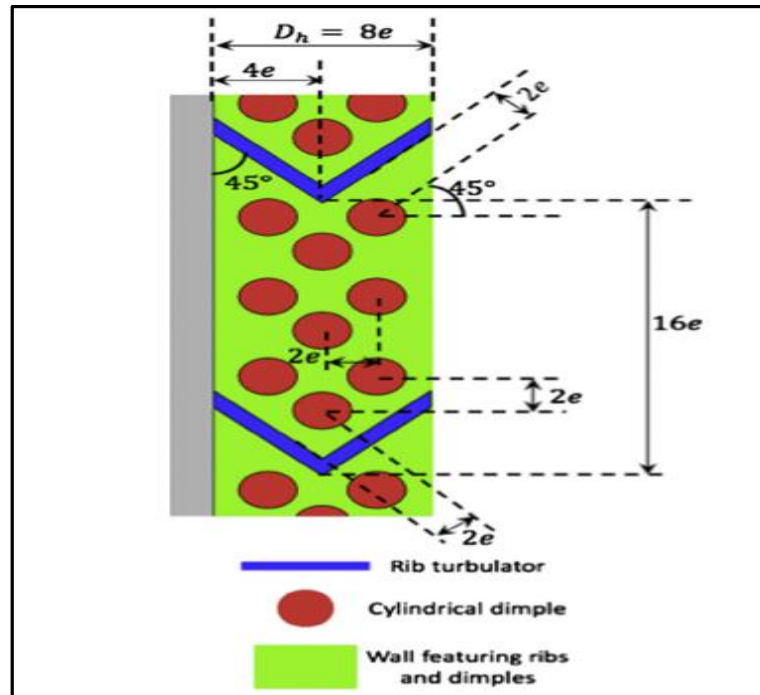
Figure (2-7): Geometry artificial of cylindrical dimples[24]

Grill et al.[25] Numerical investigations on thermo-hydraulic performance of broken arc rib in a rectangular duct of solar air heater. The rib parameters were P/e = 8, d/w = 0.65, g/e = 1.0, α/90 = 0.333, and e/D$_h$ = 0.043. And study at Reynolds number 2000–16000. The highest thermos-hydraulic performance parameter achieved was 1.94 at 0.65 relative gap position, as compared to 1.78 for continuous arc rib roughened duct. As shown in figure (2-8).
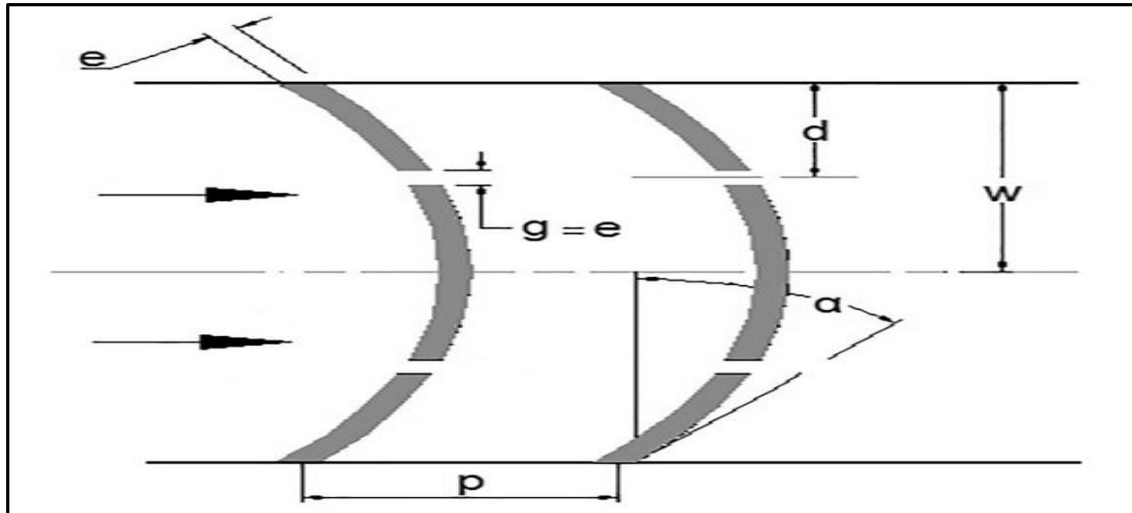
Figure (2-8): Broken arc rib. [25]

Singh et al.[26] CFD analysis of solar air heater duct having square wave profiled transverse ribs as roughness elements ribs have parameter as $p/e = 4 \, to \, 30$, Re=3000-15000, and $e/D = 0.042$. The Nusselt number and the friction factor (f) are improved when using this form of synthetic roughness $Nu = 2.14, f = 3.55$. as shown in figure (2-9).
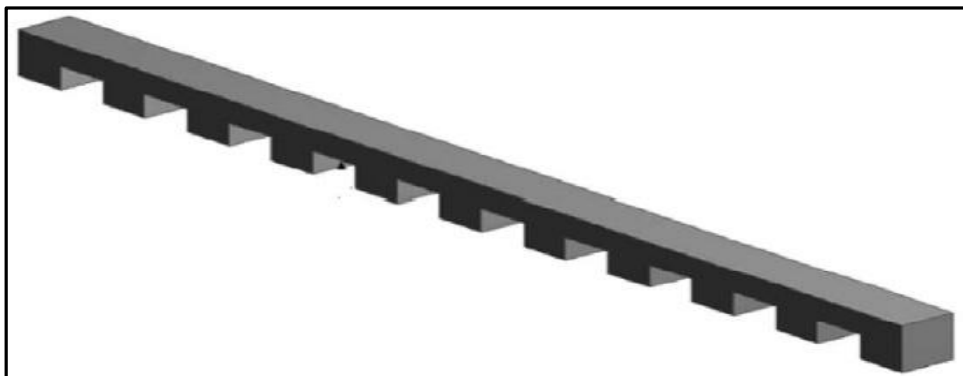
Figure (2-9): square wave profiled transverse ribs. [26]

Kumar et al.[27] Experimental investigation to enhance the heat transfer
of SAH   using   artificial   roughness . The researcher presents using twisted
roughness on the solar radiation plate as shown in figure (2-10) with parameters
of Re = 3500-21000, p / e = 8, and different values of α= 30º - 90º and the twisting
rate is y / e = 3 to 7. The practical experiment demonstrated an increase in the
heat transfer coefficient compared to smooth surface so, at p / e = 8, α = 60º,
and y / e = 3 they get ratio of Nu and the friction factor (2.46, 1.78) respectively.
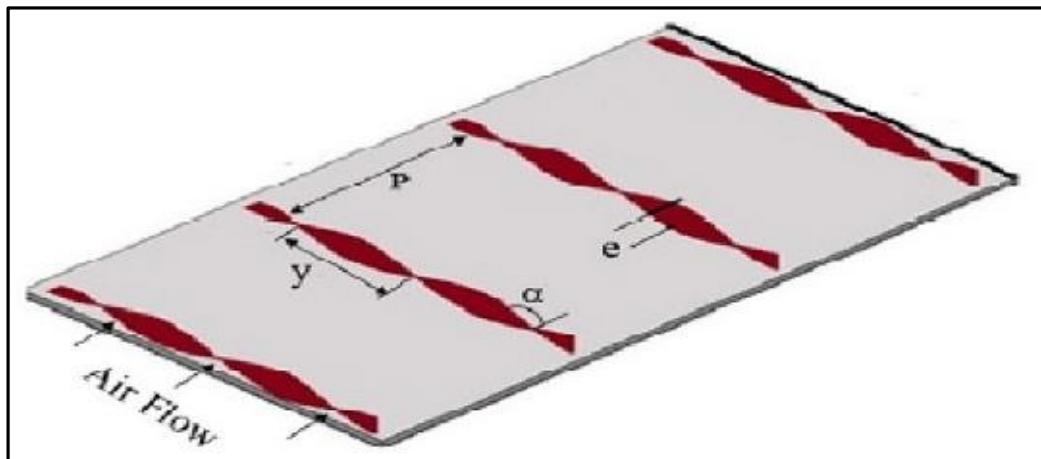
Figure (2-10): Twisted roughness[27]

Promvonge et al.[28] An experimental work has been carried out to
investigate the influence of combined turbulence promoters (or turbulators) on
forced convection and fluid flow resistance behaviors in a solar air heater duct.
Two turbulators included V-ribs with punched holes and chamfered V-grooves
were introduced. The V-rib and the V-groove having the attack angle of 45 were
mounted repeatedly on the absorber plate with their arrangements for V-tip
pointing upstream and pointing downstream. Air as the test fluid flowed into the
duct with Reynolds number (Re) ranging from 5300 to 23,000. The rib parameters
were three relative rib-pitches (RP = 1.0, 1.5 and 2.0), three inclination angles (b
= 45º, 0º, and -45º) of rib punched holes having a single relative rib height or
blockage ratio, RB = 0.5. The groove parameters included three relative groove-

20

pitch lengths (RP = 1.0, 1.5 and 2.0) similar to the V-rib case. The highest TPF of about 2.47. As shown in figure (2-11).
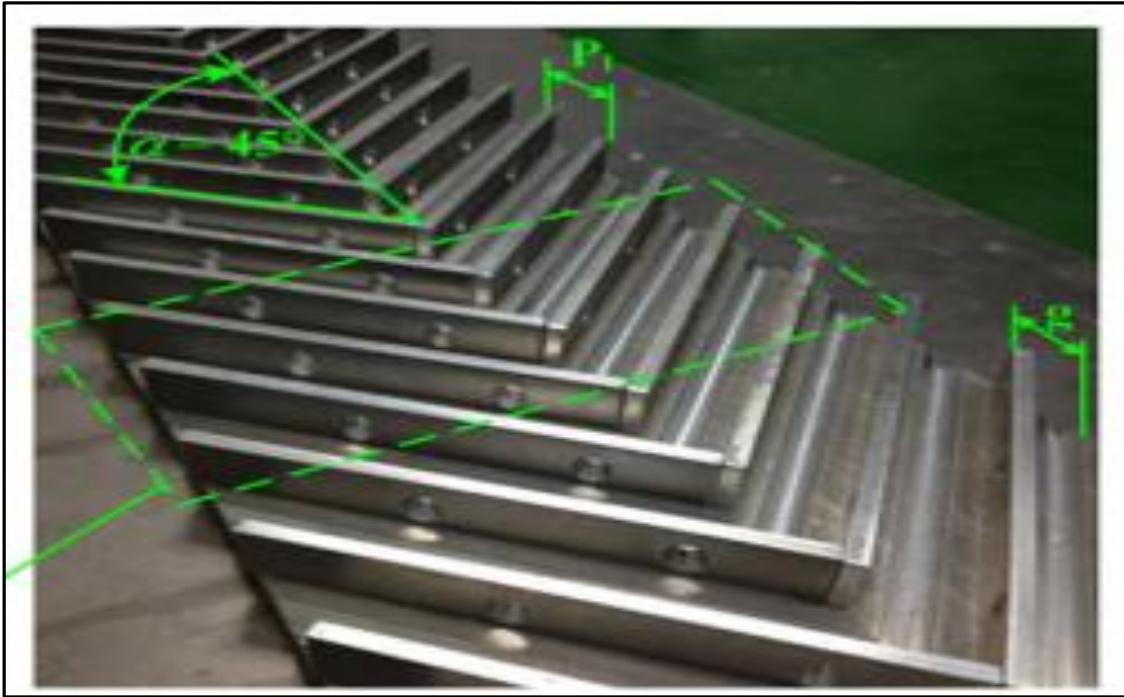
Figure (2-11): Combined punched V-ribs chamfer V-grooves. [28]

Tongyote et al.[29] An experimental work has been conducted to explore the influence of the combined V-rib and chamfered-V-groove vortex generator (VG) on flow and heat transfer behaviors in a heat exchanger channel having a constant heat-flux on the top wall. The investigated geometrical parameters were three relative rib pitches (RP = P/H =1.0, 1.5 and 2.0) and relative rib heights (called "blockage ratio", RB=e/H=0.3, 0.4 and 0.5) at a single attack angle (α =45°), and Re=5300-23000. The highest TPF= 1.907 that obtained at parameter p/H=1.5, e/H=0.4. As shown figure (2-12).
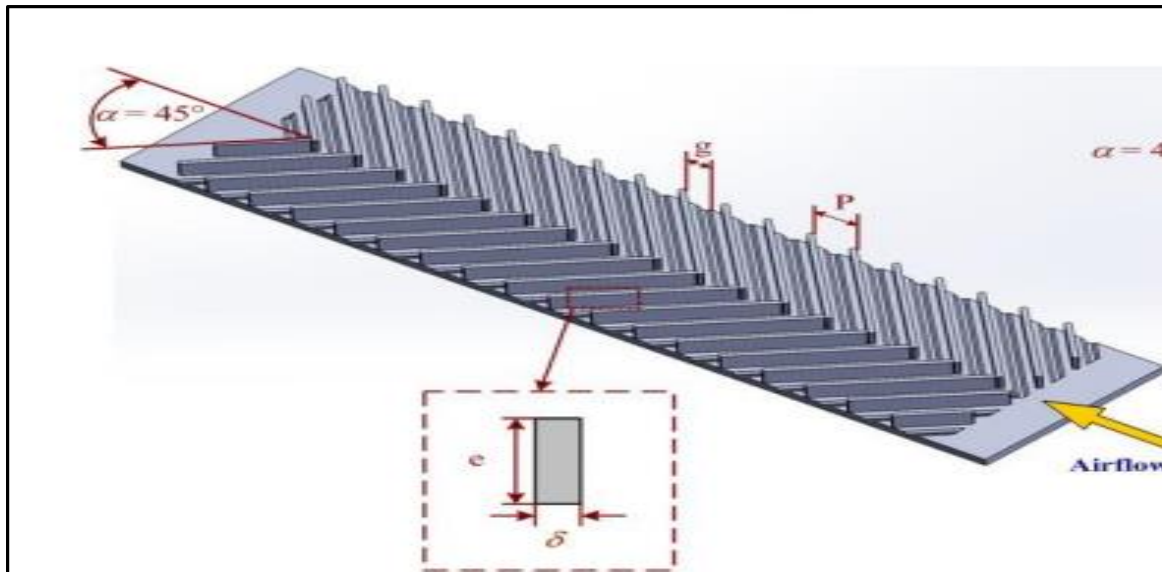
Figure (2-12): V-shaped ribs and grooves. [29]

A khanlari et al.[30] Experimental and numerical study of the effect of integrating plus-shaped perforated baffles to solar air collector in drying application to investigate the rate of heat transfer heat performance of SAH. using baffles in three forms PPSCDB (parallel pass solar collector with double baffles), with baffles, and without baffles where it was found at a mass flow rate of 0.011 kg / s , thermal efficiencies of PPSC, PPSCB and PPSCDB are in the range of 62.10-66.32%, 65.72-69.62% and 71.12-75.11%, respectively. as shown in figure (2-13).
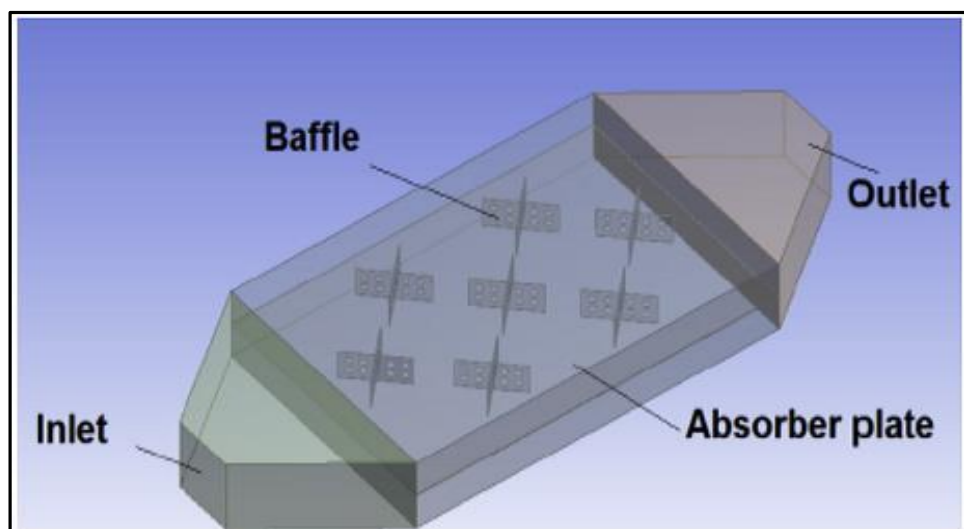
Figure (2-13): Geometry artificial roughness baffles[30]

Bayralcu et al.[31] Numerical and experimental study of the heat transfer and hydraulic performance of solar air heaters with different baffle positions. The numerical study was performed on four cases corresponding to different placements of baffles with Reynolds numbers ranging from 2370 to 8340. Although the highest Nusselt number value obtained was 70 in case 4 (Re = 8340), it produces a great pressure drop, while the lowest friction factor values were found to be 0.05 for cases 1, 2 and 3, with nearly identical values (Re = 8340). Case 2 (50%Down) has been selected as the best configuration and an effective baffle position from the point of view of thermo-hydraulic performance.

Wang et al.[32] When using artificial roughness to increase thermal efficiency and improve the thermal performance of SAH. The researcher experimented with an internal process using the S-shaped with a gap as shown in figure (2-14) with parameters of Re= 2000-20000, p /e=20-30, e / D = 0.023-0.036, and under solar radiation intensity (450-650W/m^2).The optimization of thermal efficiency increased by (13% - 48%)compared to the smooth channel under different conditions.
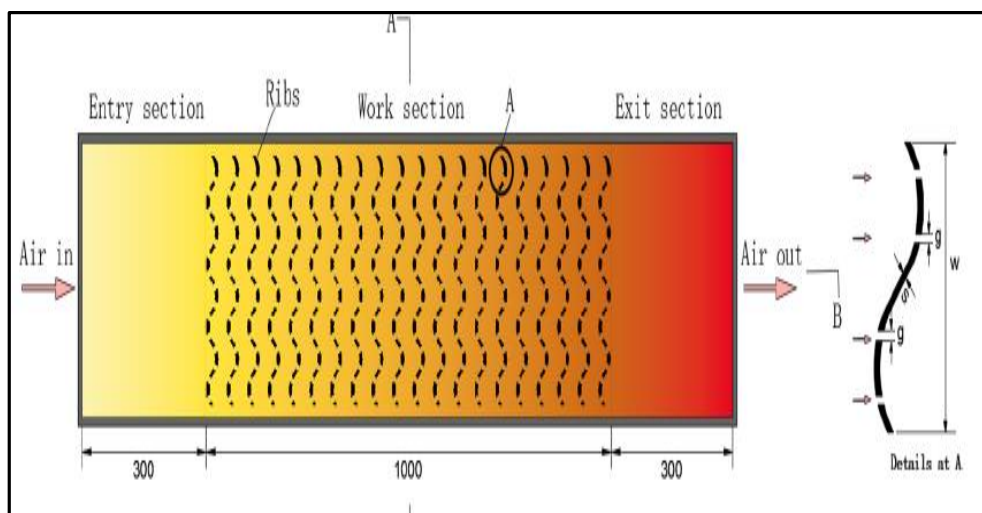
Figure (2-14): S-shaped with a gap artificial roughness[32]

  Baissi et al.[33] Illustrates the techniques of enhance heat transfer and thermal performance of SAH by use of artificial roughness. Here, the researcher shows when using roughness in the form of barriers in the form of a longitudinal delta that used two cases of barriers with holes and barriers without holes as shown in figures (2-15). With different parameters, Re= 2500-12000, p / e = 3-5, e / h = 0.8, α = 45° through these parameters, improvement was obtained in Nu and an increase in heat transfer and hypotension as Nu = 6.94, f = 45.83 compared to the smooth channel and the highest thermal improvement factor 2.26.
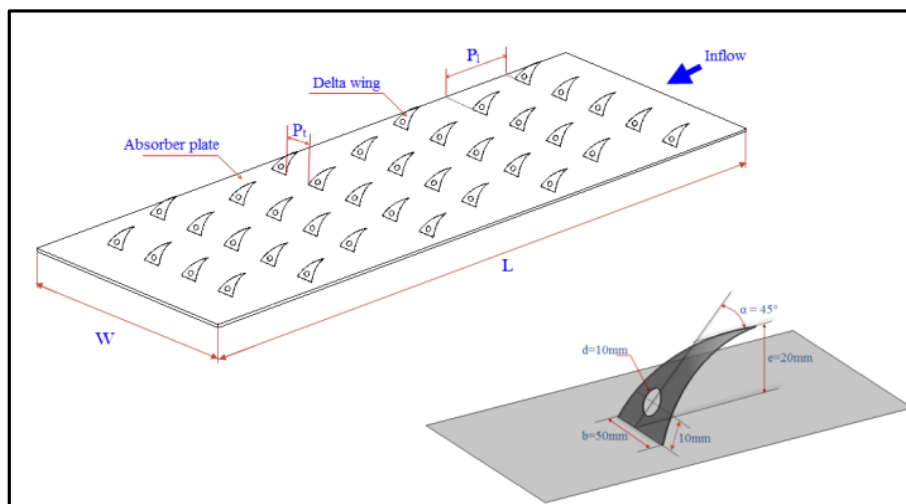
Figure (2-15): Longitudinal delta baffles shaped[33]

Mahanand et al.[34] Numerical investigation the heat transfers and flow fields analysis in solar air heater duct having of transverse inverted-T shaped ribs is performed. for the parameters p / e=7.14-17.86, Re=3800-18000. The study dealt with the use of a two-dimensional RNG-k-ε model to simulate a program with average solar radiation intensity in the form of heat flux of 1000 W/m². A Thermal enhancement factor of 1.87 is obtained as a result of enhancement in heat transfer for the SAH. As shown in figure (2-16)
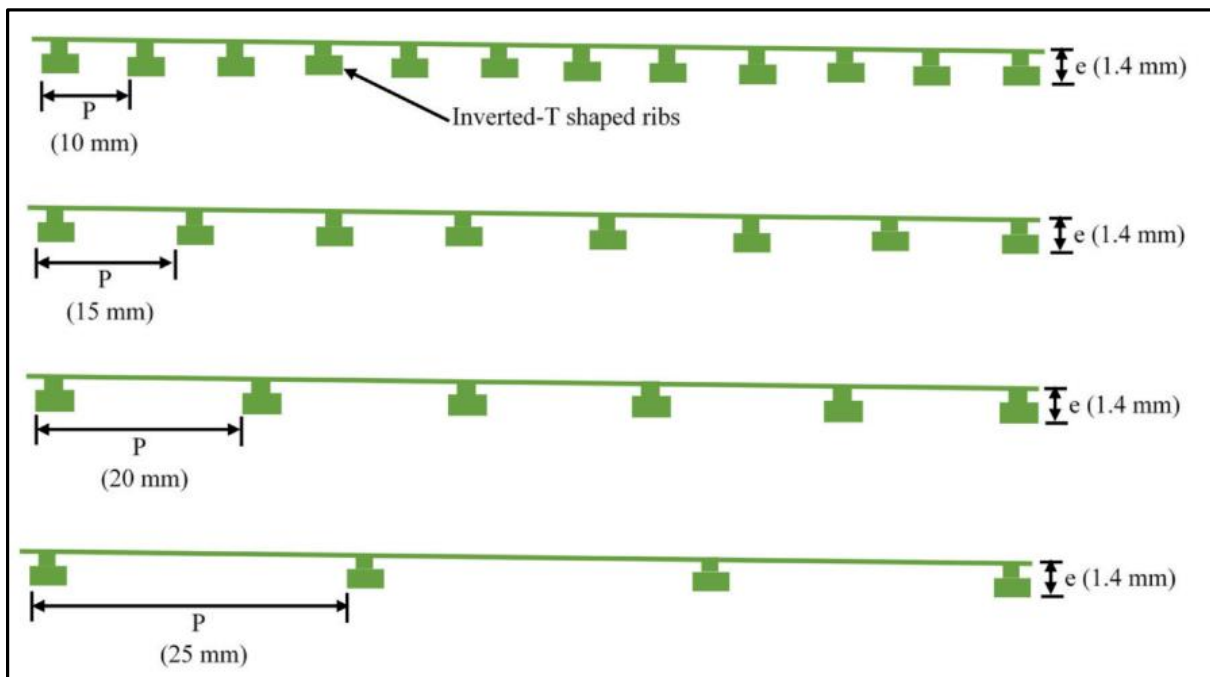
Figure (2-16): Transverse inverted-T shaped ribs. [34]

Olfiten et al.[35] numerical investigation presented to study the effect of using two different types of baffles on the thermal performance of a SAH at the rate of Re=(100-2000), at an angle of attack of 30º fixed, in the form of a protracted at α =90º. Where Nu = 148.15 and pressure drop= 316.67 at Re= 2000 increase compared to the model without baffles as shown in figure (2-17).
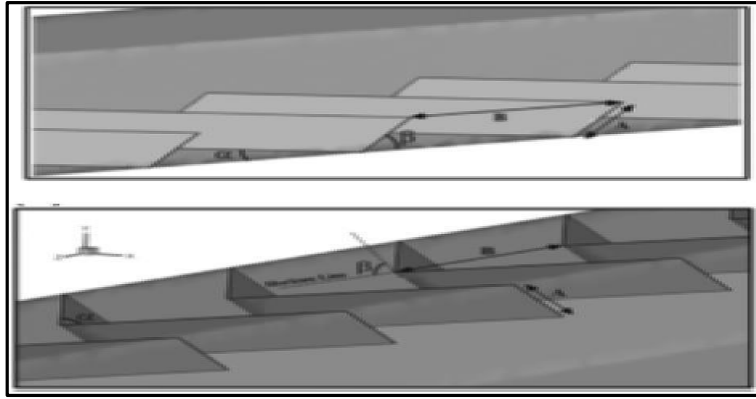
Figure (2-17): Geometry artificial roughness rectangular baffles[35]

Smith et al.[36] An experimental and numerical analysis to investigation thermal evaluation of flow channel with perforated-baffles. The perforated-baffles were designed in two forms: perforated-baffle (PB) and perforated-baffle with square wings (SW-PBs). Transverse solid baffles (TBs) were also tested for an assessment. All baffles had an identical height of 12 mm ($e/H = 0.3$). Experimental results showed that SW-PBs offered better Nu than PBs. It is also seen that PBs and SW-PBs caused lower pressure loss than TBs by around 20.49% and 13.98%, respectively. The reduction of friction loss was primarily due to the baffle perforation. In addition, the PBs yielded the thermal performance factors (TPF) up to 1.01 at the lowest Reynolds number of 6000. As shown in figure (2-18).
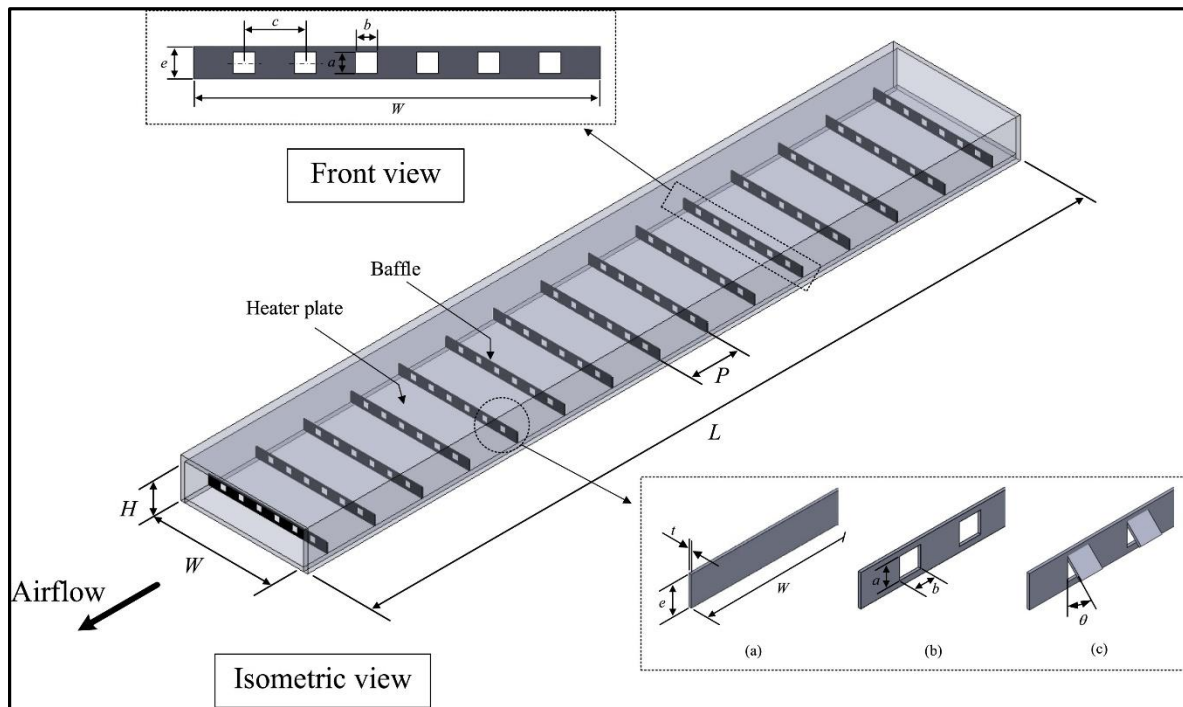
Figure (2-18): The perforated-baffles

Promvonge et al.[37] An experimental investigation the effect of arc-shaped twisted-baffles on augmented heat transfer in a rectangular duct solar air heater. Five attached angles (α) between 20º and 90º were used to form the arc-shaped twisted-baffle (T-ABs).as shown in figure (2-19). Some factors, such as pitch ratio (p/w) and Re (4000-20,000) are expressed as dimensionless parameters. For each experiment at a different pitch lengths (p), with p = 12 mm (p/w = 4.0), p = 18 mm   (p/w = 6.0), p = 24 mm   (p/w = 8.0),   and p = 30 mm (p/w = 10.0), respectively.The optimum condition is achieved using T-ABs at an attached arc-shape angle of α = 90º, p/w = 4.0 and Re = 4000, where the heat transfer rate (Nu), friction factor (f) and TPF are found to be, respectively, 3.31, 4.68 and 1.98 times greater than those of a plain channel.
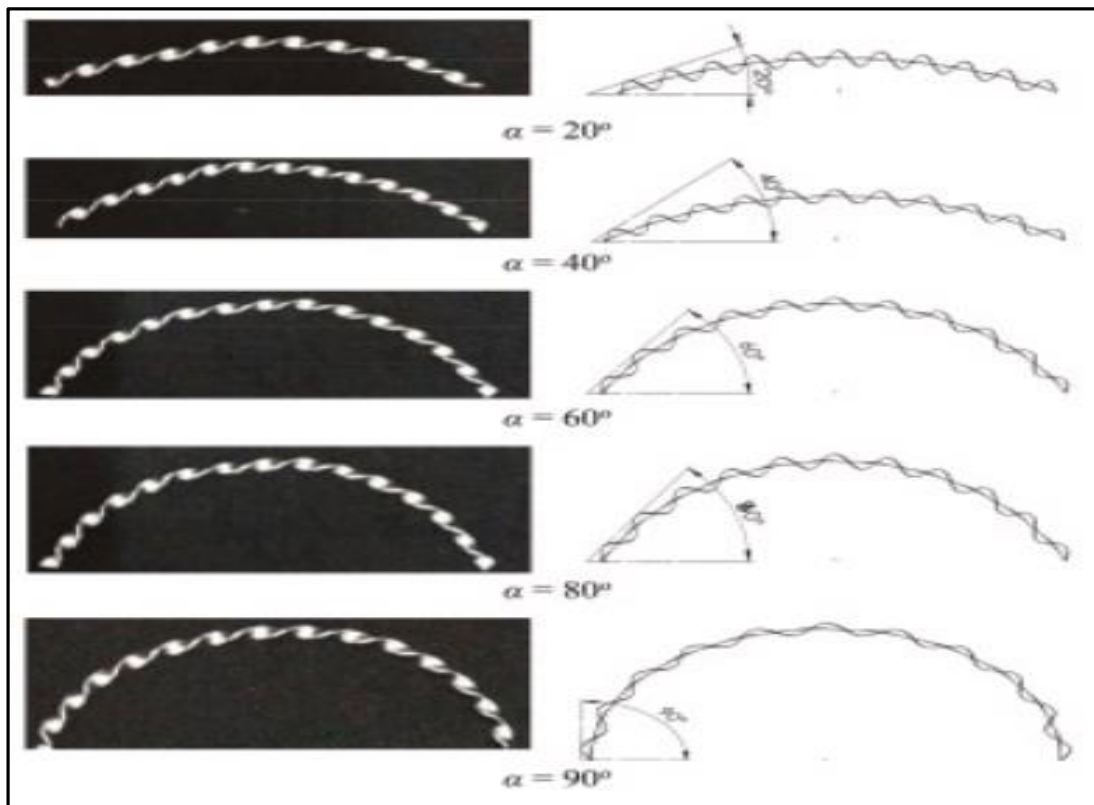
Figure (2-19): Arc-shaped twisted-baffles. [37]

2.3 Summary

Table 2.1 shows the summary for this chapter:

Table 2-1. Literature review summary.

Author	Year	Geometry	Research type	Results summary
1. Studies on the artificial roughness of rib				
Sahu et al.[14]	**2005**	broken ribs at $\alpha = 90°$	Experimental	• The maximum thermal efficiency was obtained by 83.5%.
Saini et al.[15]	**2008**	dimples	Experimental	• The maximum value of Nusselt number=73 has been found corresponds to relative roughness height (e/D) of 0.0379 and relative pitch (p/e) of 10. • The minimum value of friction factor=0.06 has been found correspond to relative roughness height (e/D) of 0.0289 and relative pitch (p/e) of 10.
Alam et al.[16]	**2017**	conical protrusion	Numerical	• Thermal efficiency are found as 69.8% and enhancement factor 1.346%

Ghritlahre et al.[17]	**2020**	arc shape of the shadow	Experimental	• The best thermal performance for upstream apex = 72.2% and for down apex = 63.1% compared to smooth.
2. Studies using Fins and Baffles / Vortex Generators				
Zhou et al. **[18]**	**2012**	curved trapezoidal winglet type vortex generators	Experimental	• The thermal-hydraulic performance was highest 1.3 at Reynolds No. 18000
Yadav et al. **[19]**	**2014**	square sectioned transverse rib	Numerical	• The best optimization of the Nusselt number was obtained at parameters p/e = 7-17, e/D_h=0.042, Nu/Nus = 2.860.
kumar et al.**[20]**	**2014**	Sinusoidal Corrugated	Experimental	• The thermal performance factor is 2.05
Chabane et al.[21]	**2014**	longitudinal fin	Experimental	• The values of thermal efficiency at the mass flow rate of 0.012 and 0.016 kg/ s with and without using fins varied from 40.02% to 51.50% and from 34.92% to 43.94%, respectively.

Skullong et al.[22]	**2016**	square and thin ribs 90º	Experimental	• obtained that the inline rib array provides the maximal heat transfer while staggered thin ribs show the highest thermal improvement factor whereby obtained Nu/Nu_o=2.13 -2.16.
Skullong et al.[23]	**2017**	combined wavy-groove and delta-wing vortex generator (WVG)	Experimental	• Thermal improvement factor of 2.24 is obtained when such a coarseness is used with a ratio Nu/Nuo=5.74, f/fo=17.01.
Singh et al. [24]	**2017**	V-shaped ribs and cylindrical dimples	Experimental	• Thermal performance factor equal to 1.65.
Grill et al.**[25]**	**2017**	broken arc rib	Numerical	• The highest thermos-hydraulic performance parameter achieved was 1.94 at 0.65 relative gap position
Singh et al.[26]	**2018**	square wave profiled transverse ribs	Numerical	• The Nusselt number and the friction factor (f) are improved when using this form of synthetic roughness $Nu = 2.14, f = 3.55$.
Kumar et al.[27]	**2019**	twisted roughness	Experimental	• At p / e = 8, α = 60º, and y / e = 3 they get ratio of Nu and the friction factor (2.46, 1.78) respectively.

Promvonge et al.[28]	**2019**	combined turbulence promoters	Experimental	• The highest TPF of about 2.47
Tongyote et al.[29]	**2019**	combined V-rib and chamfered-V-groove vortex generator	Experimental	• The highest TPF= 1.907 that obtained at parameter p/H=1.5, e/H=0.4
khanlari et al.[30]	**2020**	plus-shaped perforated baffles	Experimental and numerical	• Thermal efficiencies of PPSC, PPSCB and PPSCDB are in the range of 62.10-66.32%, 65.72-69.62% and 71.12-75.11%, respectively.
Bayralcu et al.[31]	**2020**	different baffle positions	Experimental and numerical	• the highest Nusselt number value obtained was 70 in case 4. the lowest friction factor values were found to be 0.05 for cases 1, 2 and 3, with nearly identical values (Re = 8340).
Wang et al.[32]	**2020**	S-shaped with a gap	Experimental	• The optimization of thermal efficiency increased by (13% - 48%) compared to the smooth channel.
Baissi et al.[33]	**2020**	Longitudinal delta baffles shaped	Numerical	• Improvement was obtained in Nu and an increase in heat transfer and hypotension as Nu = 6.94, f = 45.83

				compared to the smooth channel and the highest thermal improvement factor 2.26.
Mahanand et al.[34]	**2020**	transverse inverted-T shaped ribs	Numerical	• Thermal enhancement factor of 1.87
Olfiten et al.[35]	**2020**	two different types of baffles	Numerical	• Where Nu = 148.15 and pressure drop= 316.67 at Re= 2000 increase compared to the model without baffles.
Smith et al.[36]	**2023**	perforated-baffles	Experimental and numerical	• Thermal performance factors (TPF) up to 1.01
Promvonge et al.[37]	**2023**	arc-shaped twisted-baffles	Experimental	• Where the heat transfer rate (Nu), friction factor (f) and TPF are found to be, respectively, 3.31, 4.68 and 1.98 times greater than those of a plain channel.

Chapter Three

Numerical simulations

Chapter Three

Introduction

In this chapter presents the use of the ANSYS FLUENT version 17. Which was used for CFD analysis to simulate a SAH with dimensions (length * width * height) (2100 * 300 * 30) mm with and without artificial roughness. In this numerical analysis, the following is done:

1. The first step is to create an architecture using the SolidWorks 2021 study program.

2. The second step after entering the variables and parameters of the model, the program solves the equations needed to simulate it in each element of the mesh until it reaches the best convergence.

3. The third step: When the best affinity is reached, the smooth results will be compared with the empirical equation, and after that, the artificial roughness will be added

3.1 Building model

A simplified physical model must be established in order to examine the heat transfer performance and flow properties of the air channel of SAH. Examines the duct depicted in Fig. (3-2) with one hot absorber plate and three smooth, insulated sides. The model was created using SolidWorks 2021. In addition, exported to ANSYS DESIGN MODELER. The dimensions of the duct are as follows: L=2.1 m, W = 0.3 m, and H = 0.03 m. The angular S-shape and arc-shape parameter is kept constant at $\alpha=60^{\circ}$. In Table 3-1, the parameters that were used in drawing the model are clarified.

Table (3-1) parameters of geometry used in SAH

S. No.	Parameter	Units in (m)
Duct parameter	Width, W	0.3
	Height, H	0.03
	Thickness of glass	0.04
	Thickness of glass-wool	0.5
	Glass covers the distance from the plate absorber	0.03
	Length, L	2.1

3.2 Mathematical Modeling

The current study included three-dimensional simulation of SAH. The following assumptions introduced as:

1.   The flow is steady state, incompressible flow and three-dimensional.

2.   There is no slip.

3.   Thermal conductivity does not change along the duct.

4.   Homogeneous and isotropic roughness material and wall duct.

5.   No heat loss from the bottom due to good insulation with a thickness of 40 mm.

6.   The heat loss from the glass due to radiation from the absorber plate neglected.

3.3 Meshing

Mesh is the most important determinant in the numerical simulation process used as it plays a role in determining the accuracy of the solution Created in ANSYS ICEM CFD V.17 the mesh is well fabricated near the walls and roughness in the middle to show the effect of the boundary layer. A fine mesh is adopted for analysis after careful examination. There are two regions, the first region is where the fluid flows over the absorbing plate of solar radiation, whose dimensions are (2.1 * 0.3 * 0.03) m. The second region is the artificial roughness region with a thickness of 0.5 mm with parameters l / H= (0.8335, 1.666, 2.5, and 3.335), p/H= (1.667, 3.33, 5, and 6,667), the value of the attack angle is fixed at α=60º, in addition to d/H=1.33, b/H=0.667, e/H=0.4. The intensity of solar radiation in the form of heat flux was taken as (965,967,966 and 966) W/m^2 for simulation. The number of iteration used to obtain the results is 500.

(a)

(b)
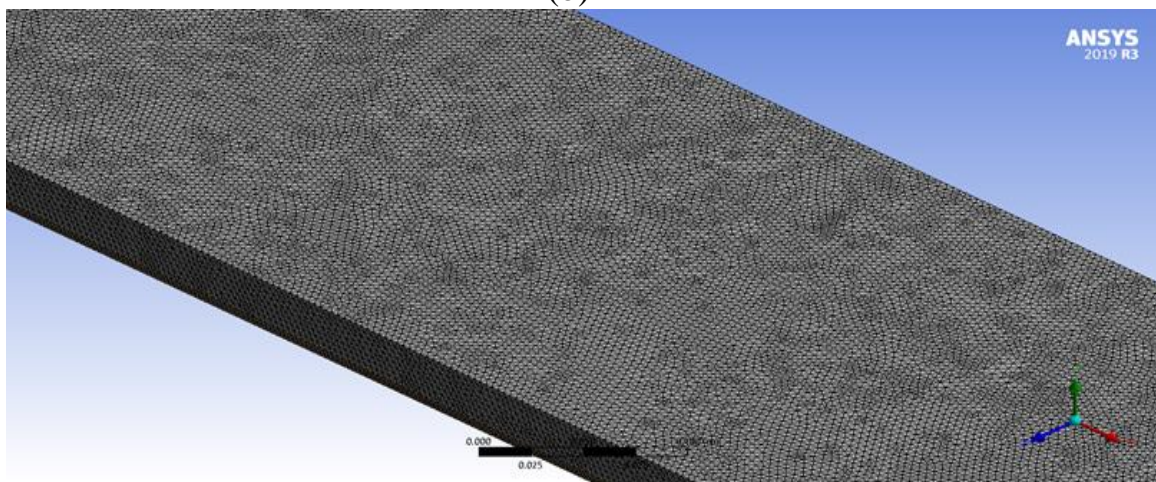
(c)

Figure (3-1): (a) & (b) The computational meshing of the various shape of geometry at α=60º (c) Elements size of rough surface with S and arc shaped

3.4 Grid-Independent study

In a numerical inquiry, obtaining an accurate result of Nu and for the suggested geometry is vital, and ANSYS ICEM CFD V.17 is used for meshing - grid element distribution. Validating mesh grid-independent test to forecast Nu and values yields an appropriate computation analysis outcome. Variable element sizes [four distinct values ranging from 1 mm to 4 mm] were utilized to determine the optimal element cell size for the current operation. Table (3-2) outlines the validation outcomes. A typical view of the mesh can be seen in figure (3-2). According to the proposed element size, a no uniform triangular grid is generated using a fine mesh solution and convergent engagement between 8156465 and

14282863 element cells for arc shaped and for S-shaped between 4864379 and 17355745. The largest Nu divergence was found in the 9859884-element cell, whereas the average Nusselt number variation showed the least deviation at +6.7% for arc shape and S-shape at +7.1% and the average frication factor variation showed the least deviation at +7.4% for arc shape and S-shape at +7.9% . Consequently, the 17355745-element cell for S-shape and 14282863 is utilized for analytical research.

(a)   (b)

(c)   (d)

(e)   (f)

(g)   (h)
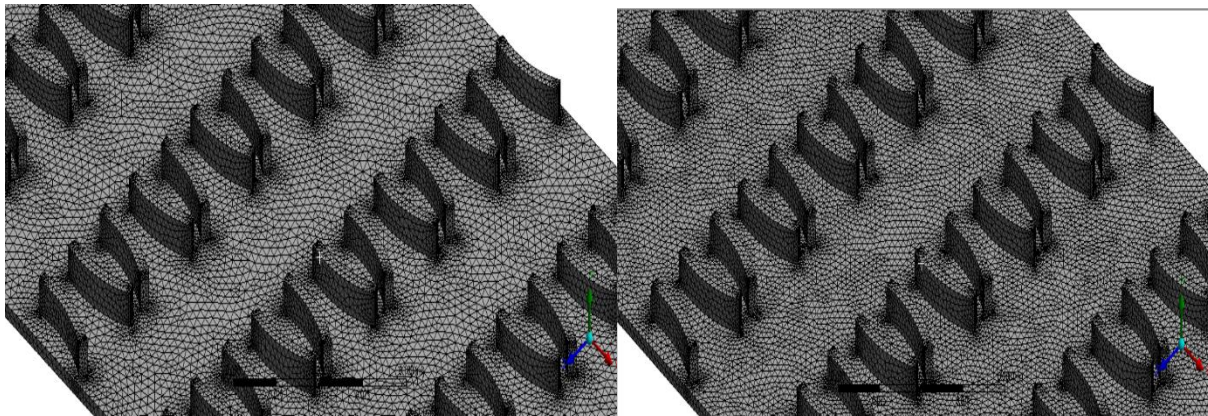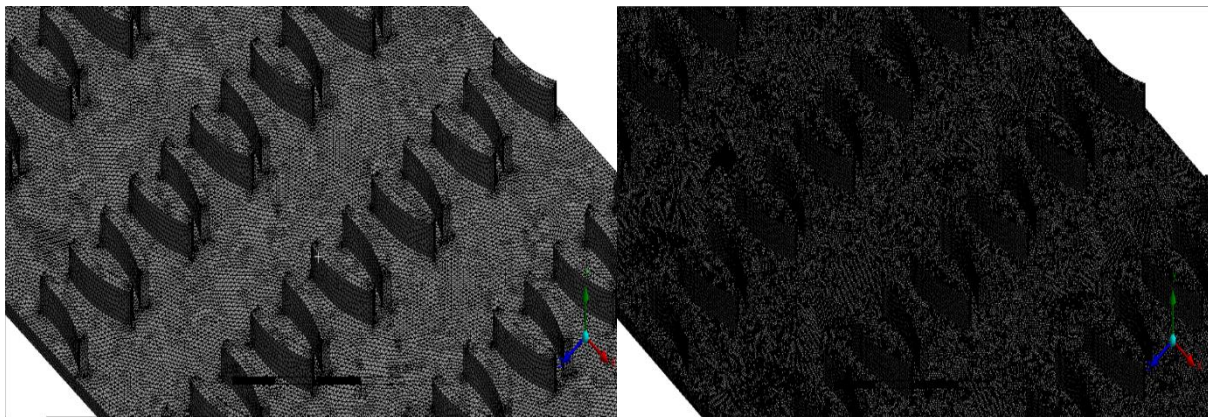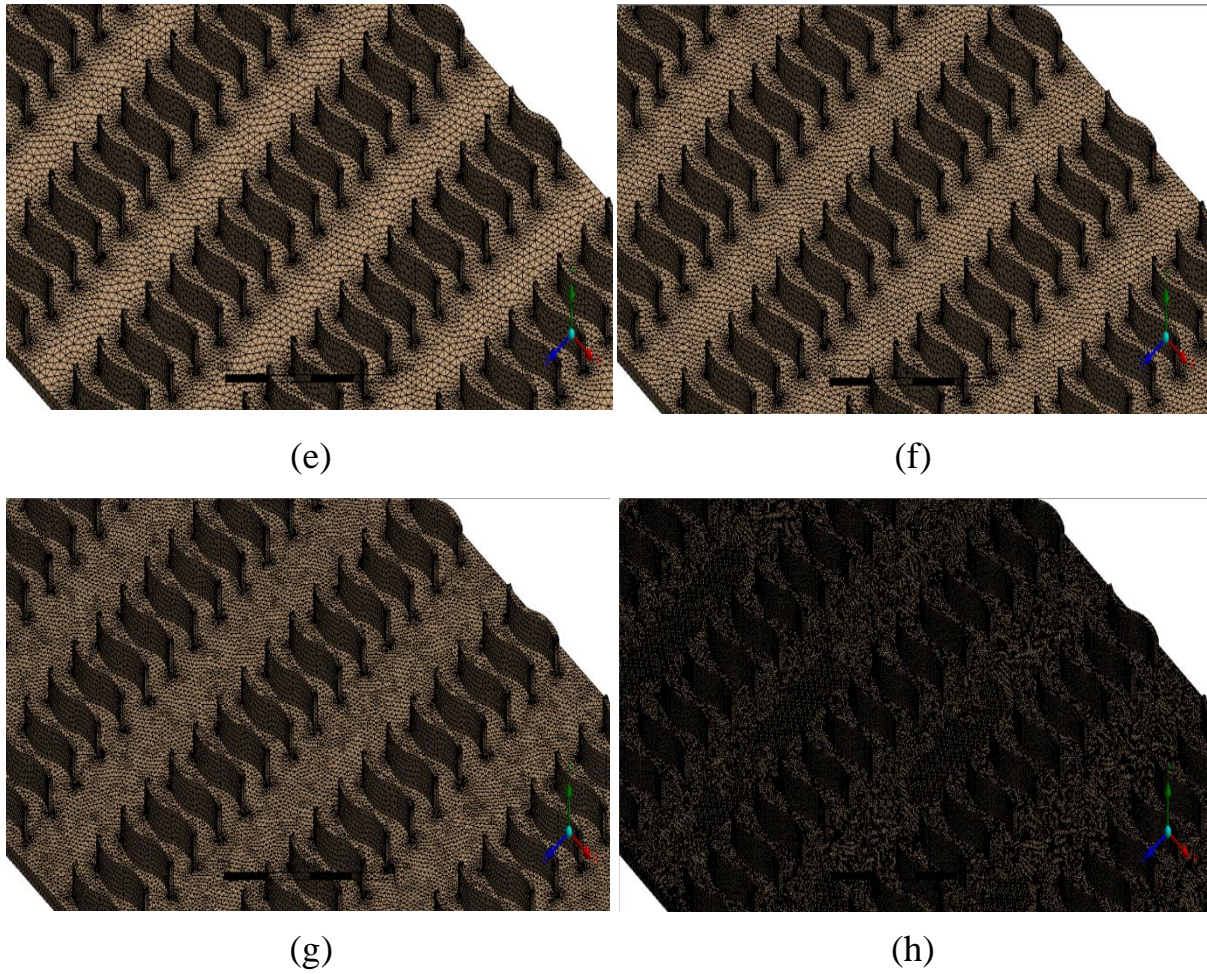
Figure (3-2): The computational grid (a) 8156465 cells (b) 9326598 cells (c) 11598745 cells (d) 14282863 cells (e) 4864379 cells (f) 6659874 cells (g) 12598745 cells (h) 17355745 cells.

Table (3-2): Grid Independent Validation

Geometric	Number of elements
Smooth surface	1485950-2580000
S-shape	4864379-17355745
Arc-shape	8156465-14282863

3.4 The physical material used in simulation

1. The rectangular channel used is made of galvanized iron according to the characteristics mentioned in table (3-4) as in figure (3-3).
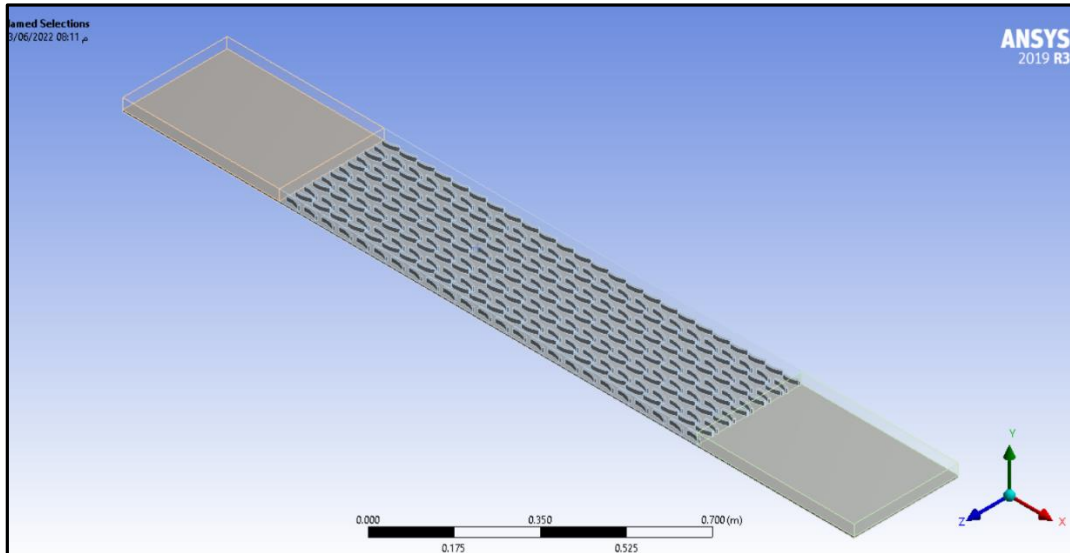
Figure (3-3): SP-SAH duct

2. The radiation absorbing plate is made of aluminum as shown in figures (3-4).
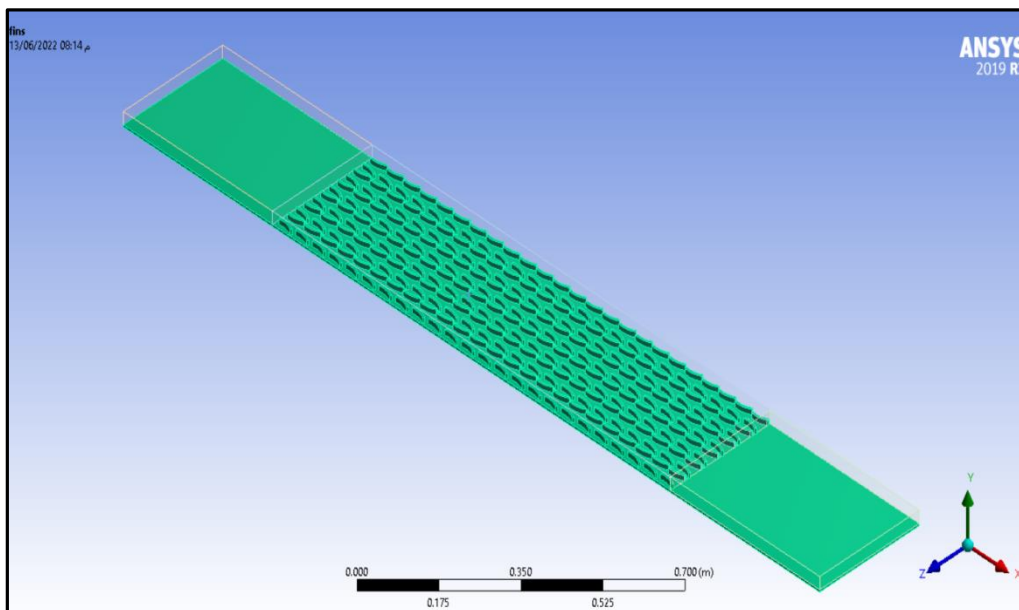
Figure (3-4): Absorber plate

41

3.   Glass

The glass cover absorbs small amount of solar energy which transferred to heat. In addition, there is a radiant thermal energy from absorber plate received by the glass cover due to the temperature difference between them. The heat gained by glass cover is transferred to the ambient air by convection. Another function of the glass is to prevent dust from entering the absorption plate from the outer circumference.

Table (3-3): the properties of glass

Properties	Specification
Density	2500 kg/m3
Thermal conductivity	0.96 W/m/°C
Specific heat	840 J/g K
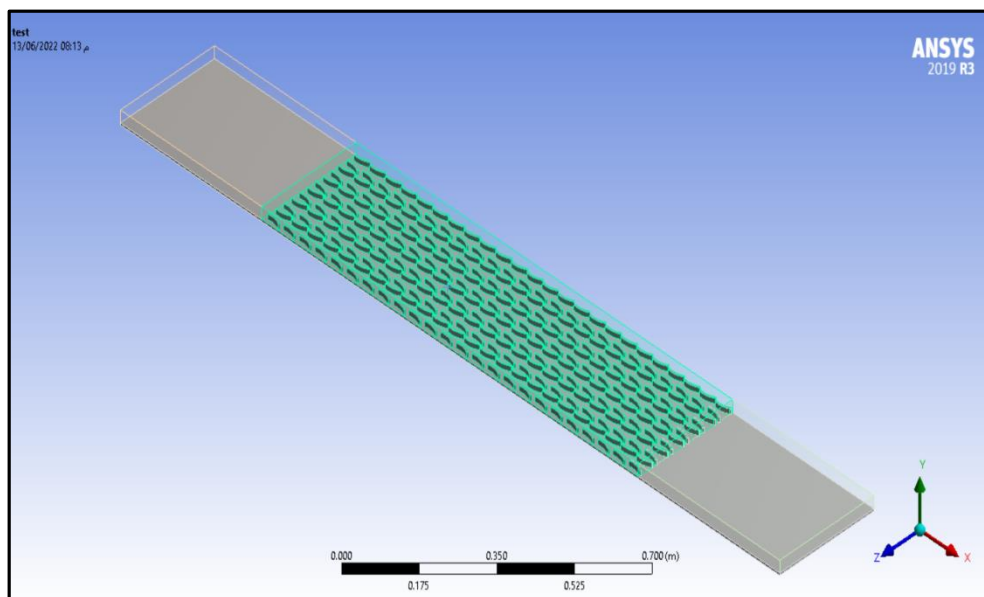
Figure (3-5): View of glass

Table (3-4) the physical properties of thermal-hydraulic of present work [38]

Properties	Air	Aluminum	GI
Density (ρ)	$1.225\ kg/m^3$	$2719\ kg/m^3$	$7870\ kg/m^3$
Specific heat (C_p)	$1006.4\ J/kg.k$	$871\ J/kg.k$	$896\ J/kg.k$
Viscosity (μ)	$1.789*10^{-5}\ kg/m.s$	-------	----------
Thermal conductivity (K)	$0.0242\ W/m.k$	$202.4\ W/m.k$	$204.2\ W/m.k$

3.5 Turbulent model

When attempting to forecast improvements in thermal performance using computational fluid dynamics, validation of turbulent models is crucial. Several turbulent models, including the a) conventional k- ε model, b) Renormalization k- ε model, and c) Realizable k- ε, model, were employed to verify the average Nu of the smooth surface in the current study. In Fig. (6-3), we see a visual representation of the obtained results .Disruption in the SAHs smooth flow was discovered to be influenced by the RNG - renormalization k-ε model. When compared to the predicted value obtained using Equation (5.1), other models either fall short or exceed the expected value. It, was, concluded, that the Nu values in the Renormalization, k- ε model were more in line with the empirical correlation values. The current study simulated SAH to detect increased heat transport by using the renormalization, group, k- ε model. With the CFD method, several researchers have used the same model[19], [39], [40].
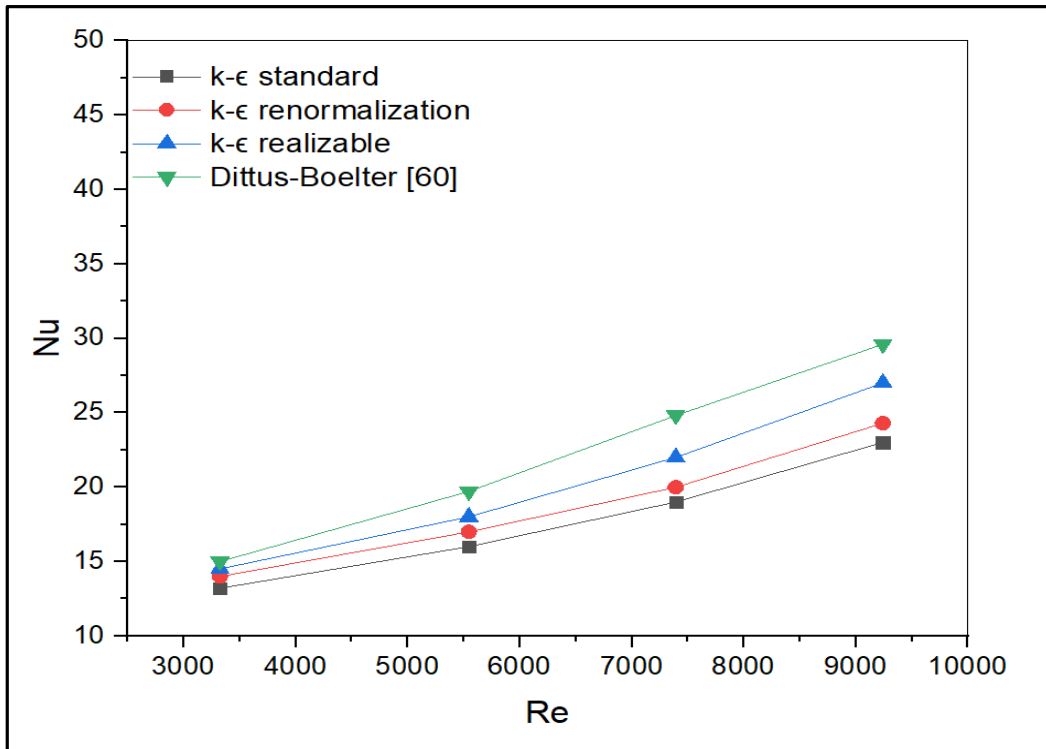
Figure (3-6): validation of turbulent models.

3.6 Equations used in the Analysis

According to the assumptions, the form of the equations for the continuity and momentum equations in three dimensional and the energy equation is as follows[41]:

1.   Continuity Equation (Conservation of Mass):

$$\frac{\partial u}{\partial x} + \frac{\partial v}{\partial y} + \frac{\partial w}{\partial z} = 0 \qquad\qquad (3.1)$$

2.   Momentum equations

➢ At x-direction

$$\rho\left(u\frac{\partial u}{\partial x}+v\frac{\partial u}{\partial y}+w\frac{\partial u}{\partial z}\right)$$

$$=-\frac{\partial p}{\partial x}+\frac{\partial}{\partial x}\left(\mu\frac{\partial u}{\partial x}\right)+\frac{\partial}{\partial y}\left(\mu\frac{\partial u}{\partial y}\right)+\frac{\partial}{\partial z}\left(\mu\frac{\partial u}{\partial z}\right) \qquad (3.2)$$

➢ At y direction

$$\rho\left(u\frac{\partial v}{\partial x}+v\frac{\partial v}{\partial y}+w\frac{\partial v}{\partial z}\right)$$

$$=-\frac{\partial p}{\partial y}+\frac{\partial}{\partial x}\left(\mu\frac{\partial v}{\partial x}\right)+\frac{\partial}{\partial y}\left(\mu\frac{\partial v}{\partial y}\right)+\frac{\partial}{\partial z}\left(\mu\frac{\partial v}{\partial z}\right) \qquad (3.3)$$

➢ At z direction

$$\rho\left(u\frac{\partial w}{\partial x}+v\frac{\partial w}{\partial y}+w\frac{\partial w}{\partial z}\right)$$

$$=-\frac{\partial p}{\partial z}+\frac{\partial}{\partial x}\left(\mu\frac{\partial w}{\partial x}\right)+\frac{\partial}{\partial y}\left(\mu\frac{\partial w}{\partial y}\right)+\frac{\partial}{\partial z}\left(\mu\frac{\partial w}{\partial z}\right) \qquad (3.4)$$

3.   Equation of energy:

$$\frac{\partial T}{\partial t}+u\frac{\partial T}{\partial x}=\alpha\frac{\partial^2 T}{\partial x^2} \qquad (3.5)$$

4.   Transport equation for the RNG k-ε model [42]

$$\frac{\partial(\rho k)}{\partial t}+\frac{\partial(\rho u k)}{\partial x}=-\frac{\partial}{\partial t}\left[(a_k\mu_{eff})\frac{\partial k}{\partial x}\right]+G_k+G_b-\rho\varepsilon-Y_M+S_k \qquad (3.6)$$

$$\frac{\partial(\rho k)}{\partial t}+\frac{\partial(\rho u \varepsilon)}{\partial x}=-\frac{\partial}{\partial t}\left[(a_k\mu_{eff})\frac{\partial \varepsilon}{\partial x}\right]+G_{1\varepsilon}\frac{\varepsilon}{k}(G_k+G_{3\varepsilon}G_b)+G_{2\varepsilon}\rho\frac{\varepsilon^2}{k}-R_\varepsilon+$$

$$S_k \qquad\qquad\qquad\qquad\qquad\qquad\qquad\qquad\qquad\qquad\qquad\qquad\qquad (3.7)$$

In the equation, the term of turbulence kinetic energy generation is due to mean velocity gradient it defines as

$$G_k = -\rho \overline{\acute{u}_i \acute{u}_j} \frac{\partial u_j}{\partial x_i} \qquad (3.8)$$

Where μ_{eff} represent the effective turbulent viscosity and is given by

$$\mu_{eff} = \mu + \mu_t \qquad (3.9)$$

Where μ_t turbulent viscosity is combining $k \ and \ \varepsilon$ as following:

$$\mu_t = \rho C_\mu \frac{k^2}{\varepsilon} \qquad (3.10)$$

In equation the term of turbulence kinetic energy generation due to mean velocity gradient and buoyancy G_k and G_b respectively. $G_{1\varepsilon} = 0.09$, $G_{3\varepsilon} = 1.92$ And $G_{2\varepsilon} = 1.44$ that constant respectively[43].

3.7 Boundary condition

In general, the computational domain comprises a solar air heater duct with an absorber plate sitting on the x-y-z plane, surrounded by the intake, outlet, and both upper and lower wall boundaries. As the equation momentums are solved in the arithmetic domain, the terms of the non-slip boundary on the airway walls are assumed throughout the whole state. The surface of the lower wall is insulated, that is, adiabatic, while the surface of the top wall of the solar air heater is exposed to average solar radiation during the day in the form of constant heat flux (965,967,966, and 966) W/m². The constant inlet temperature is assumed 300 K. In the case of the input limitations of the arithmetic range, a variable airflow rate with velocity values of (0.9, 1.5, 2, and 2.5) m/ s is provided. At flow inlets, mass flow rate inlet boundary conditions are often employed to determine flow velocity and all related numerical flow parameters. In this simulation, four uniform mass

flow rates are established at the field's entrance. The velocity of the flow intake is computed using the Reynolds number. On leaving the arithmetic domain, the port boundary condition is given. At the output of the outlet, continuous pressure of 1.013 x 10^5 Pa is applied to the outlet boundary condition. The thermo-physical parameters of air, aluminum absorption plate, and galvanized iron are displayed in Table (3-4).

(I)   The air velocity at the inlet is variable by fours values.

   At inlet section in the X-direction
$$u = u_o, v = 0, T = T_o, w = 0$$

(II)   At the exit, atmospheric pressure is applied.

   At the exit section
$$\frac{\partial u}{\partial x} = 0, \frac{\partial v}{\partial x} = 0, \frac{\partial T}{\partial x} = 0$$

(III)   The solar collector is isolated.

   Side and bottom walls
$$\dot{q} = 0$$

(IV)   The heat flux on the duct surface in the amount of (965,967,966, and 966) W/m^2 is the average value of days during which the test was carried out.

   At the top of the wall (absorber plate)
$$u = 0, v = 0, q = 965,967,966, \text{and } 966 \text{ W/m}^2$$

3.8 Uncertainty analysis

Verification of Uncertainty the following relationship can be used to indicate a possible error value in the measurement tools: A related formula between the dependent and independent variables can be used to figure out the resultant uncertainty value [55].

$$Y_R = \sqrt{\Sigma_0^i \left(\frac{\partial R}{\partial z_i} \cdot Y_{Zi}\right)^2} \tag{3.11}$$

$$R = f(Z_1, Z_2, \dots, Z_n) \tag{3.12}$$

Where:

Y_R: Uncertainty regarding the results

$Z_1, Z_2, \dots, Z_n$: Independent factors

$Y_1, Y_2, \dots, Y_n$: Associated variables.

the general formula to be employed to assess the uncertainty of the experimentally obtained performance analysis in the current study. Table 3-5. contains the methods used to calculate experimental uncertainty in the measurement of Nu, Re, f, h, and $\dot{m}$

Table 3-5: Range of determined uncertainty error %

Parameter discerption	Symbol	Units	Uncertainty error %
Mass flow rate	$\dot{m}$	Kg/sec	(±0.0004155) 1.478%
Heat transfer coefficient	h	W/m^{2}K	(±0.50249) 5.02%
Reynolds number	Re	dimensionless	(±0.50249) 5.02%
Friction factor	f	dimensionless	(±0.0204) 2.04%
Nusselt number	N	dimensionless	(±0.0381) 3.81%

Chapter Four

Experimental and Measurements

Introduction

In this chapter, experiments revealed the presence of two types of duct, one with the artificial roughness of a SP-SAH and the other with a smooth duct. They were examined at velocities (0.9, 1.5, 2, and 2.5) m/s according to Re (3325, 5545, 7393, and 9241) respectively.

In 2022, from 8:00 a.m. to 3:00 p.m., two SP-SAH models were produced and tested outdoors in Diwaniyah, Iraq (32N latitude and 45E longitude) in actual sunlight. This section discusses the primary components of the SAH and the measurement instruments.

4.1 Experimental device

Figure (4-1) depicts an image and an illustration of the two devices, illustrating their components, as well as the devices' size and uses. The SAH is a rectangular channel with dimensions of (2.1*0.3*0.03) m insulated with a layer of glass wool with a thickness of 4 cm and plywood plate with thickness 1 cm and topped by a layer of glass with a thickness of 4 mm, where the height of the air duct is 30 mm and the area of the solar collector is 0.63 m^2. The experimental setup includes three sections: an inlet section (0.6 * 0.3) m, test section (1.2 * 0.3) m, and an exit section (0.3 * 0.3) m. To get a fully developed turbulent flow used the below equations to ensure the inlet and exit section compatible with the design. The aspect ratio of 10 must be maintained. In addition to the lowest entry and exit parts, the thermal solar collector ASHARE standard (5√HW & 2.5√HW) measurements were also considered. A principal component of the system is the solar absorbent panel. A centrifugal pump operated by a control valve propels the air. Table (4-1) and Table (4-2) range of operating parameters used in SP-SAH and the value of geometry parameter used of SP-SAH, respectively.

Table 4-1 Range of operating parameter used in SP-SAH

Operating parameters	Range
Reynolds number "Re"	3323, 5545, 7393, and 9241
Prantel number "Pr"	0.7
Relative roughness length "d/H"	1.3
Relative roughness height "e/H"	0.271
The distance between each Arc and S shapes "b/H"	0.667
Relative roughness length "l/H"	0.8335, 1.667, 2.5, and 3.335
Relative roughness pitch "p/H"	1.667, 3.33, 5, and 6.667
Angle of attack	60º

Table 4-2 Value of geometry parameter used of SP-SAH

Operating parameters	Value (m)
Entrance length (L1)	0.6
Test section (L2)	1.2
Exit length (L3)	0.3
Width of duct	0.3
Height of duct	0.03
Hydraulic diameter D_h	0.054
Rib height (e)	0.0102
Pitch (p)	(5,10,15, and 20) cm
Aspect ratio W/H	10 (dimensionless)

There are several ways to measure the entry area to reach the fully developed case of turbulent flow[44]:

$$1. \quad 10 \leq \frac{L_e}{D} \leq 60 \quad ; \frac{L_e}{D} \approx 10 \qquad\qquad\qquad (4.1)$$

4.2 SAH purpose

Experimental set up has been designed and fabricated to study the effect of S and arc-shaped roughness elements on the heat transfer and fluid flow characteristics of a rectangular duct used in solar air heaters. show the contents of main components of SAH and pictorial view of experimental set up is shown in figure (4-1).

Figure (4-1): Photograph of SP-SAH

[1] blower	[6] thermocouples
[2] SAH duct	[7] stand
[3] artificial roughness	[8] data logger
[4] glass	[9] anemometer
[5] control valve	[10] solar power meter
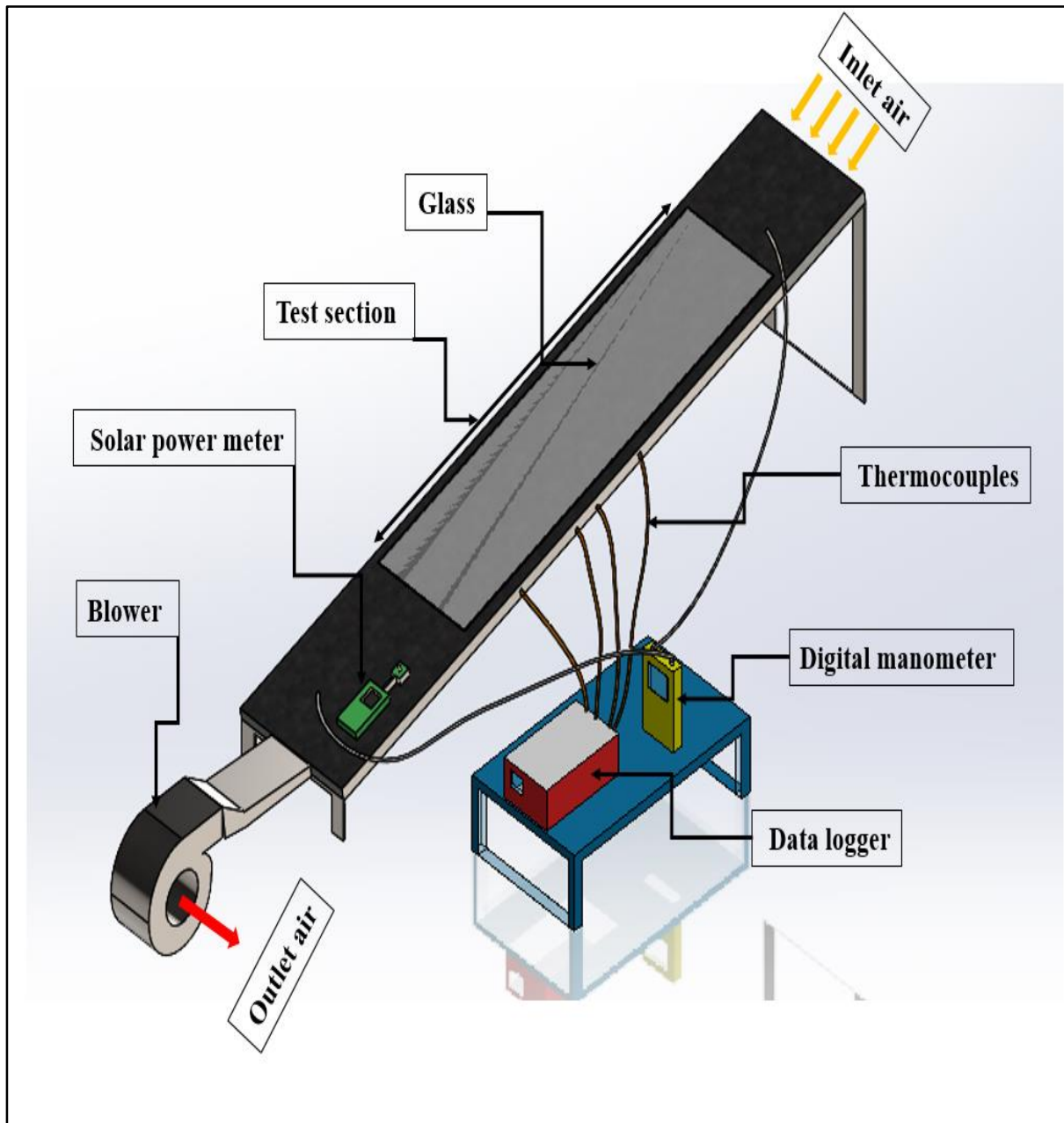
Figure (4-2): Schematic diagram of SP-SAH

4.2.1 Blower

Airflow blower fixed on port of exit air to pull air through collector as clear in figure (4-3). 2 Speed, Forward Curve, Direct Drive, Wheel Diameter 5 1/8 In. Table (4-3) showed the specification of blower.
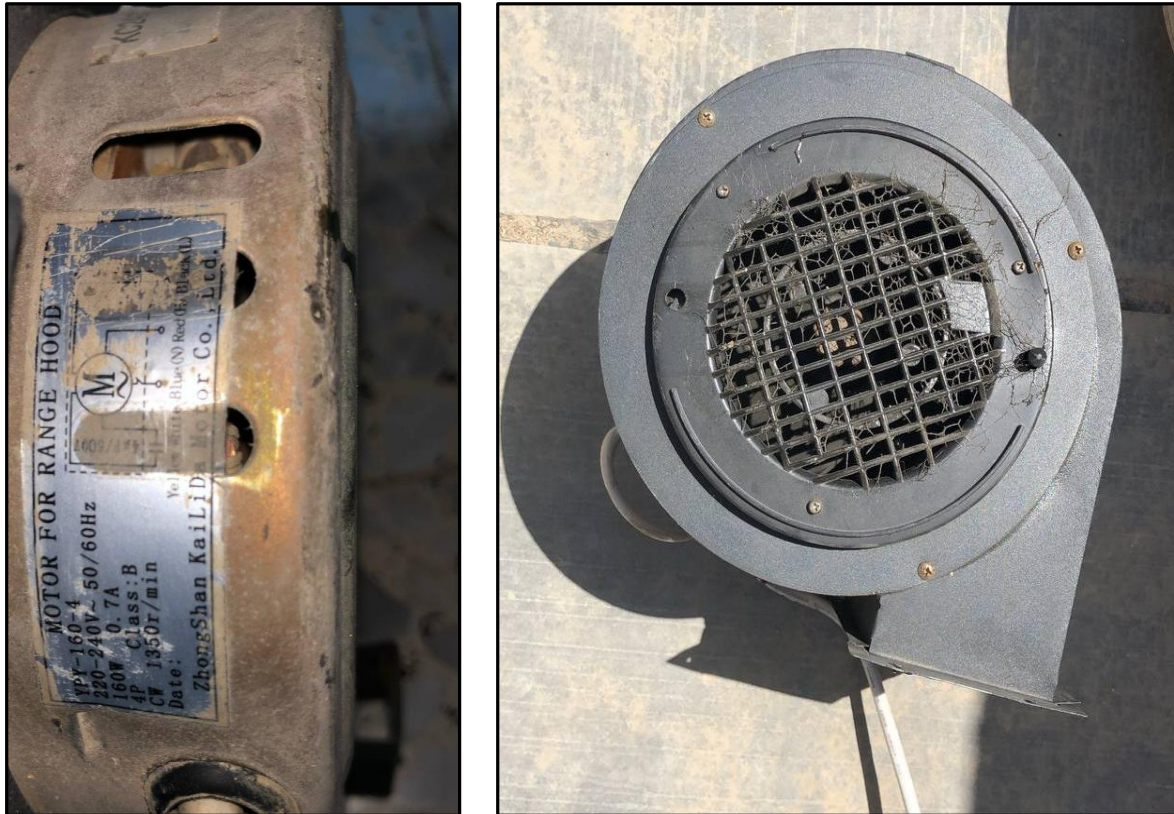
Figure (4-3) blower

Table (4-3): The specification of blower

Data			N	Product dimensions L x W x H
V	Hz	A		
220-240	50/60	0.7	1350 rpm	11.25 x11.25 x10.25 inches

4.2.2 SAH duct

The SAH is a rectangular channel with dimensions of (2.1*0.3*0.03) m insulated with a layer of glass wool with a thickness of 4 cm and plywood plate with thickness 1 cm and topped by a layer of glass with a thickness of 4 mm, where the height of the air duct is 30 mm and the area of the solar collector is 0.63 m². The experimental setup includes three sections: an inlet section (0.6 * 0.3) m, test section (1.2 * 0.3) m, and an exit section (0.3 * 0.3) m. as shown in figure (4-4).
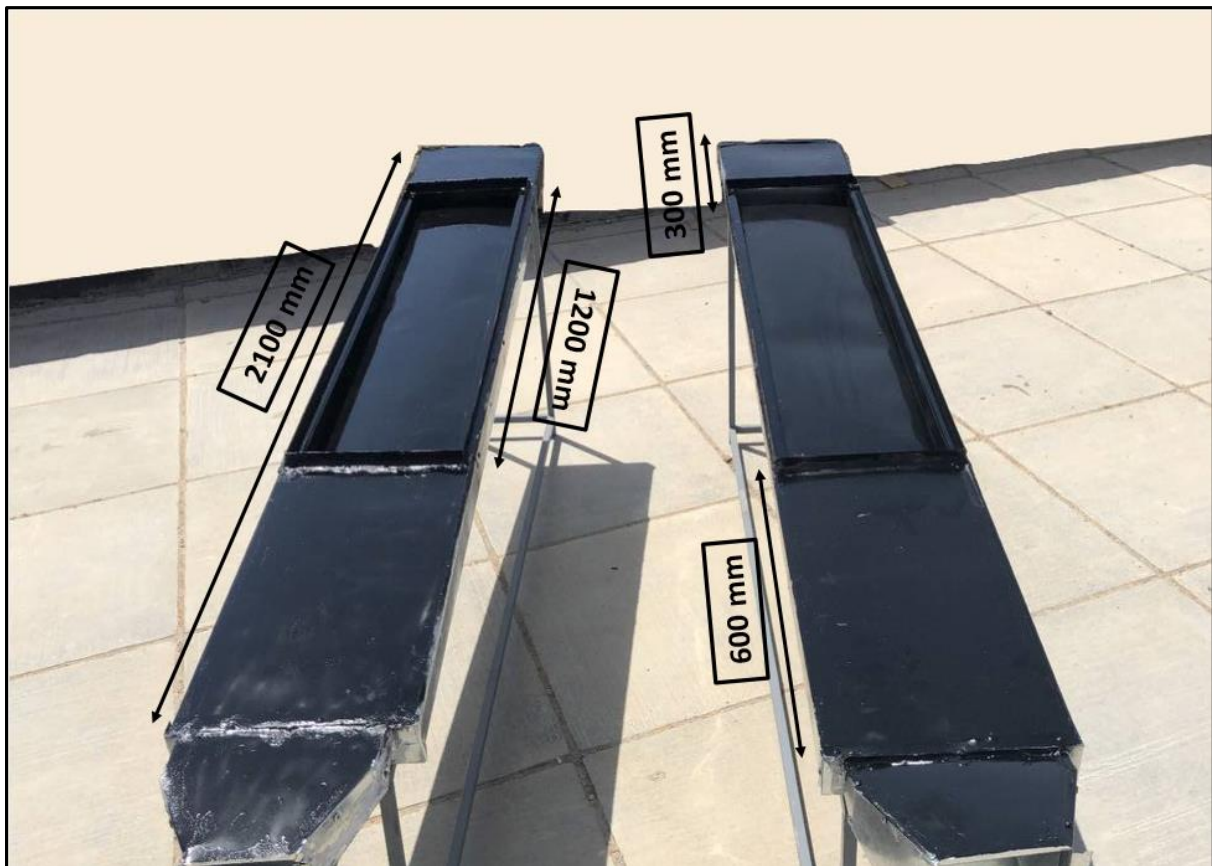
Figure (4-4): SAH duct.

4.2.3 Artificial roughness

It is one of the most essential aspects that helps to enhance the heat transfer coefficient and is regarded as one of the negative approaches with varying sizes and forms of artificial roughness depending on the assignment.

In the experimental examination, a solar radiation-absorbing panel was made GI roughness. The first kind employs an arc-shaped rectangular GI strip with a 60º angle of attack, while the second type is S-shaped in the form of vortex generators and consists of a GI strip with dimensions of (0.2 x 4) cm shown in figure (4-5) and (4-6). Arrange with parameters p/H = (1,667, 3,33, 5, 6.67) for inline arrangement and parameter l/H = (0.8335, 1.667, 2.5, 3.33) for staggered arrangement .We determine d/H to be 1.30, e/H to be 0.271, and the angle of attack (α) to be 60 °.
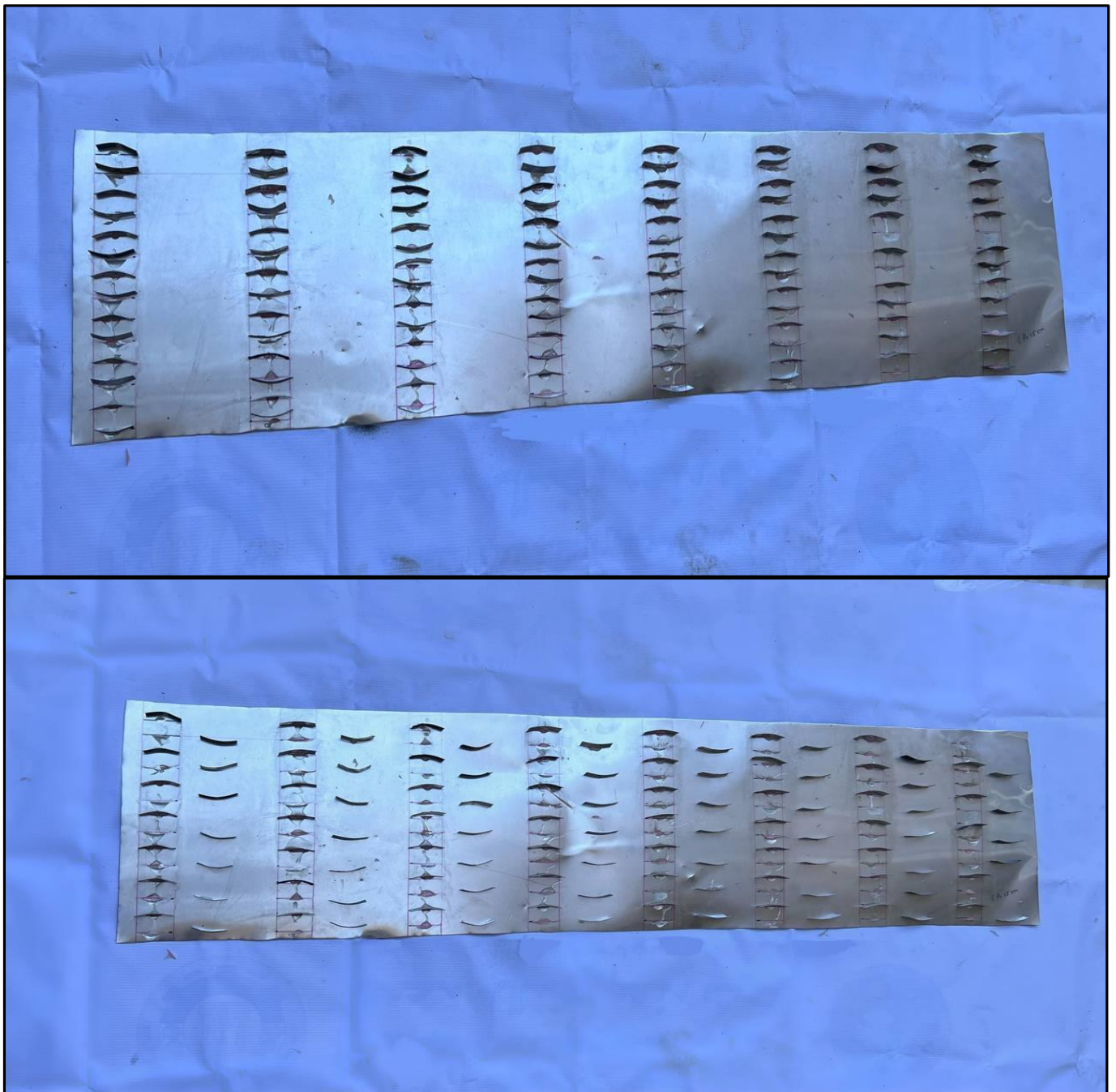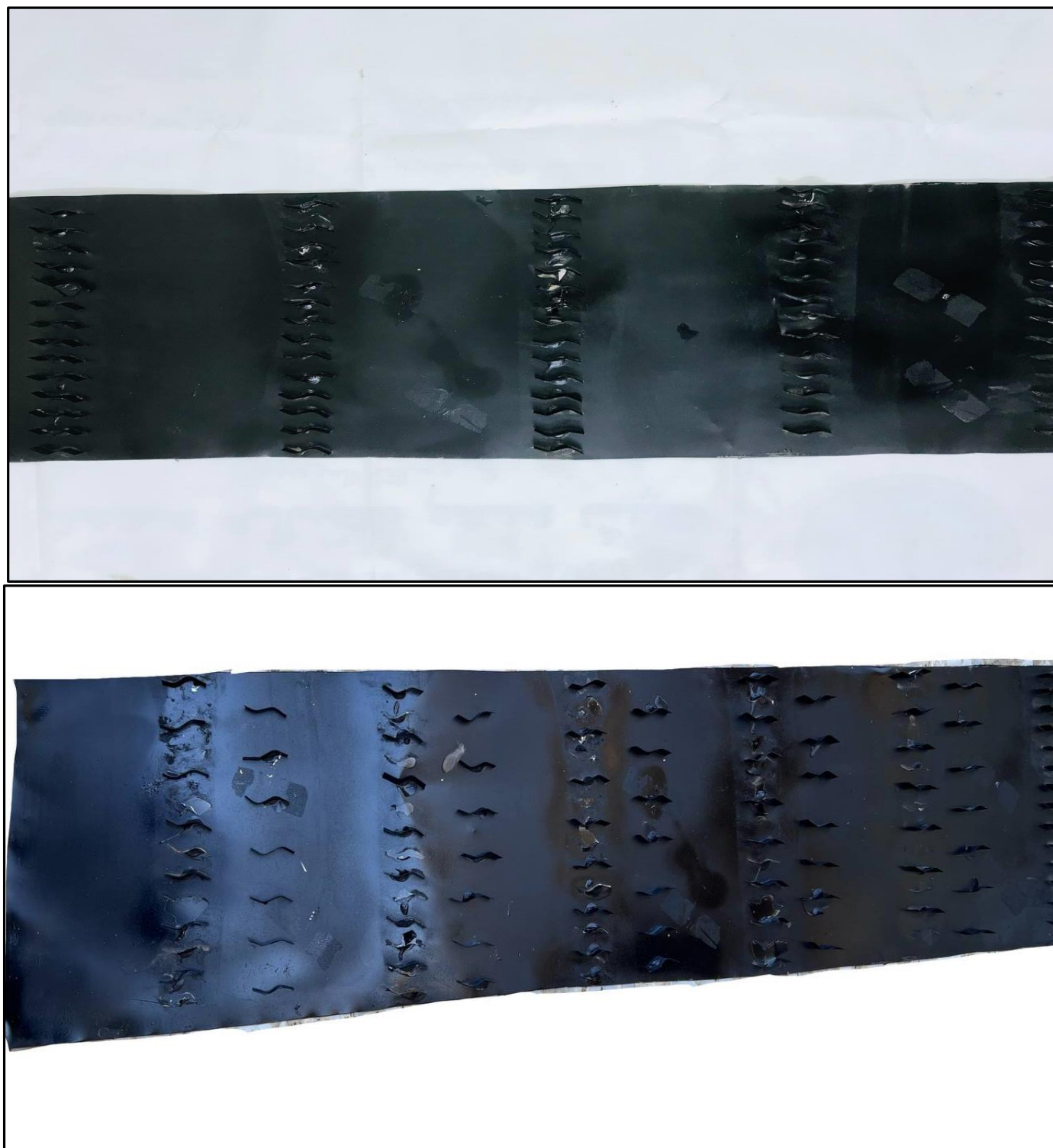
Figure (4-5): Absorber plate with artificial roughness arc and S-shape
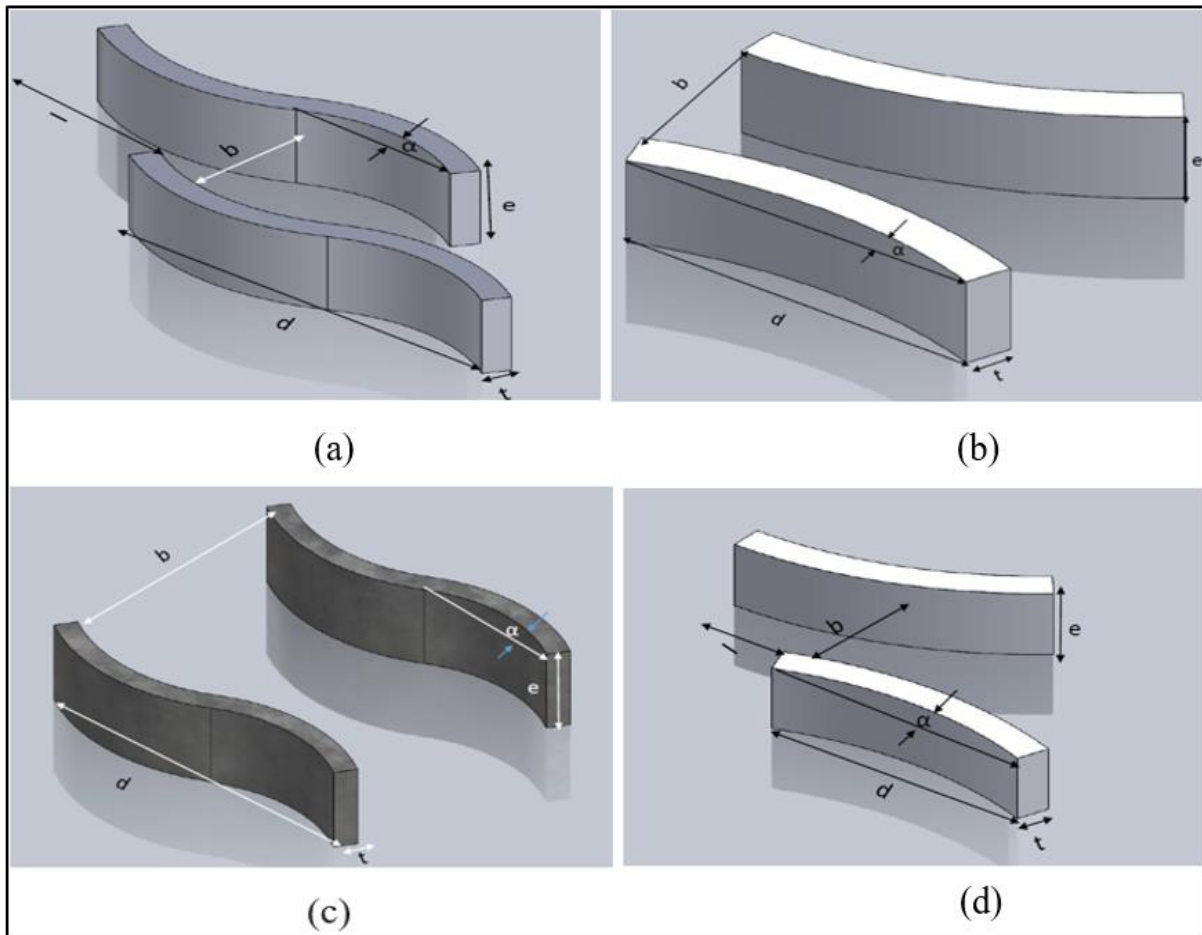
Figure (4-6): The schematic view of : (a) SRVG staggered, (b) ARVG inline, (c) SRVG inline, (d) ARVG staggered.

4.2.4 Glass

Glass is commonly used for solar heater glazing because it can transmit up to 90 % of short-wave solar energy while transmitting all wavelengths. The glass used in the experiment has a 4 mm thickness and is exceptionally clear. The glass avoids loss by isolating the absorbent plate from the outside air and protecting it from dust and grime.

4.2.5 Absorber plate

The absorbent plate is the most important component of a solar collector. It is installed into the air duct. The bottom is insulated, while the top is made of glass. The absorbent board transforms solar energy into thermal energy. It is formed of an absorbent material, such as the aluminum used in the experiment,

and its dimensions are (1200 x 300) mm. It is also colored black, since this helps to increase absorption. Figure (4-7) depicts the absorbent plate. On this absorbent plate, several artificial roughness will be attached.
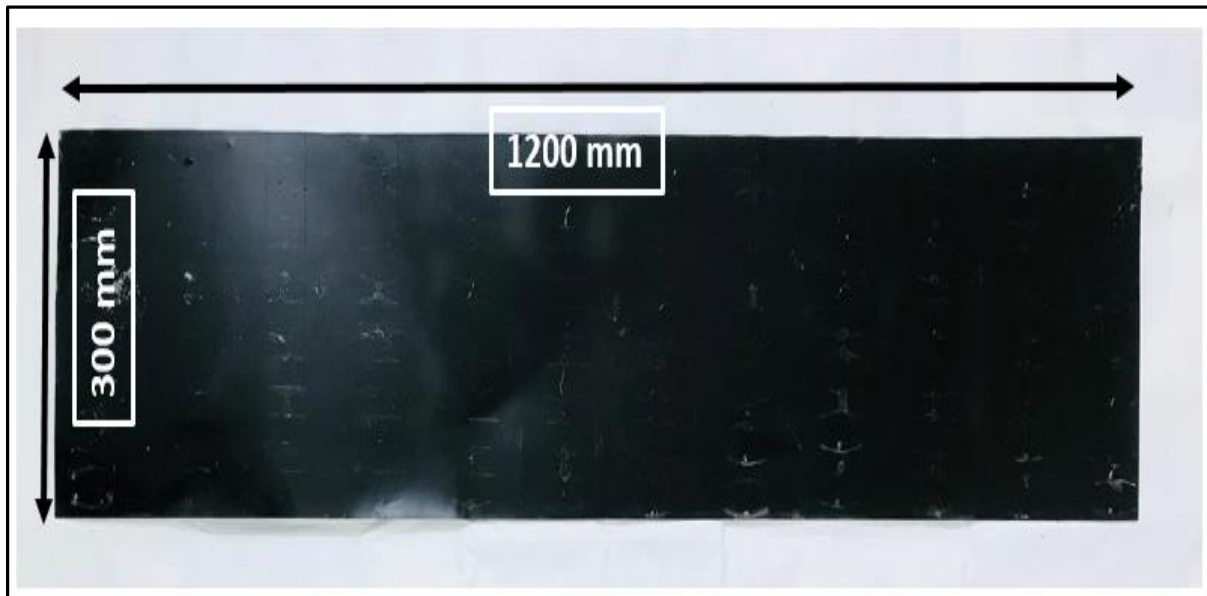
Figure (4-7): Absorber plate

4.3 Measurement instruments

To measure all parameters, the following devices are used

4.3.1 Data logger

It incorporates a 32-channel or more Data Logger AT4532x figure (4-8) that is controlled by a computer, and the flash memory region is powered by direct electrical supply. Utilize this gadget to display temperature information.

Figure (4-8): Data logger AT4532x

4.3.2 Solar power meter measurement device

Figure (4-9) shows the TENMARS (TEM-207) radiation meter, which monitors the intensity of solar radiation directly. For greater precision, while measuring the intensity of radiation, the measuring instrument must be inclined to match the angle of the glass on the test section with an angle of 32º. It is with an accuracy of (± 5%) and of range (0-2000) W/m². Furthermore, the device's calibration results as shown in Appendix [A].

Figure (4-9): Solar power meter.

4.3.3 Wind velocity measurement by Anemometer

Since velocity is a crucial role in improving heat transfer, air velocity must be monitored using an anemometer type (AM-4206M), shown in the figure (4-10). In addition, the anemometer's standards provide for accuracy of (5%) throughout a range of (0.4 – 35) m/sec. was used to track the velocity of the wind. Calibration is performed at the Diwaniyah meteorological station. The device's calibration results are shown in Appendix [B].

Figure (4-10): Wind velocity measurement by Anemometer

4.3.4 Temperature sensor thermocouples

Inside and outside the SAH, a K-type thermocouple recorded temperatures to an accuracy of (0.5 % $\pm$ 1 $^{\circ}$C) and range temperature from (-40 to 260 $^{\circ}$C). The temperature spread as follows to measure the predicted temperature in the solar heater on three sections: entry, exit, and the test portion, specifically, the thermocouple calibration involves taking readings at three different points: at ambient, ice, and steam. As shown in Appendix-[C], temperature readings may be taken using a mercury thermometer and a variety of temperature sensors connected to a multi-channel data logger of the AT4532 kind. Used k-type

thermocouples in figure (4-11). shows the arrangement of thermocouples over an absorber plate in figure (4-12).

➢ Six sensor fixed in test section for smooth duct

➢ Six sensor fixed in test section for rough duct

➢ One sensor in inlet for each devices

➢ One sensor in outlet for each devices

➢ One sensor to measure glass temp.

➢ One sensor to measure ambient temperature.

Figure (4-11) thermocouples k-type
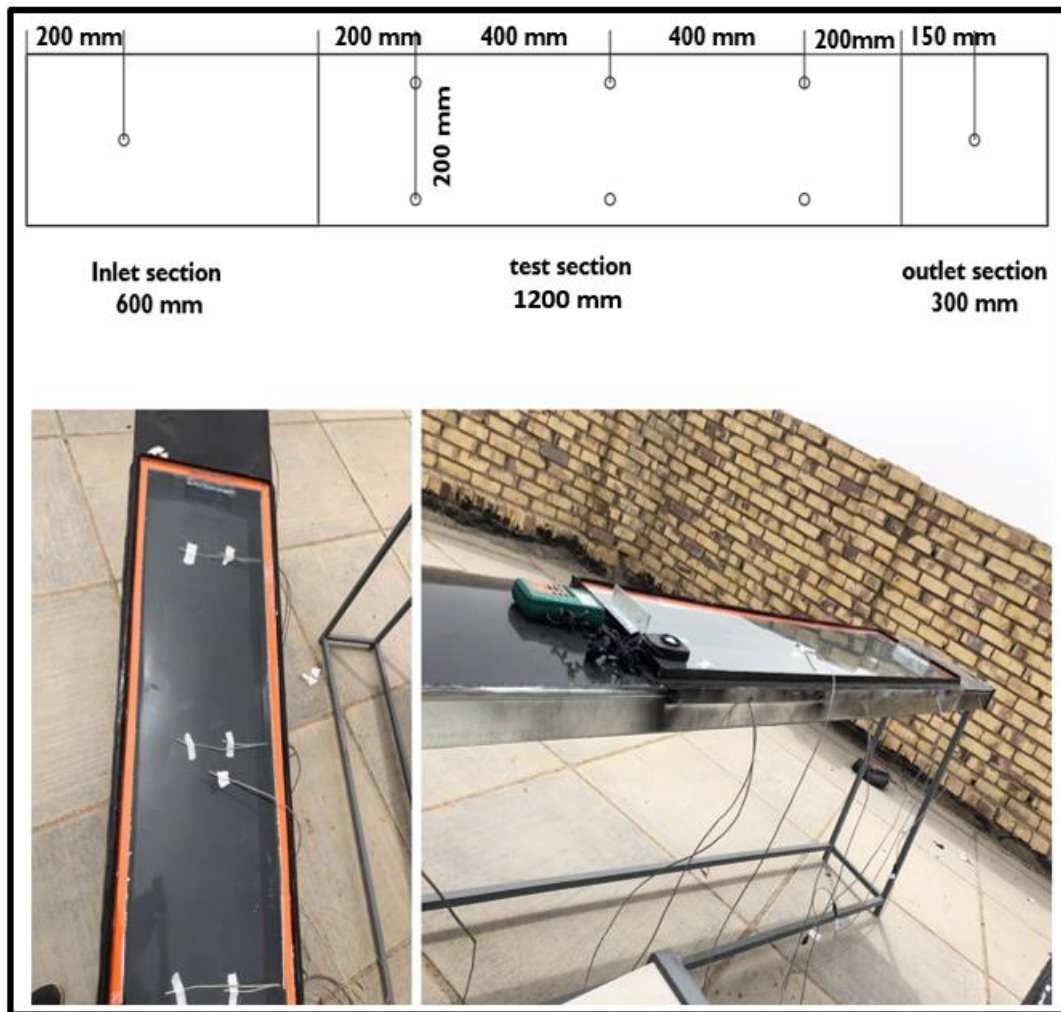
Figure (4-12) positions of thermocouples.

4.3.5 Digital manometer (pressure differential)

The pressure drop over the collector was measured with a calibrated digital manometer (512 type) in this investigation. Between the SP-SAH's inlet and exit ducts is a digital manometer with the following specifications: operating range of (0 to 35.0) kPa, an accuracy of (0.5%) of the whole scale , and a resolution of (0.01 kPa). As shown in figure (4-13).
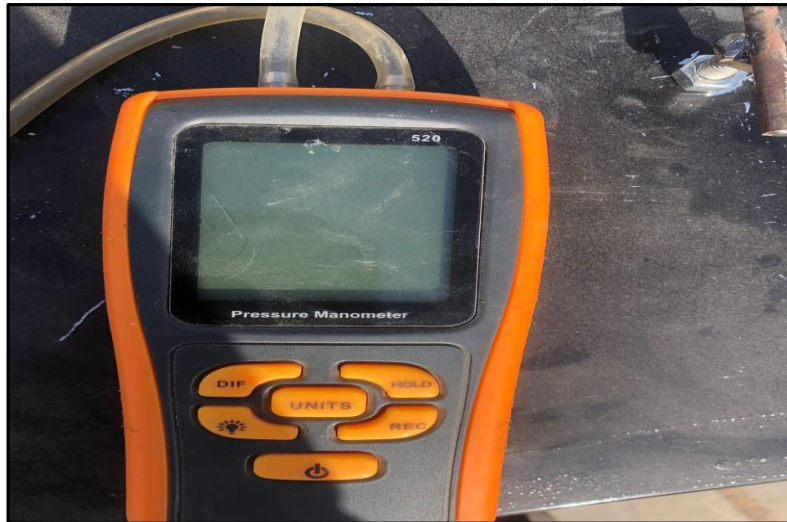
Figure (4-13): Digital manometer

4.4 Experimental analysis

The Nusselt number, the friction factor, and the thermal improvement coefficient are used to depict the experiment's dimensionless outcomes.

In the steady state, the rate of heat transfer is determined by assuming that the rate of heat loss equals the rate of heat transfer. From eq. (1), (2) and (3)[46]

$$Q_{air} = Q_{absorber\ plate} \qquad\qquad (4.2)$$

$$where: Q_{air} = \dot{m}C_{p,air}(T_{out} - T_{in}) \qquad\qquad (4.3)$$

The test part's convective heat transfer may be expressed as follows:

$$Q_{absorber\ plate} = hA(T_{ap} - T_{am}) \qquad\qquad (4.4)$$

In which[47]

$$T_{am} = \frac{(T_{out} + T_{in})}{2} \qquad\qquad (4.5)$$

And temperature of absorber plate [47]

$$T_{ap} = \sum T_{ap}/6 \qquad\qquad (4.6)$$

The average heat transfer coefficient that used from experimental data and after that calculation Nusselt Number Nu from the following expression[48]:

$$h = \frac{\dot{m} C_{p,air}(T_{out} - T_{in})}{A(T_{ap} - T_{am})} \tag{4.7}$$

and to calculated the hydraulic diameter for rectangular duct[49]:

$$D_h = \frac{2ab}{a+b} \tag{4.8}$$

So now calculated Nusselt number from obtain equation [50]:

$$Nu = \frac{hD_h}{k} \tag{4.9}$$

Reynolds number obtain from next equation [50]

$$Re = \frac{\rho v \, D_h}{\mu} \tag{4.10}$$

Friction factor that calculated pressure drop given by[48]:

$$f = \frac{2}{L/D_h} \frac{\Delta P}{\rho v^2} \tag{4.11}$$

Thermal enhancement factor that expression relative to the smooth duct given by[51]:

$$TPF = \frac{(Nu_r / Nu_s)}{(f_r / f_s)^{\frac{1}{3}}} \tag{4.12}$$

The equation of thermal efficiency give by [51]:

$$\eta = \frac{Q_{air}}{A_c I} \tag{4.13}$$

4.5 Experimental process

One, the measurement devices must be placed and secured in place once the module has been assembled. The following is a possible explanation for the utilized measurement tools.

1. Thermocouples: a K-type thermocouple is used to detect temperatures at six different spots throughout the test portion, including the intake, the outlet, and the glass. An alcohol thermometer is used to calibrate each thermocouple to guarantee precision. Connected to a 32-channel data recorder , the thermocouples save data for subsequent analysis.

2. To provide an accurate reading of the amount of solar radiation falling at a certain angle per hour, a Pyranometer is installed on the solar still and tilted to the same degree as the front glass cover. Appendix C displays the calibration for the pyranometer.

3. Anemometer: a wind speed sensor installed at the duct's output at several heights to measure the hourly average wind speed in the area. Appendix D also displays the results of calibrating the wind speed sensor.

4. To determine the pressure differential between the two test portions, a digital pressure manometer is fastened to the duct's inlet and outlet.

5. The instruments for gauging are activated all of the measurable data is recorded either automatically (temperature) or manually every half hour throughout the experiment's time window of 8:00 am to 3:00 pm (wind speed, solar radiation, and pressure).

6. The studies are conducted on the house's rooftop in Diwaniya. Modify the test section and the absorber plate's simulated roughness. The studies were conducted between 18 April and 10 May .

Chapter Five
Results and dissection

Chapter Five

Introduction

In this chapter presents the outcomes of our numerical analysis and the measured data. The results presented here compare the performances of (SP-SAH) with and without artificial roughness, analyzing the impact of solar radiation and air flow rate and the relative roughness of pitch and length at a fixed angle of attack 60° on the Improve heat transfer of turbulent flow through forced convection. Finally, the validity of the numerical results was confirmed by comparison with the experimental measurements. At last, a contrast is shown between the current model and earlier research. For this study, we carry out the following experiments and calculate the following numerical results:

1. The results of the practical study.

2. The results of the numerical analysis.

3. Comparison of experimental and numerical results

4. Numerical validation of the study.

5.1 Validation of the results

We can see the impact of changing the flow and roughness parameters on the heat transfer and frictional qualities of air passing through a rectangular channel in the figures below. When the smooth channel was present and functioning, the experimental and theoretical results were compared to those obtained when the rough channel was present and functioning under identical conditions. An experimental calculation of the f and Nu for a smooth plate was used to verify the concept. An ordinary Nu and f equation are used to evaluate the smooth plate's output against the expected values. As shown below, the Dittus-Boelter equation [46] [52]may be used to calculate the Nu for a rectangular

duct of uniform thickness, whereas the Blasius equation [53] can be used to get the f.

To valid Nusselt number for the smooth SAH using the correlation equation from the Dittus-Boelter [53] given by shown in figure (5-1):

$$Nu = 0.023 Re^{0.8} Pr^{0.4} \qquad\qquad (5.1)$$

Gnielinski Equation given by[41]:

$$Nu = \frac{\left(\frac{f}{8}\right)(Re-1000)Pr}{1+12.7\left(\frac{f}{8}\right)^{\frac{1}{2}}\left((pr)^{\frac{2}{3}}-1\right)} \qquad\qquad (5.2)$$

Where $for\ 3000 < Re\ < 5*10^6$
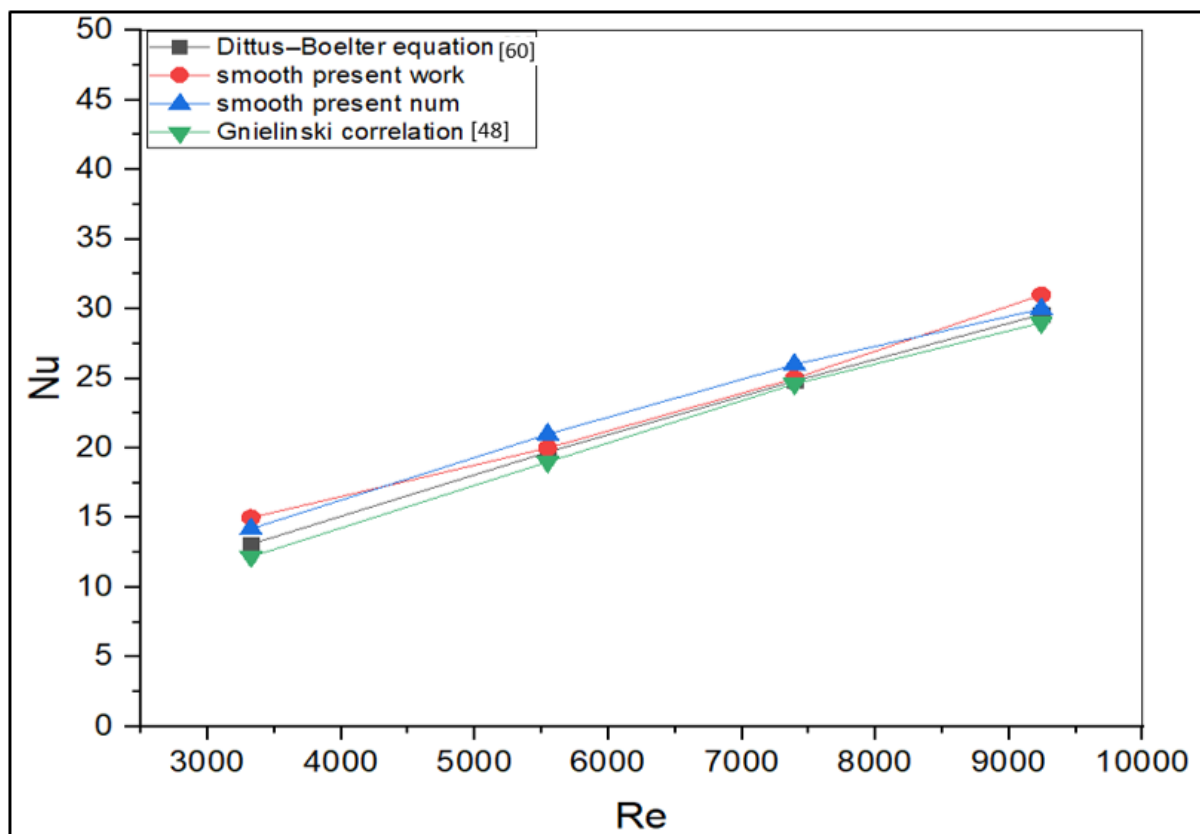
Figure (5-1): comparison of present work for smooth duct with correlation eq. for Nu.

To validate the friction factor for the smooth SAH using the Blasius correlation equation provided by [54] that is shown in figure (5-2):

$$f = 0.316Re^{-0.25} \quad \text{For } 3000 \leq R \leq 20000 \quad\quad\quad (5.3)$$

Petukov Equation given by[54]:

$$f = (0.79 \ln Re - 1.64)^{-2} \quad \text{For } 3000 < Re < 5 \times 10^6 \quad\quad (5.4)$$
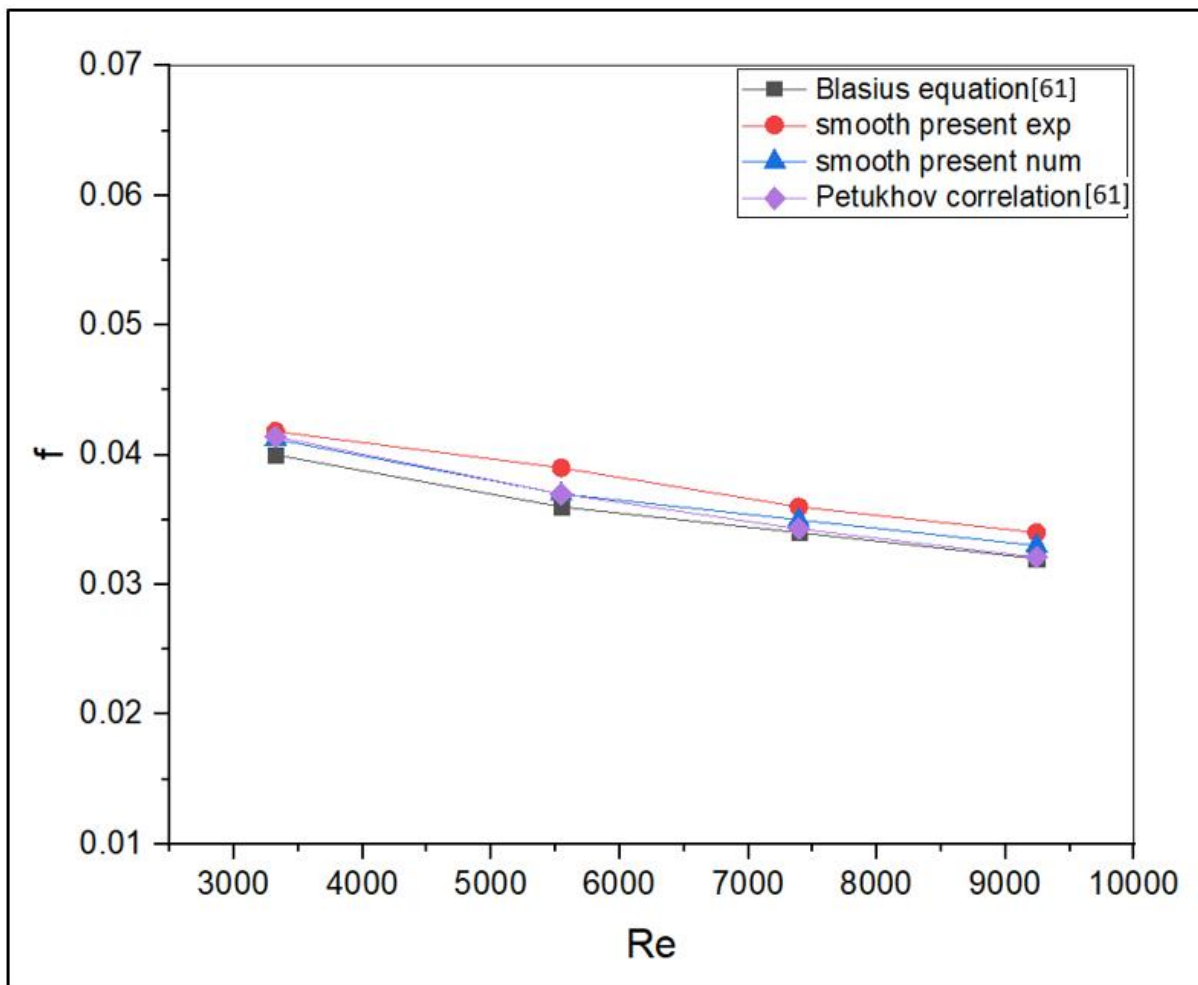
Figure (5-2): Validation of friction factor

An experimental test of the SAH was performed with the presence of artificial roughness and smooth duct. In the city of Diwaniyah between 18 April and 5 May, 2022. In Iraq, at 32°N and 45°E, the city of Diwaniyah is located. The wind speed on all test days was between (0.3 and 9.72) m/s. Two solar air heaters, one with arc-shaped synthetic roughness and one with S-shaped synthetic roughness, were tested and compared with a standard SAH. The Re varied during the experiments from 3000 to 10000.

The numerical study was carried out under the same conditions and parameters in which the experimental study were conducted. Figures (5-3 to 5-6) show a comparison between the result of Nu numerical and experimental for the present work with different Reynolds number rates. The experimental and numerical findings exhibited a high degree of concordance.

Figures (5-7 to 5-10) compare the experimental and numerical results of the friction factor for the current work at different Reynolds number rates. The experimental and numerical results matched up rather well.
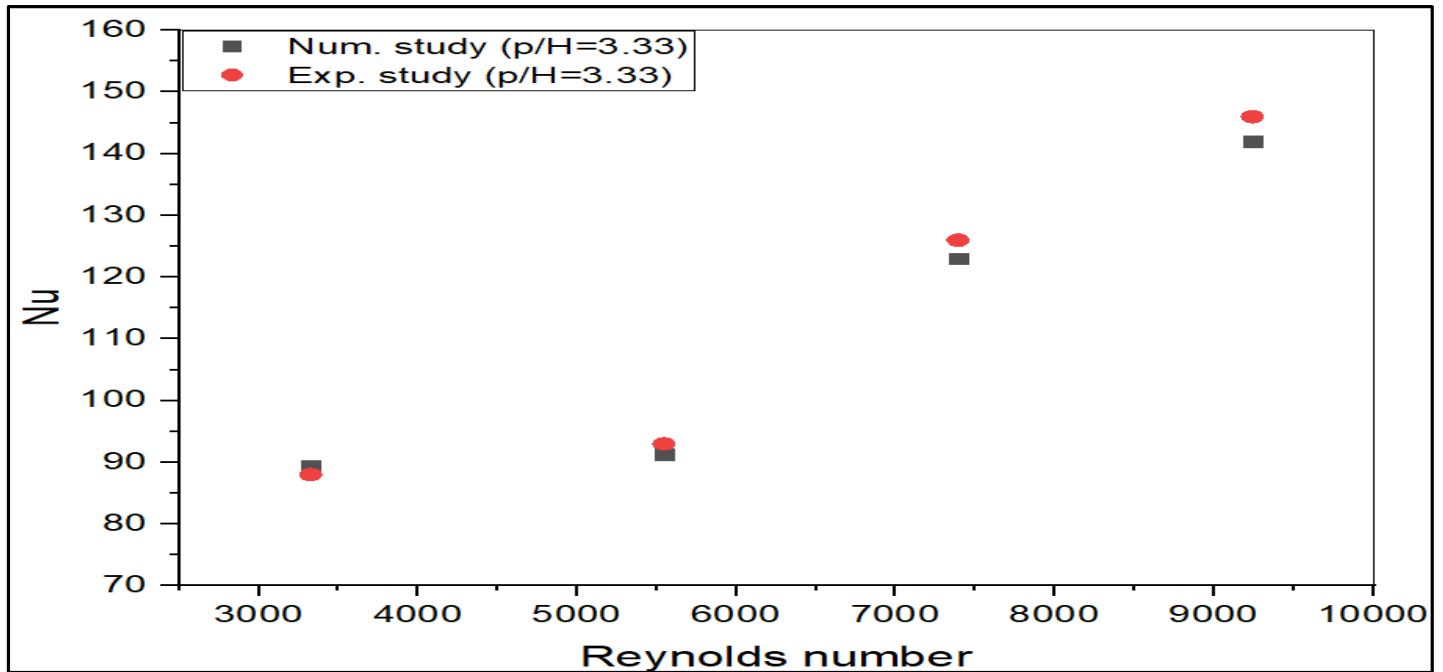
Figure (5-3): Compare the results of the Nu numerical and practical at p/H =

3.33 for an S-shaped inline arrangement.
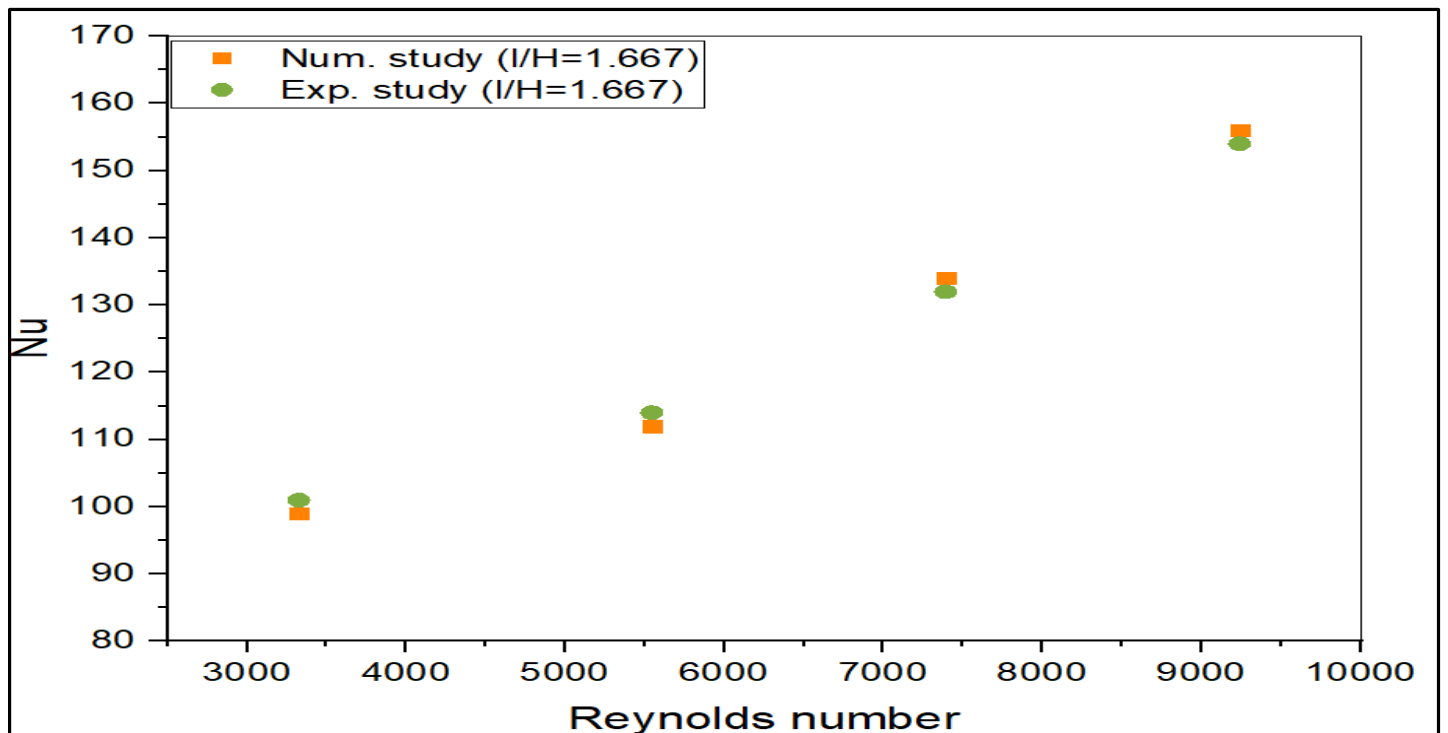
Figure (5-4): Compare the results of the Nu numerical and practical at l/H =

1.667 for S-shape staggered arrangement

.
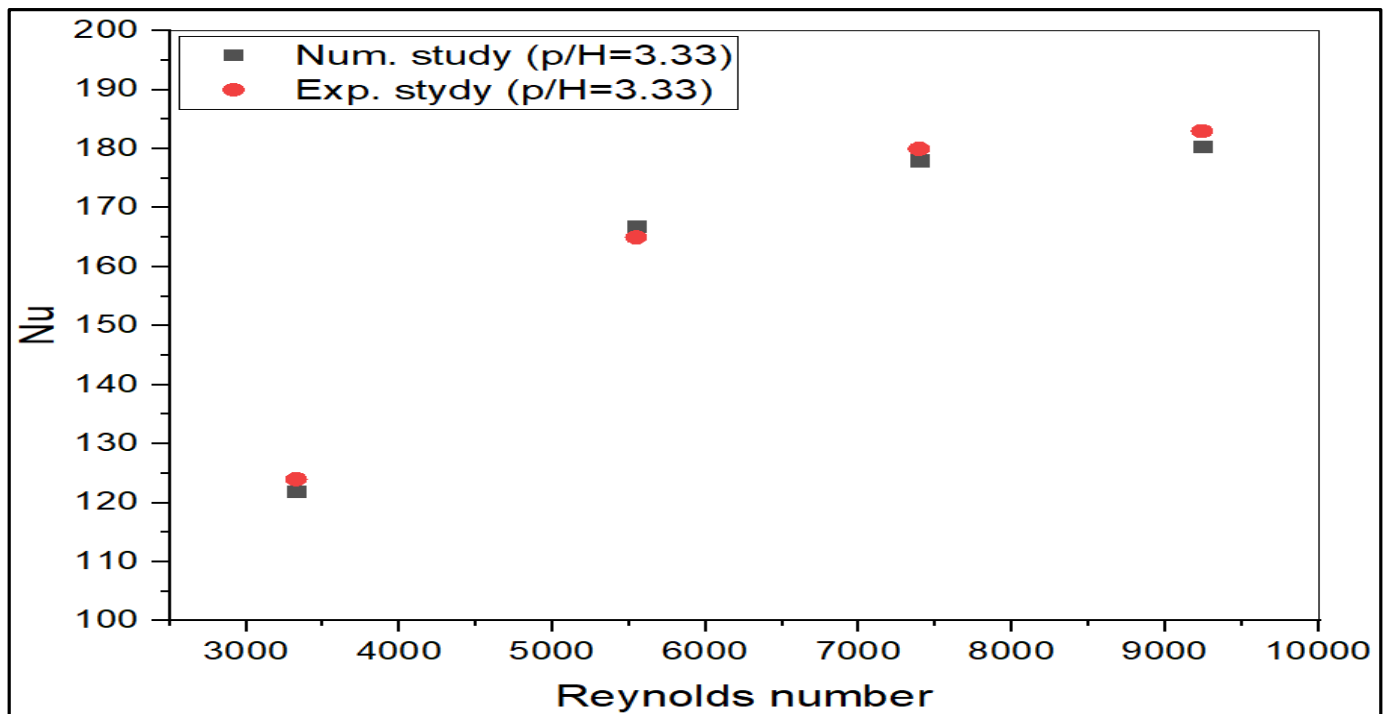
Figure (5-5): Compare the results of the Nu numerical and practical at p/H =

3.33 for arc-shape inline arrangement.
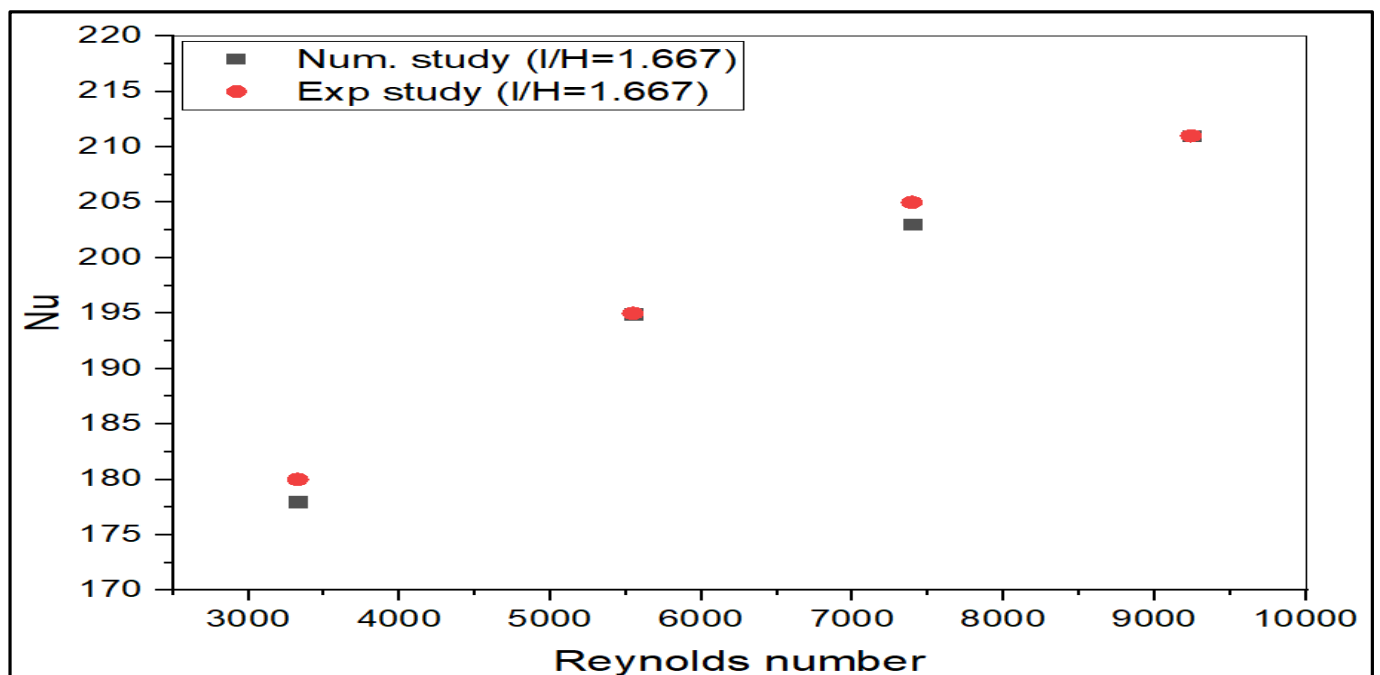
Figure (5-6): Compare the results of the Nu numerical and practical at l/H =

1.667 for arc-shape staggered arrangement.

73
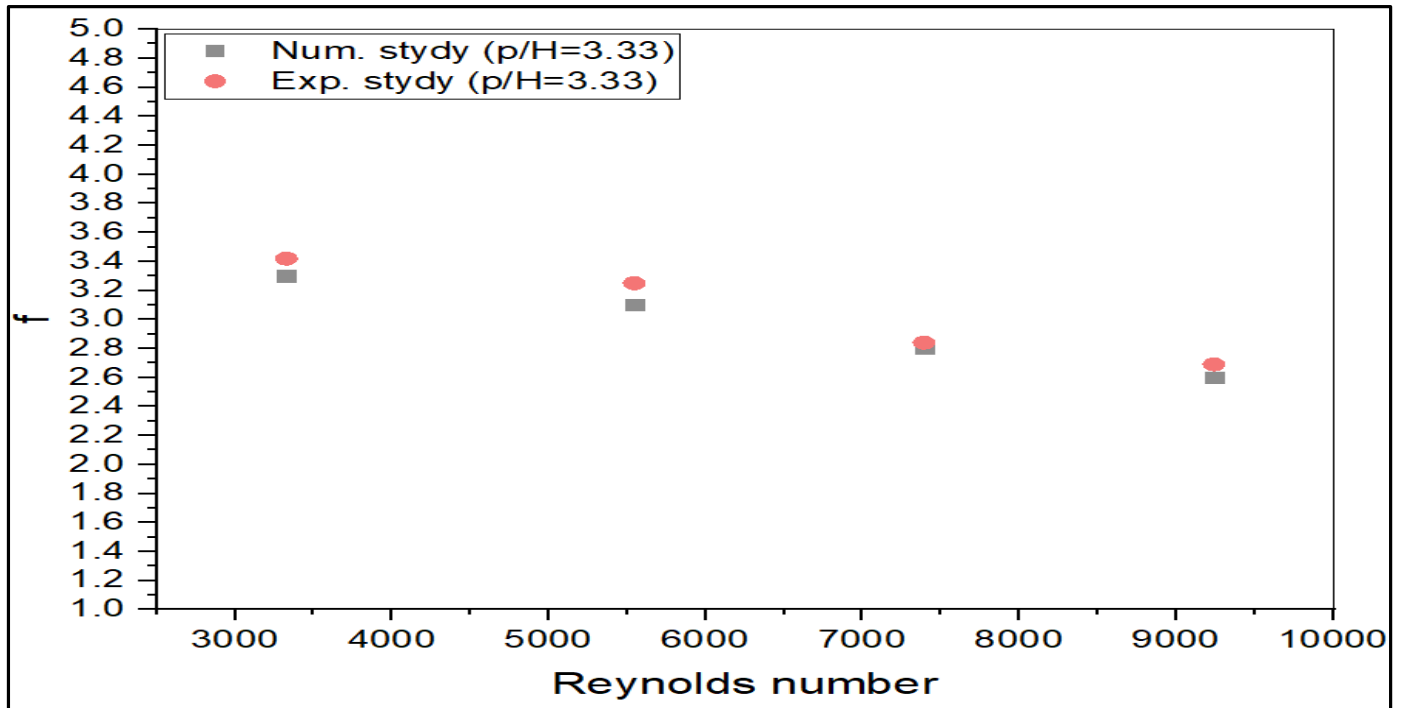
Figure (5-7): Compare the results of the f numerical and practical at p/H = 3.33

for S-shape inline arrangement.
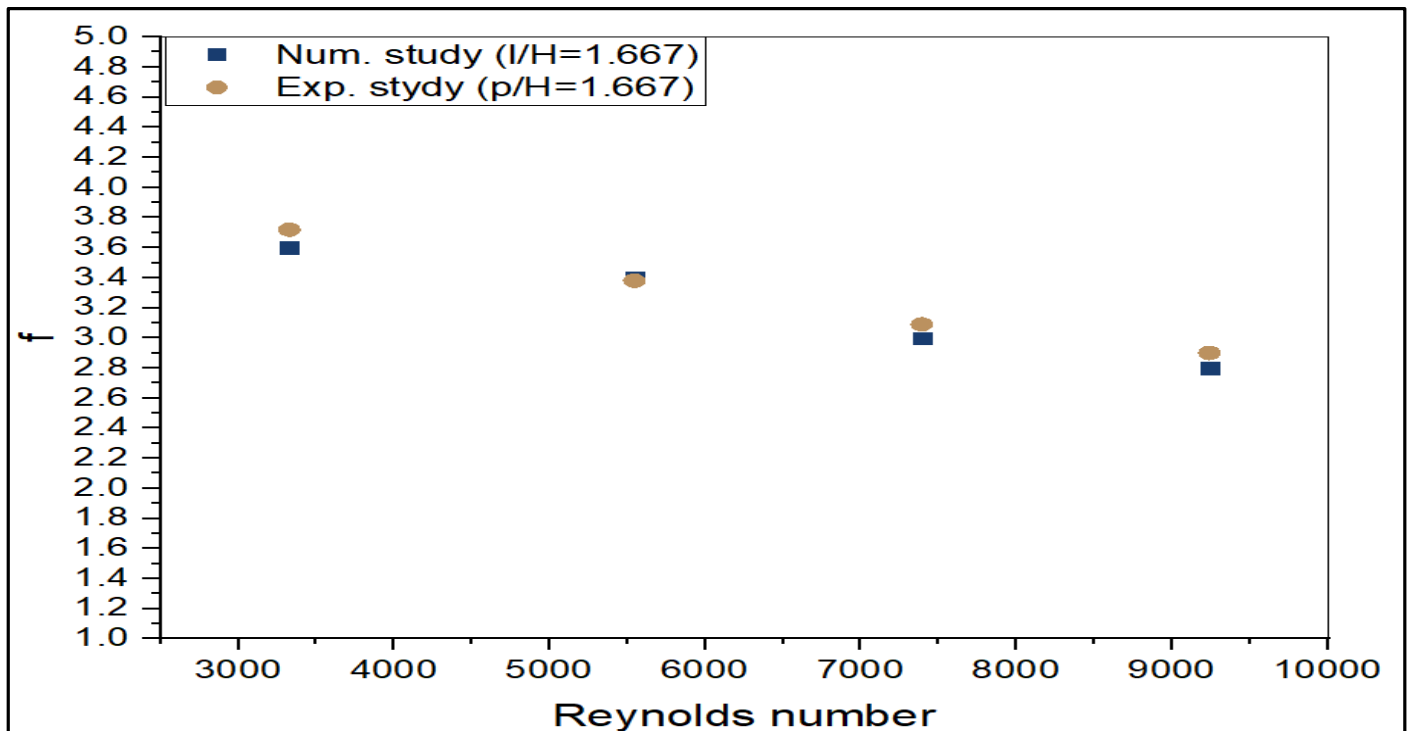
Figure (5-8): Compare the results of the f numerical and practical at l/H = 1.667

for S-shape staggered arrangement
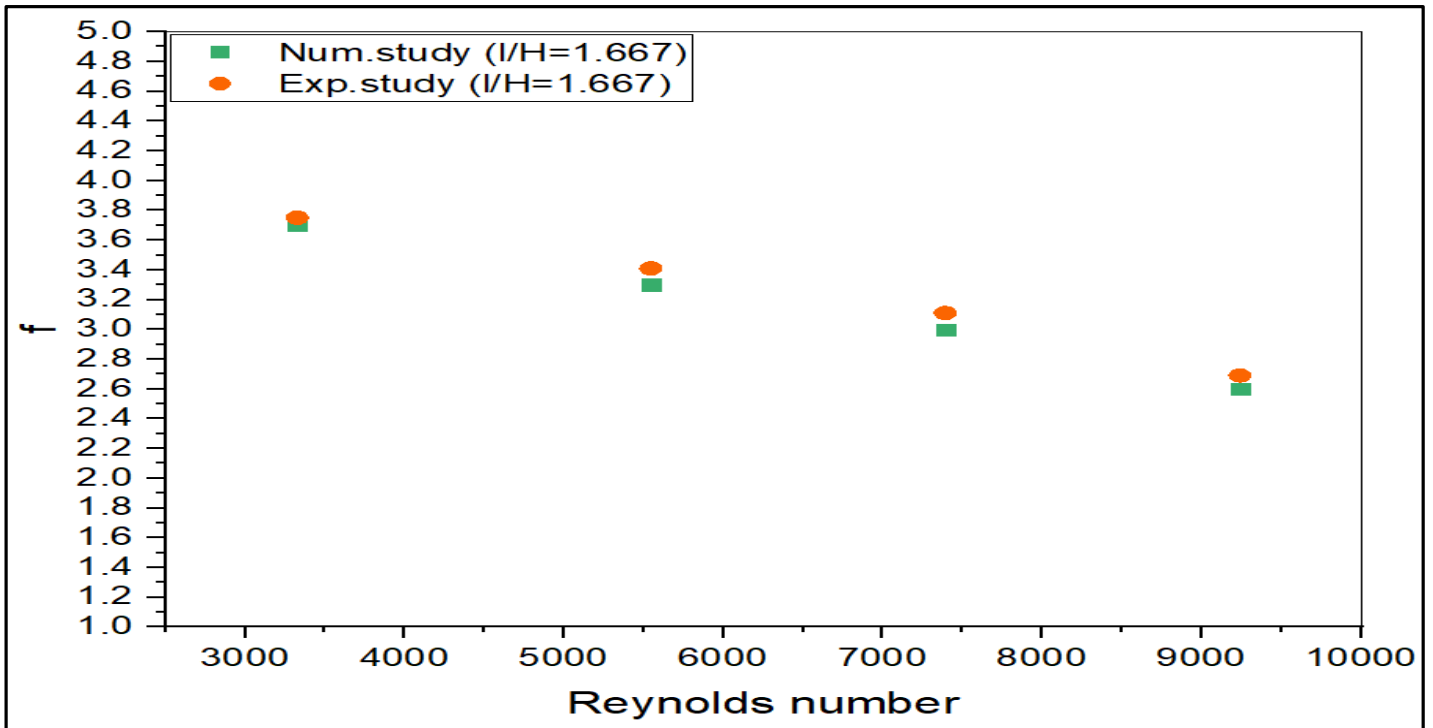
Figure (5-9): Compare the results of the f numerical and practical at p/H = 3.33

for arc-shape inline arrangement.
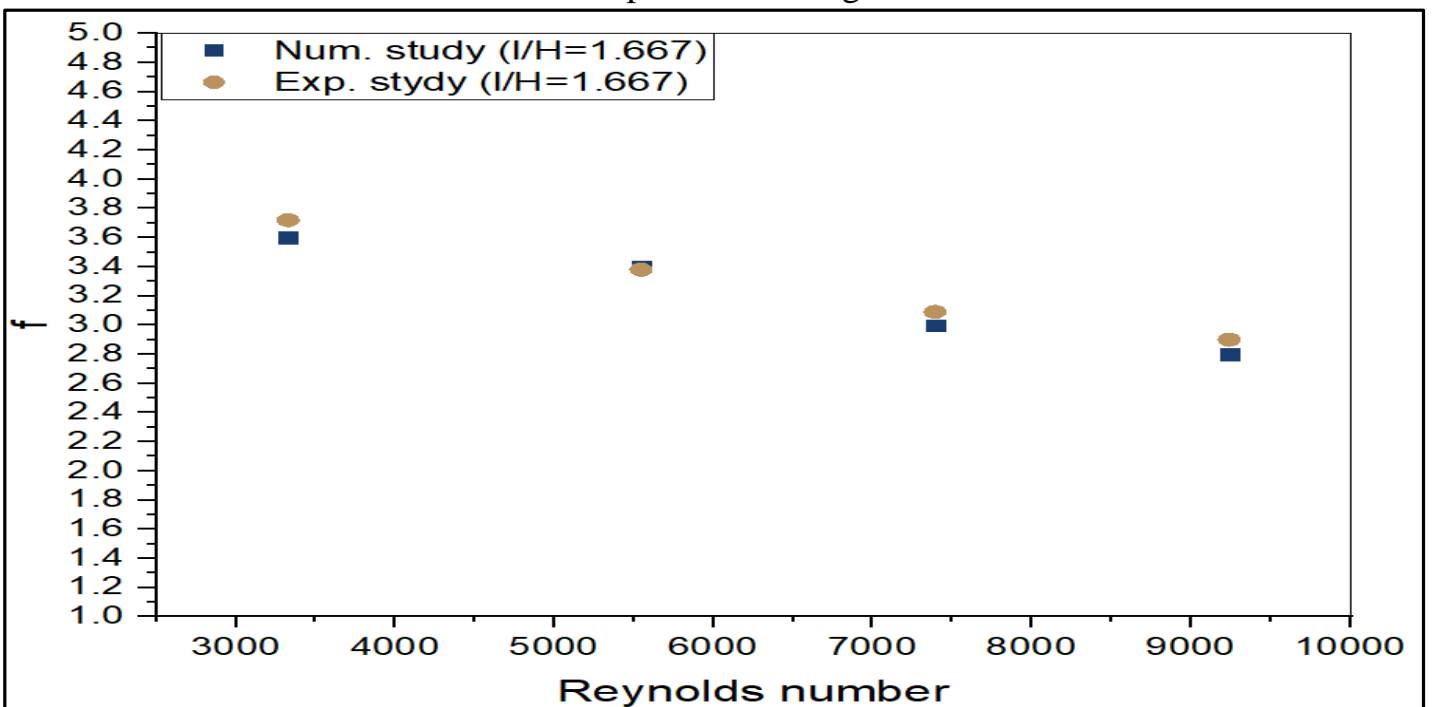
Figure (5-10): Compare the results of the f numerical and practical at l/H =

1.667 for arc-shape staggered arrangement.

5.2 Effect of solar irradiance

Figure (5-11) illustrates diversity of global solar radiation over the length of the day for the working hours from 8 A.M. until 3 P.M. According to the four different days, the figure shows that the gradual increase of global solar radiation until it reaches its maximum value of 1036 (W/m^2) at mid-noon and then gradually decreases until it reaches its minimum and also show the influence in some hours that because of the clouds, shadows, and dirt. The solar radiation meter installed with the tilt angle at the same angle of inclination as the solar collector to take real readings of the solar radiation falling on the solar collector.
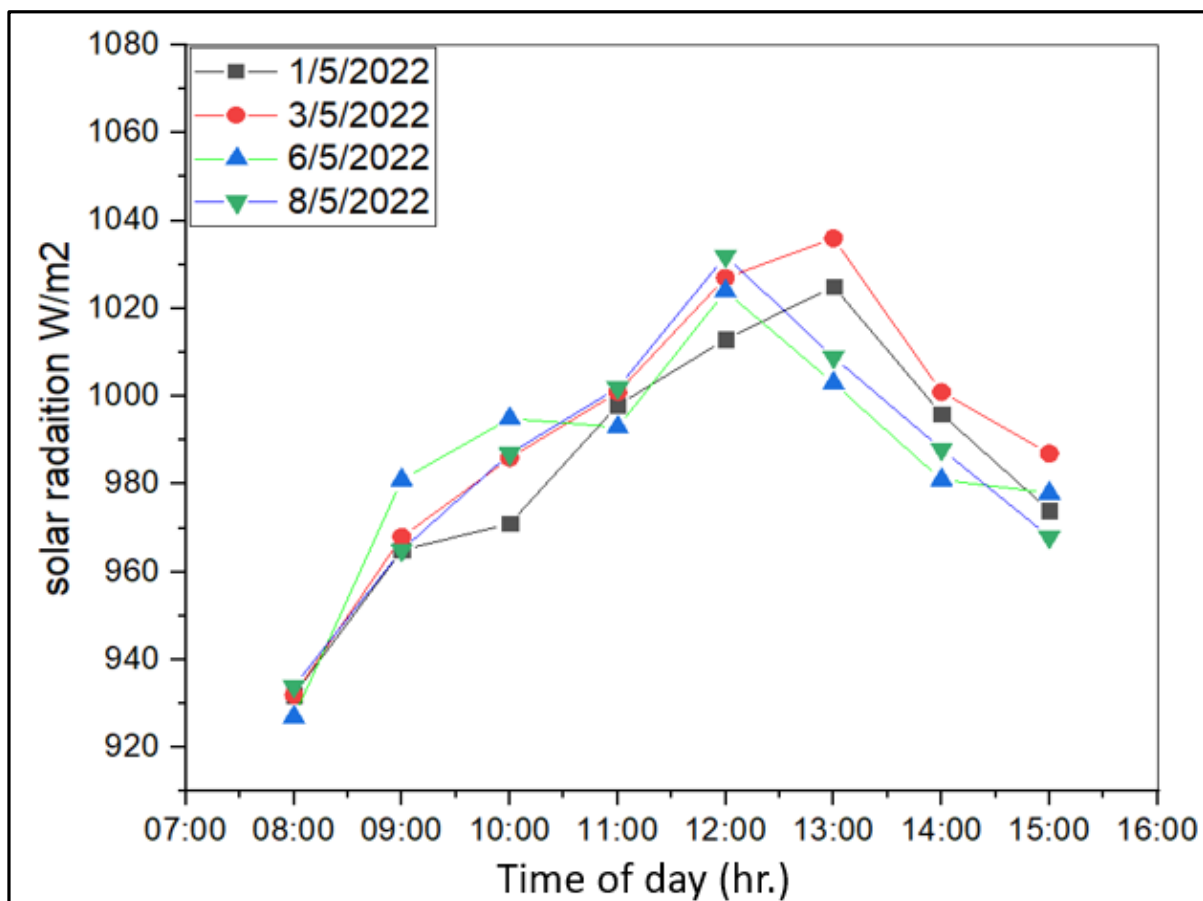
Figure (5-11): The global solar radiation

5.3 Velocity distribution study

Figure (5-12) shows velocity contours for airflow along the SP-SAH at v=2 m/s, and at p/H=3.33 at different x/L from (0.6, 0.7, and 0.8) (a) inline arc, (b) staggered arc (c) inline S-shaped (d) staggered S-shaped. This figure show the velocity contour at parameters p/H = 3.33 of the figure (a & c) in inline order. In addition, at l/H = 1.667 of the staggered shape of the figure (b & d), at Re=7393 it is noticed that secondary vortices form under the primary vortices opposite to the primary vortices, causing an increase in air mixing. This happens in the staggered figure shown in Figure (b & d), which is more than inline in (a & c).

5.4 Temperature distribution study

Figure (5-13) shows that temperature distribution across the cross-sectional region, the X-direction. To know the effect of the synthetic roughness of the shape (arc and S-shape) in the inline and staggered arrangement at p/H = 3.33 and l/H = 1.667, respectively. It is possible to see it at a velocity of 2 m/s at Re=7393. Figure (b & d) with a staggered arrangement shows the temperature distribution is better than the values of (a & c). The most important heat transfer mechanisms are the transfer of momentum between the main corners and vortices and the interaction of these vortices with the boundary layer on the surface of the absorbent plate.
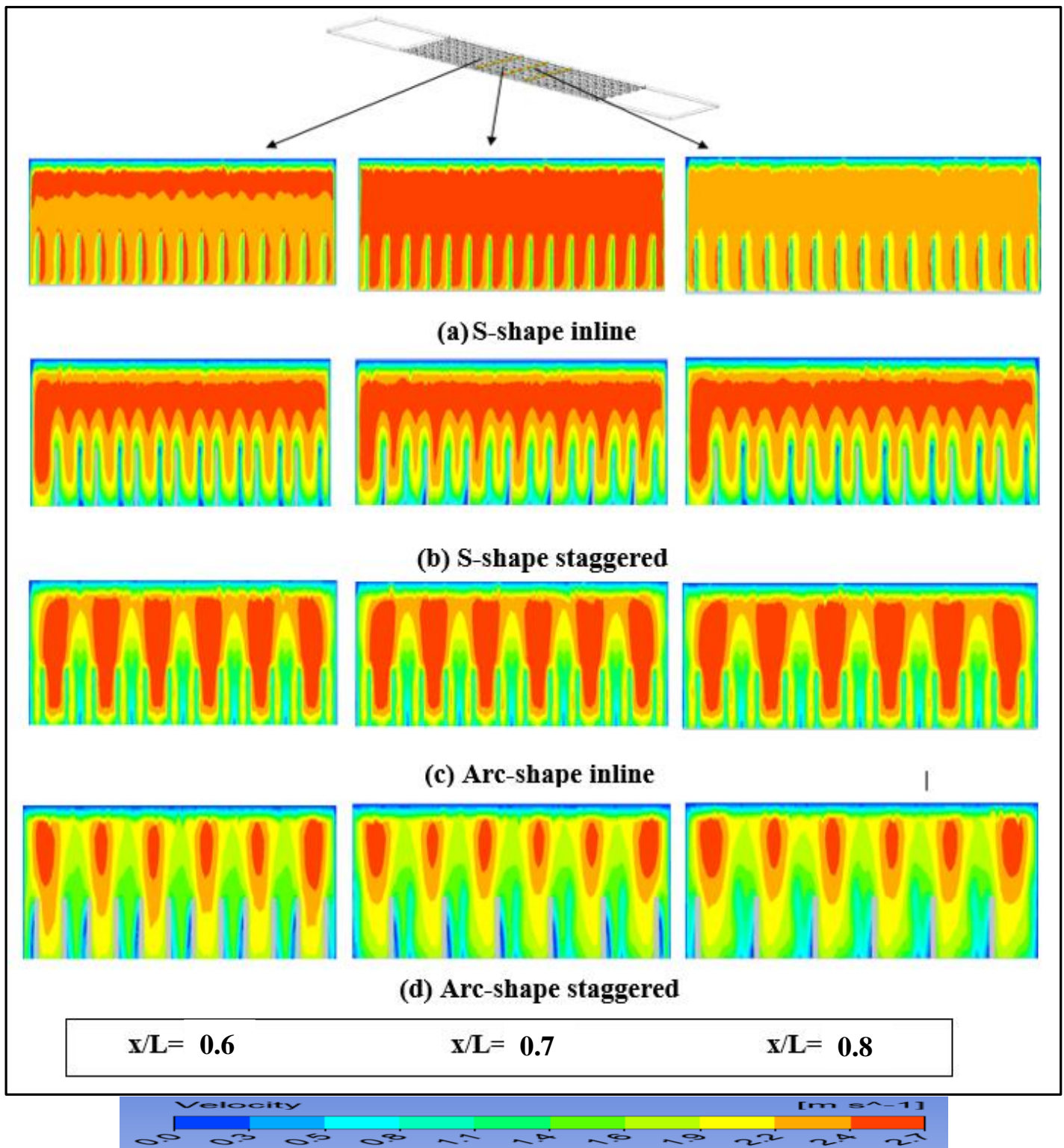
Figure (5-12): Velocity contours for airflow along the SP-SAH at v=2 m/s, and at p/H=3.33 at different x/L :(a) S-shape inline, (b) S-shape staggered (c) Arc shape inline (d) Arc shape staggered.
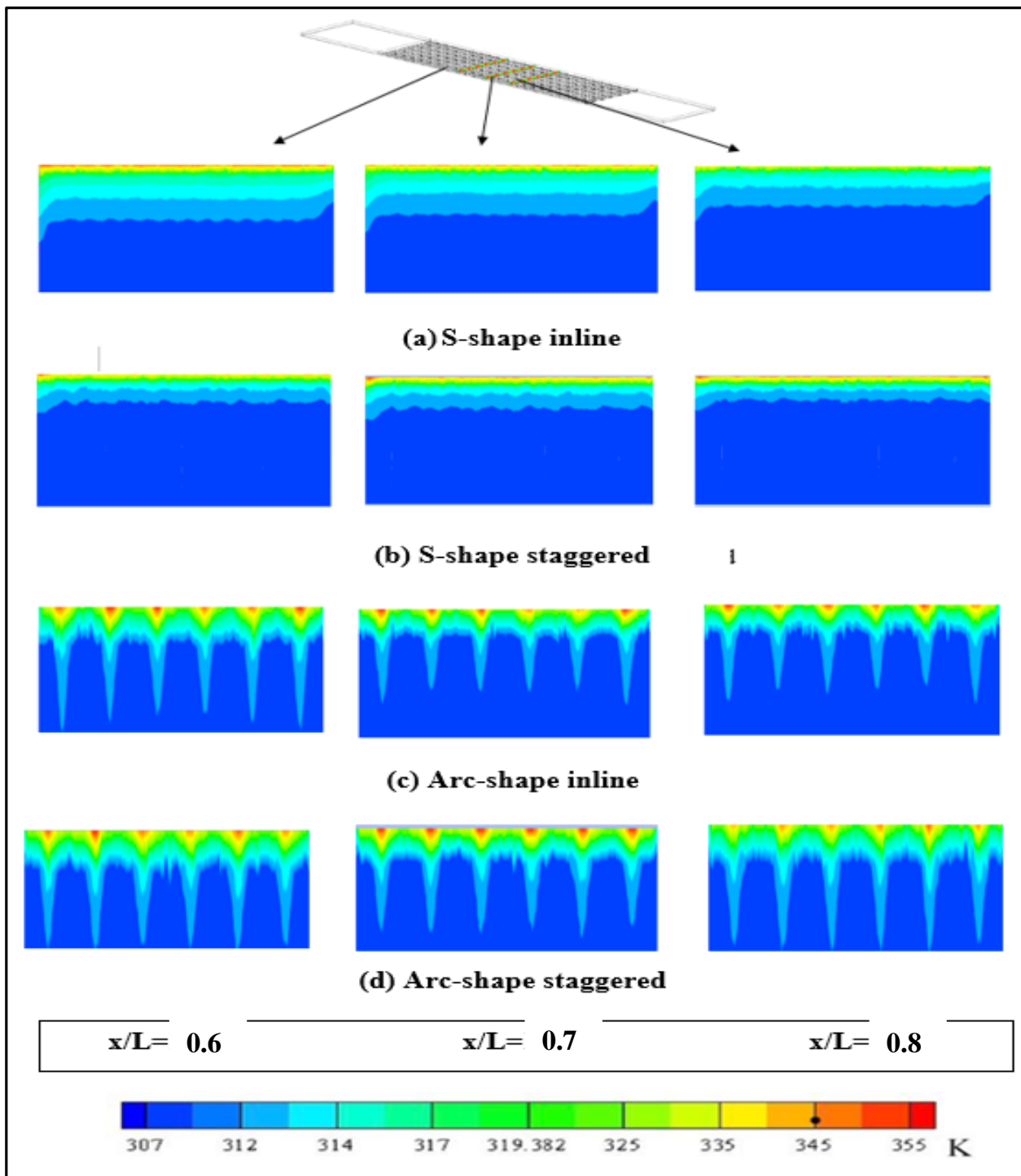
Figure (5-13): Temperature distributions for airflow along the SP-SAH at v=2 m/s, and at p/H=3.33 and l/H=1.667: :(a) S-shape inline, (b) S-shape staggered (c) Arc shape inline (d) Arc shape staggered.

5.5 Influence of p/H on the temperature and velocity distribution.

Figure (5-14) the temperature profiles of the flux on the plate can be illustrated using the artificial S-shaped roughness of inline order. The effect of the S-shaped roughness on the temperature distributions is clearly shown. The first S-shape at x/L=0.4 affects the temperature distribution along the SAH and the channel surface reach to 319 K, especially at x/L=0.95, where the exit temperature is the highest 322 K. This is due to the presence of a separate vortex formed after the first row compresses the main vortex, which enhances fluid mixing and heat transfer in areas close to the absorber plate. A gradual increase in temperature is observed from (x/l = 0.4) to (x/l = 0.95).

Figure (5-14): Temperature and velocity contours for airflow along the SP-SAH at v=1.5 m/s at p/H=3.33 for S-shape inline arrangements.

Figure (5-15) depicts a staggered arrangement of S-shape artificial roughness at Reynolds number (5545) with different x/L, demonstrating that the vortices formed in the first row disrupt the thermal boundary layer. It starts to increase as it increases (x/l). Where it is observed at x/l = 0.4 the temp reach to 320 K, the vortices start with the presence of artificial roughness, and the temperature distribution begins to increase, as a noticeable increase in the speeds resulting from the acceleration of the flow is observed after x/l = 0.6 temp. is 323 K. At x/l = 0.8 temp. is 324K and x/l = 0.95 temp. is 325 K, vortices are formed, which leads to better heat transfer.
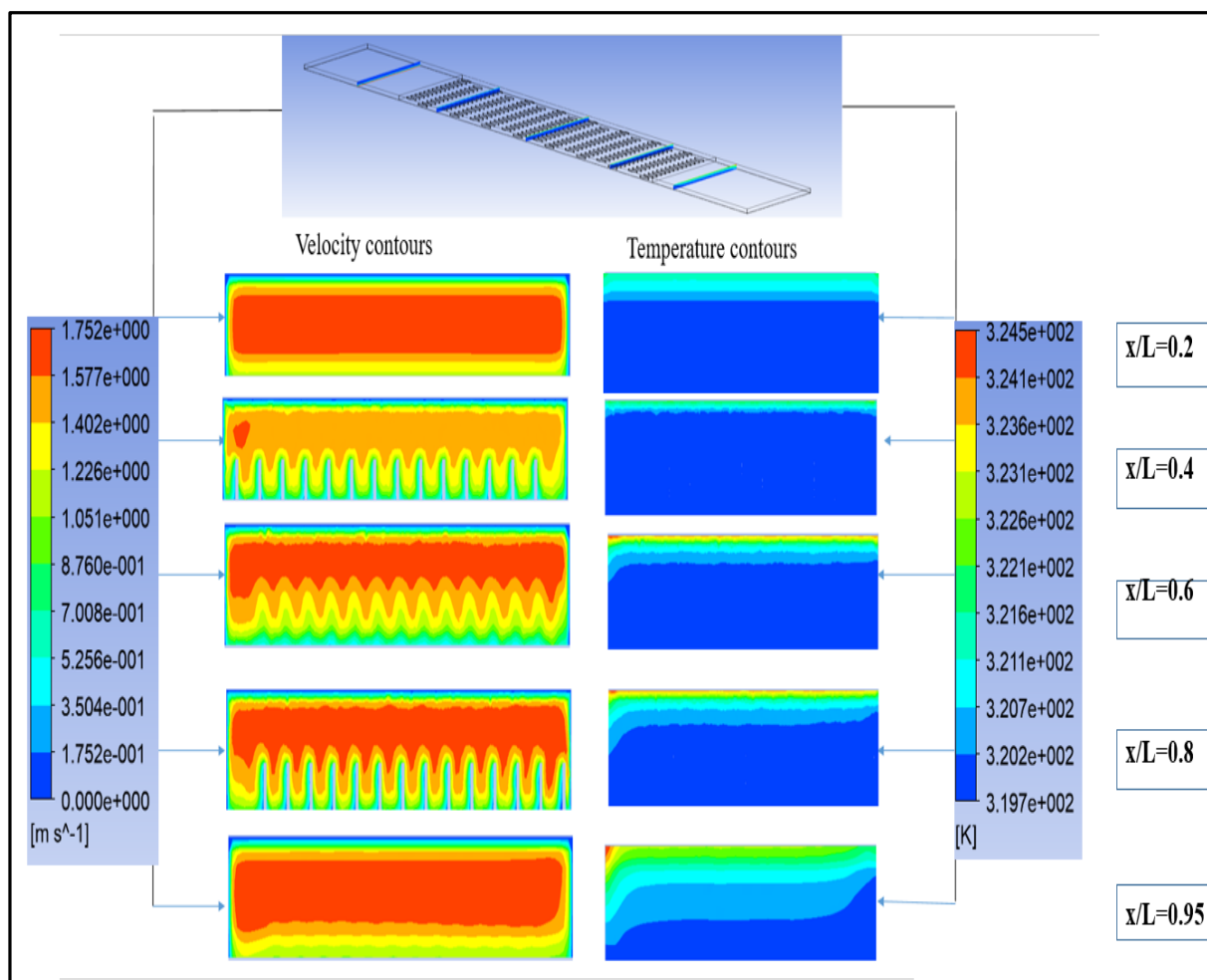
Figure (5-15): Temperature and velocity contours for airflow along the SP-SAH at v=1.5 m/s at l/H=1.667 for S-shape staggered arrangements with different x/L.

Figure (5-16) shows the temperature and velocity distribution of an arc-shaped artificial roughness with inline arrangements with parameters of a constant Reynolds number of 5545 and p/H = 3.33. Where the main vortex is responsible for the deformation of the boundary layer, at x/l = 0.4 the temp is reach 347 K, vortices begin to form that break the boundary layer and the temperature starts to increase. It is observed that the greater the x/l=0.95, the higher the temperature 353 K, and this is due to the high disturbances near the arc near the absorption plate.
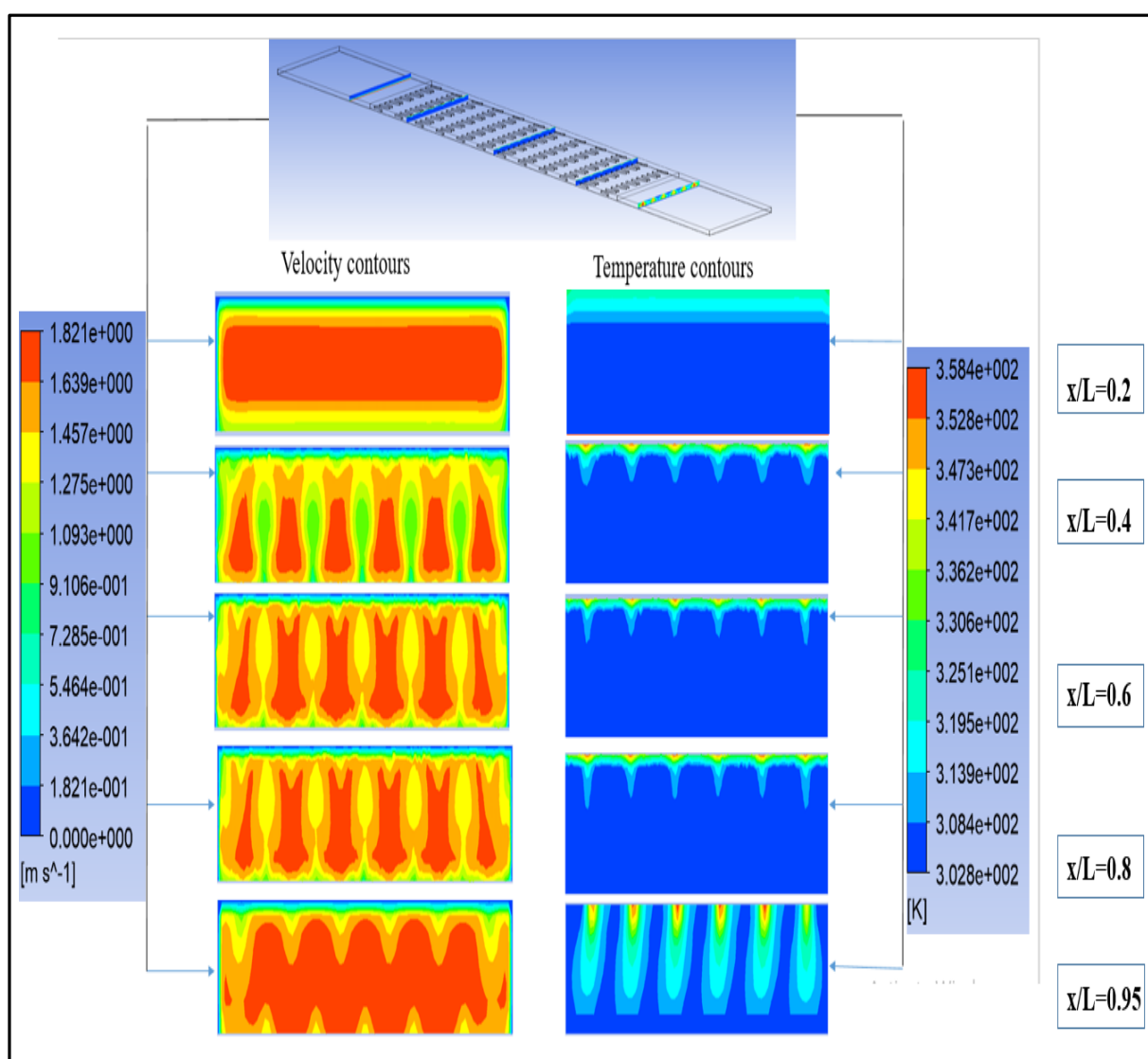
Figure (5-16): Temperature and velocity contours for airflow along the SP-SAH at v=1.5 m/s at p/H=3.33 for arc-shape inline arrangements.

Figure (5-17) shows the temperature and velocity distribution of an arc-shaped artificial roughness with staggered arrangements, with parameters of a constant Reynolds number of 5545, p/H=3.33, and an angle of attack of 60°. Where it can be observed at x/l = 0.4 temp is reach 224 K, temperatures start to rise due to the formed vortices that cause the deformation of the thermal boundary layer. It is noted in the figure that with an increase in x/l = 0.4 to 0.95, temperatures increase until they reach the best improvement at x/l = 0.95 at value 358 K. Where the optimum heat transfer is achieved in an arc shape with a staggered arrangement.
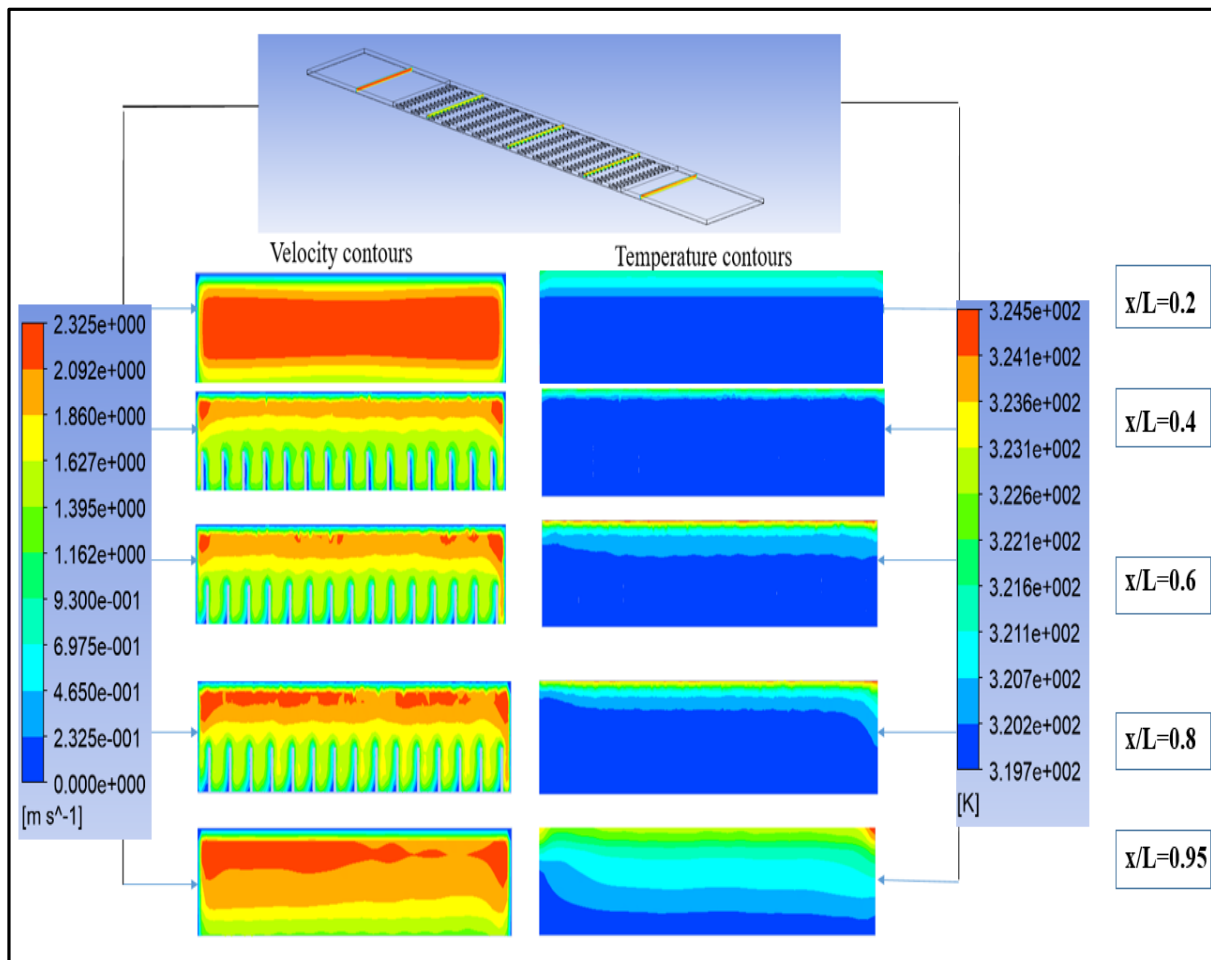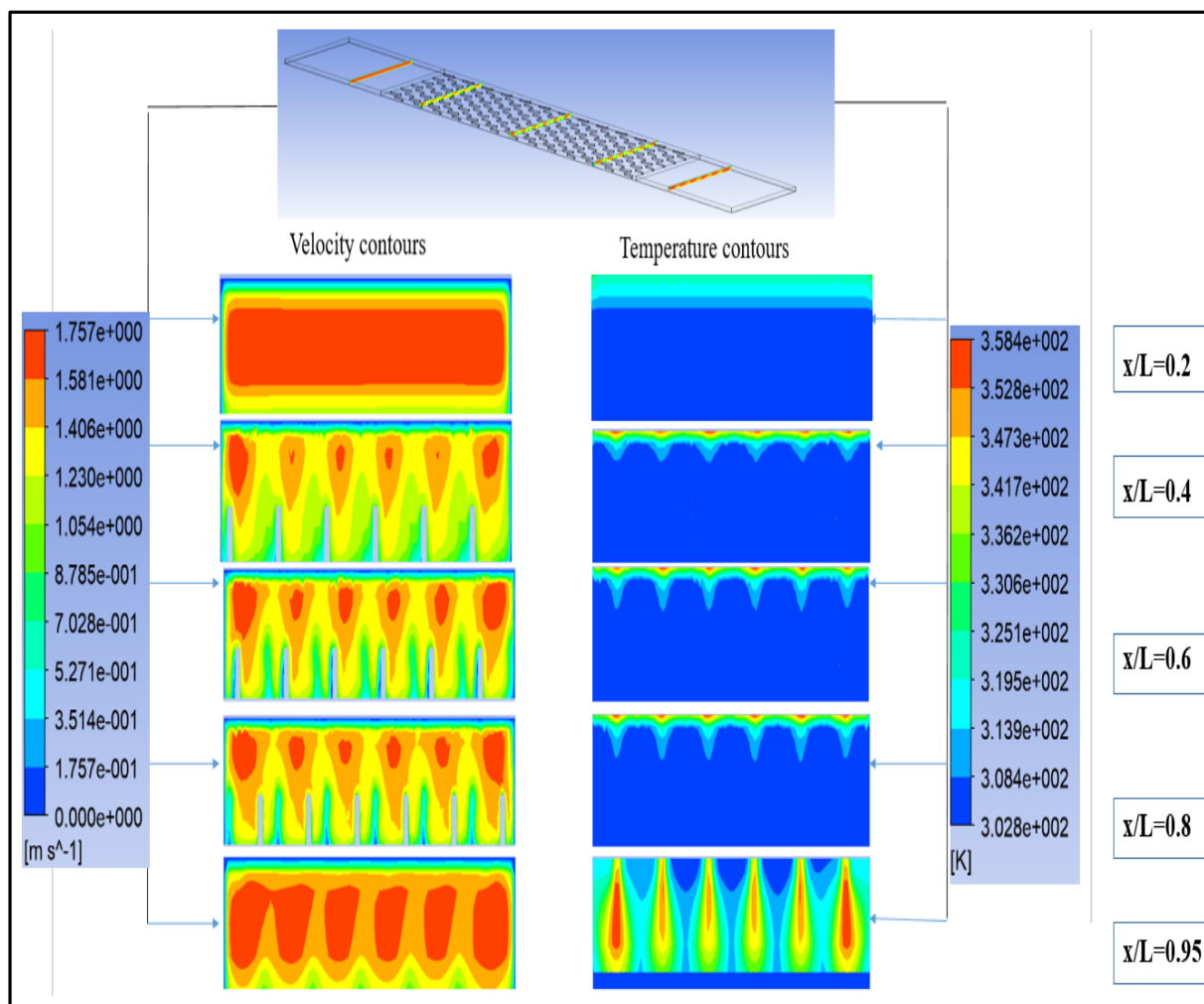

Figure (5-17): Temperature and velocity contours for airflow along the SP-SAH at v=1.5 m/s at l/H=1.667 for arc-shape staggered arrangements.

5.6 Influence of p/H on the Temperature distribution

Figure (5-18) illustrates the temperature contour of the synthetic roughness for the S-shape inline considered in this study, with parameters of Re = 5545, angle of attack of 60°, and p/H = 1.667–6.667. The temperature of the air near the S-shape is higher due to the higher temperature of the S-shape and the change in the flow structure near the S-shape. Where it can be observed that the higher the values of (p/H), the lower the temperature. It is noted in figure (b) that the temperature distribution is better than the rest of the values of (p/H), and the reason for this is that the more (p/H), the fewer reconnection areas the flow.

(a)

(b)

(c)

(d)
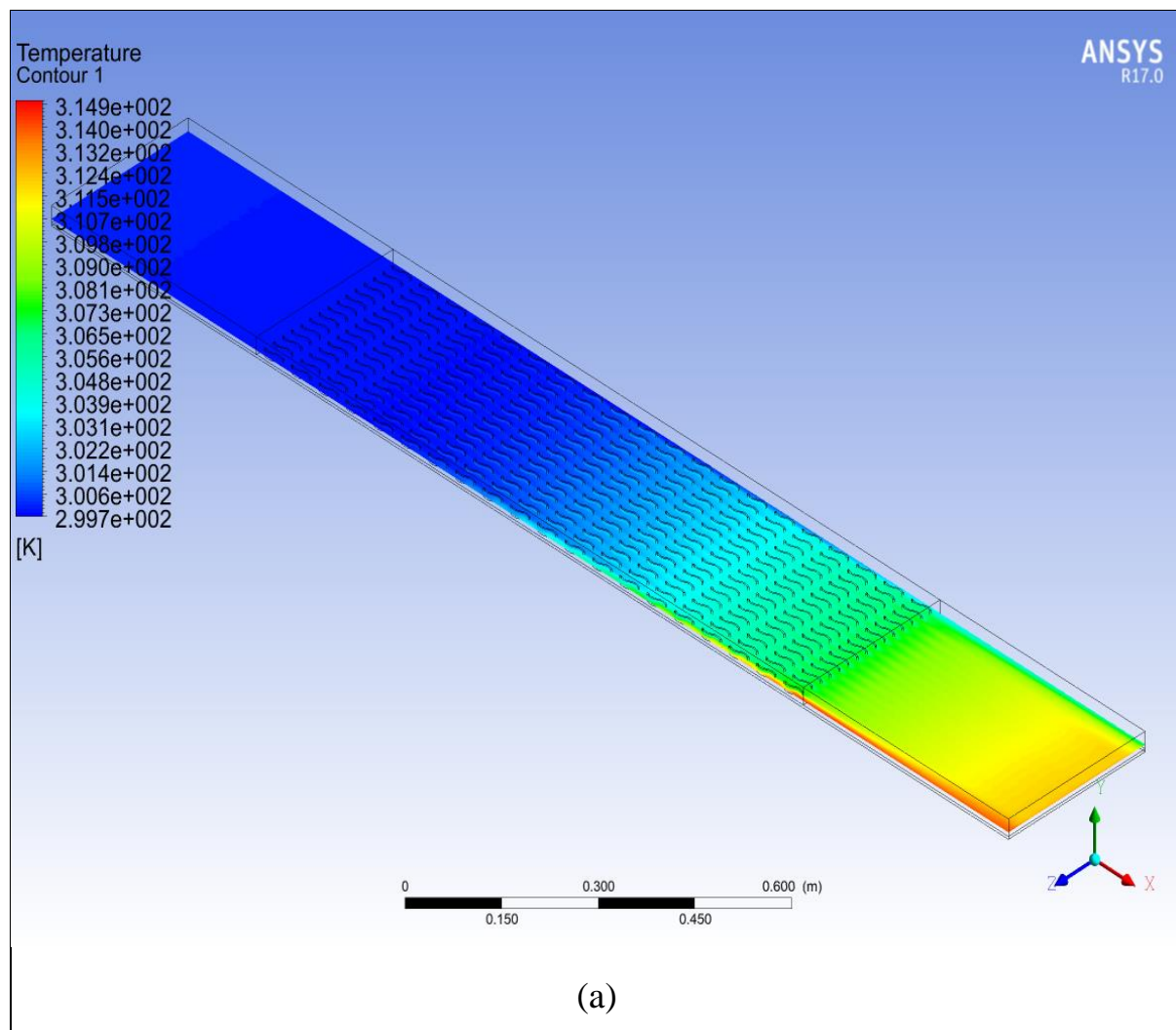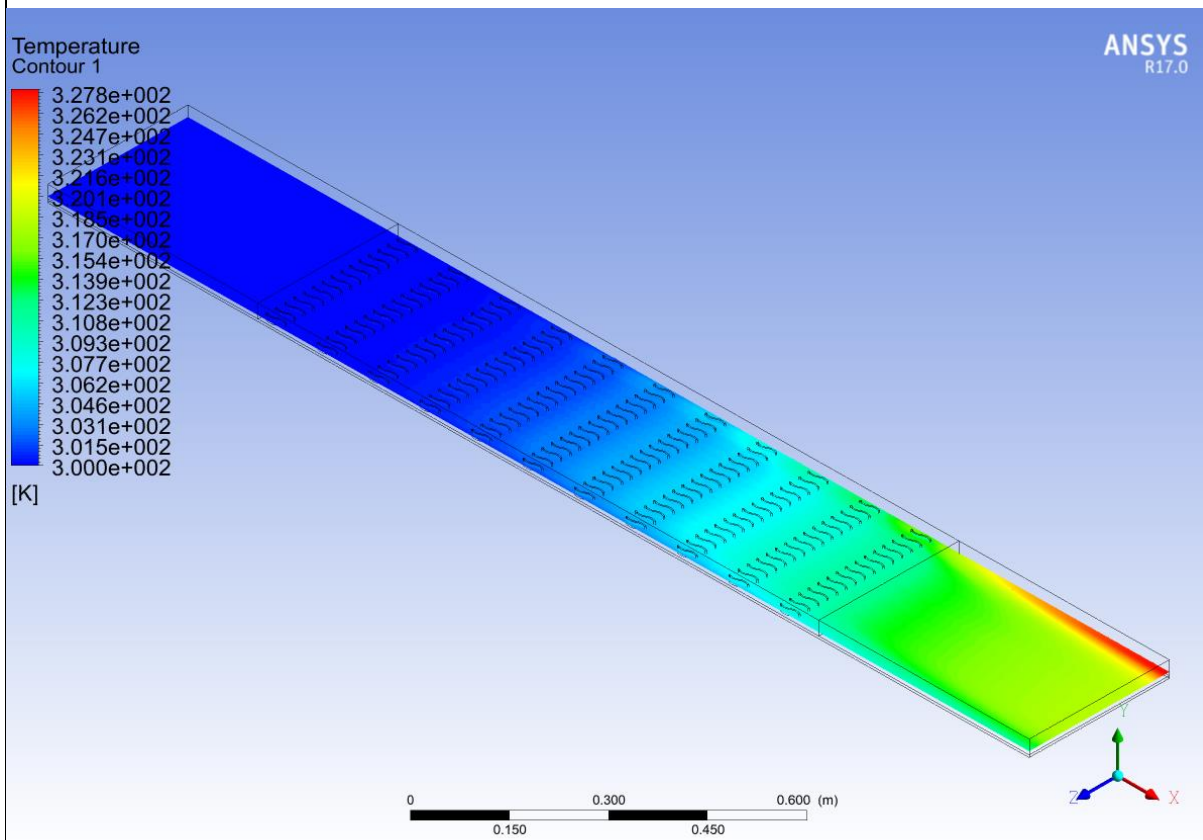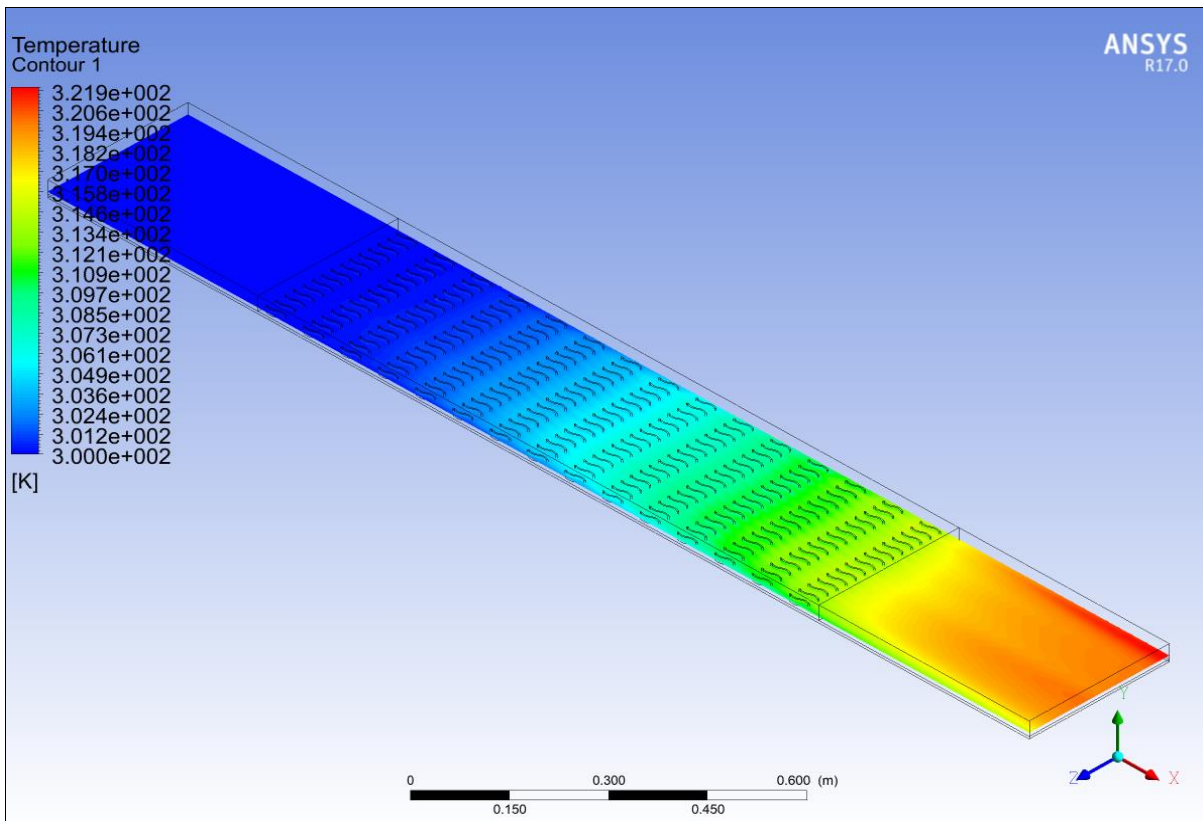
Figure (5-18): Temperature distributions contours for airflow along the SP-SAH for the S–shape inline at v=1.5 m/s at (a) p/H=1.667, (b) p/H=3.33, (c) p/H= 5, (d) p/H=6.66.

Figure (5-19) illustrates contour of the temperature distribution of the staggered S-shape arrangement with parameters of Reynolds number (5545), angle of attack of 60º, and l/H = 0.835–3.33, its shows that the temperature in S-shape is higher than the s-shape inline values because the fluid currents mix appropriately with respect to the staggered arrangement. Where it is noted in figures (a) and (b), the high-temperature distribution is due to the strong vortices formed due to geometric artificial roughness and thus an increase in the heat transfer rate.

(a)

(b)

(c)

(d)
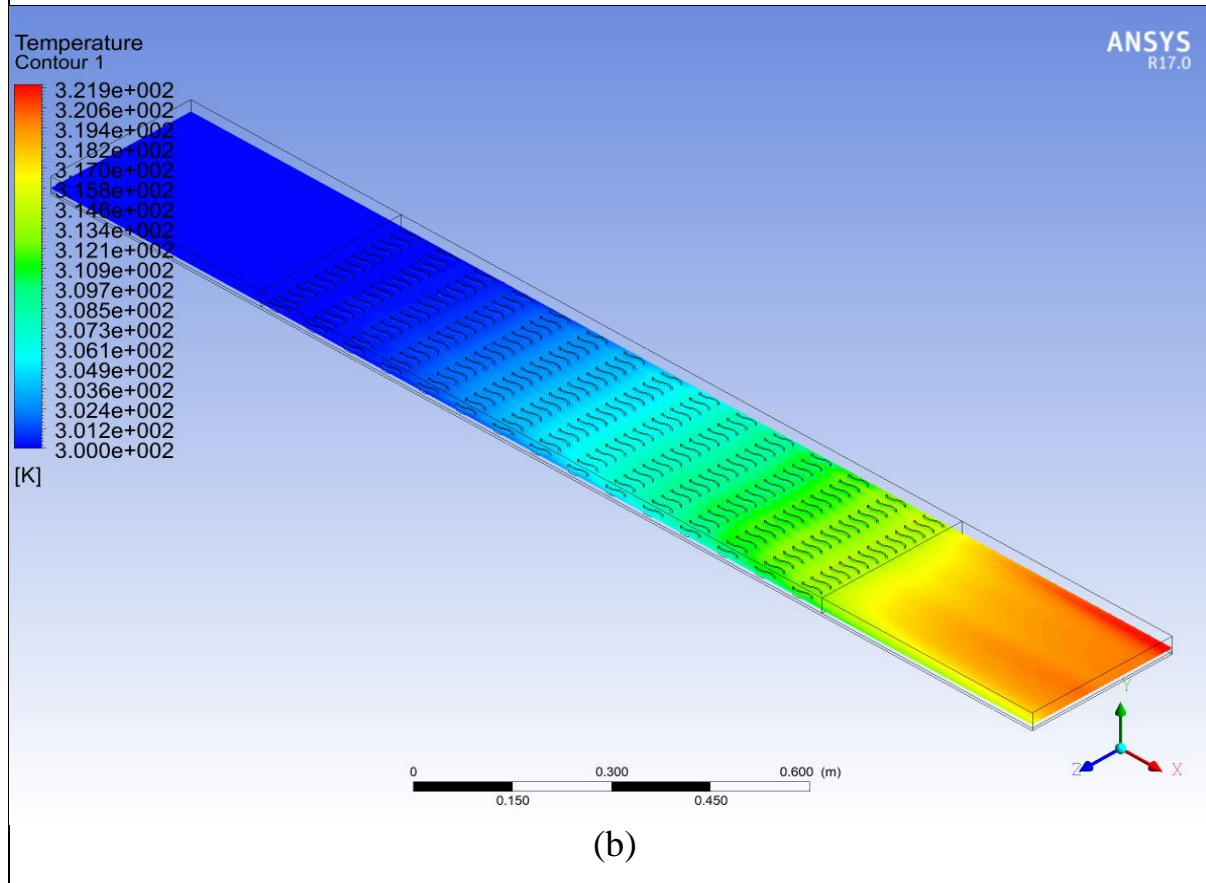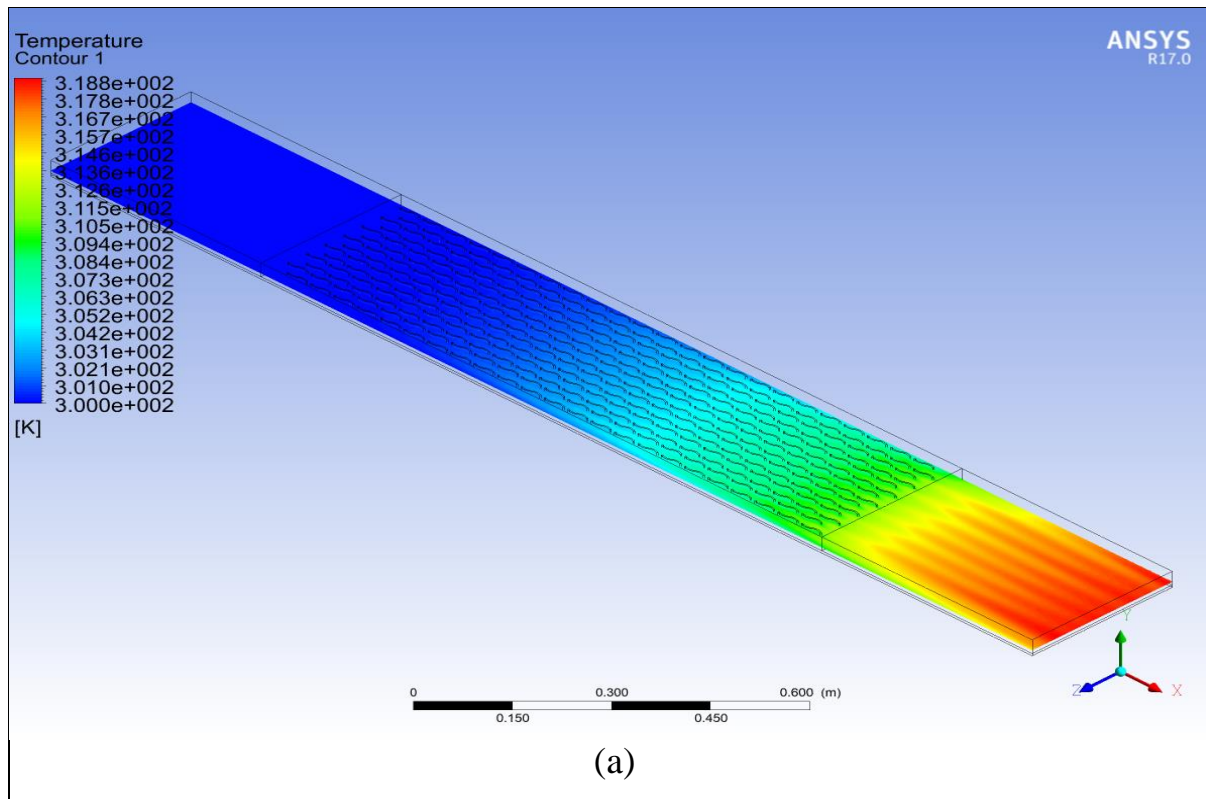
Figure (5-19): Temperature distributions for airflow along the SP-SAH for the S–shape inline at v=1.5 m/s at (a) l/H=0.835, (b) l/H=1.667, (c) l/H= 2.5, (d) l/H=3.33.

5.6.1 The effect of p/H on Nu and _f_ for S-shape

Figure (5-20) illustrates the diversity between the Nusselt number and p/H values at different arrangements. It shows an increase in the Nusselt number with increasing p/H until p/H=3.33 then decreases. It occurs because the SAH duct on absorber plate has lower artificial roughness at (p/H) higher relative roughness، this leads to the reconnection points are few، and the turbulent vortices that increase the Nusselt number will decrease with increasing pitch. Where observed at p/H=3.33, the values of Nu=192 and 181 for both S-shape staggered and inline, respectively.
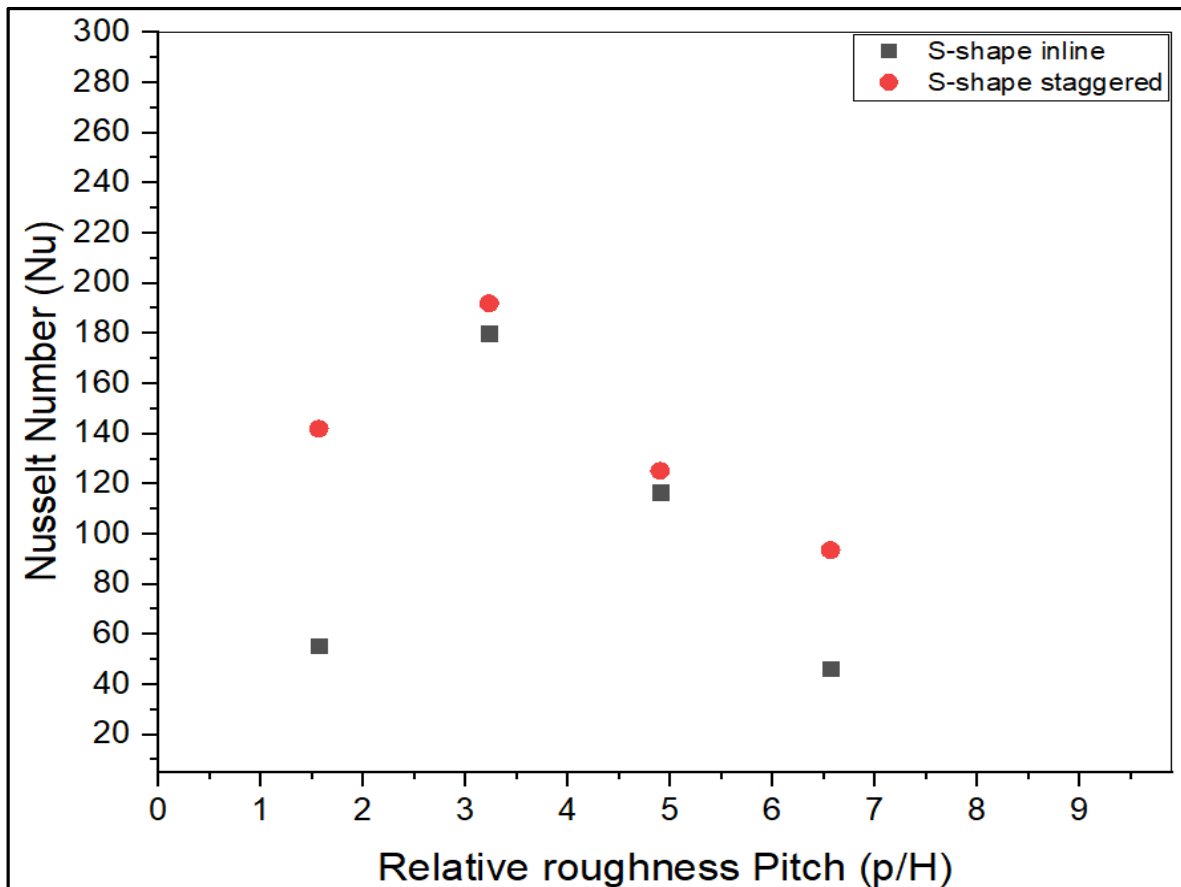
Figure (5-20): Variation of Nu with the p/H at l/H=1.667.

Figure (5-21) the effect of p/H on friction factor for S-shape at different arrangements. The figure shows that as the values of (p/H) increase towards the x-axis, the value of f decreases toward the y-axis. due to a decrease in the number of reattachment points. For S-shape staggered and inline arrangements.
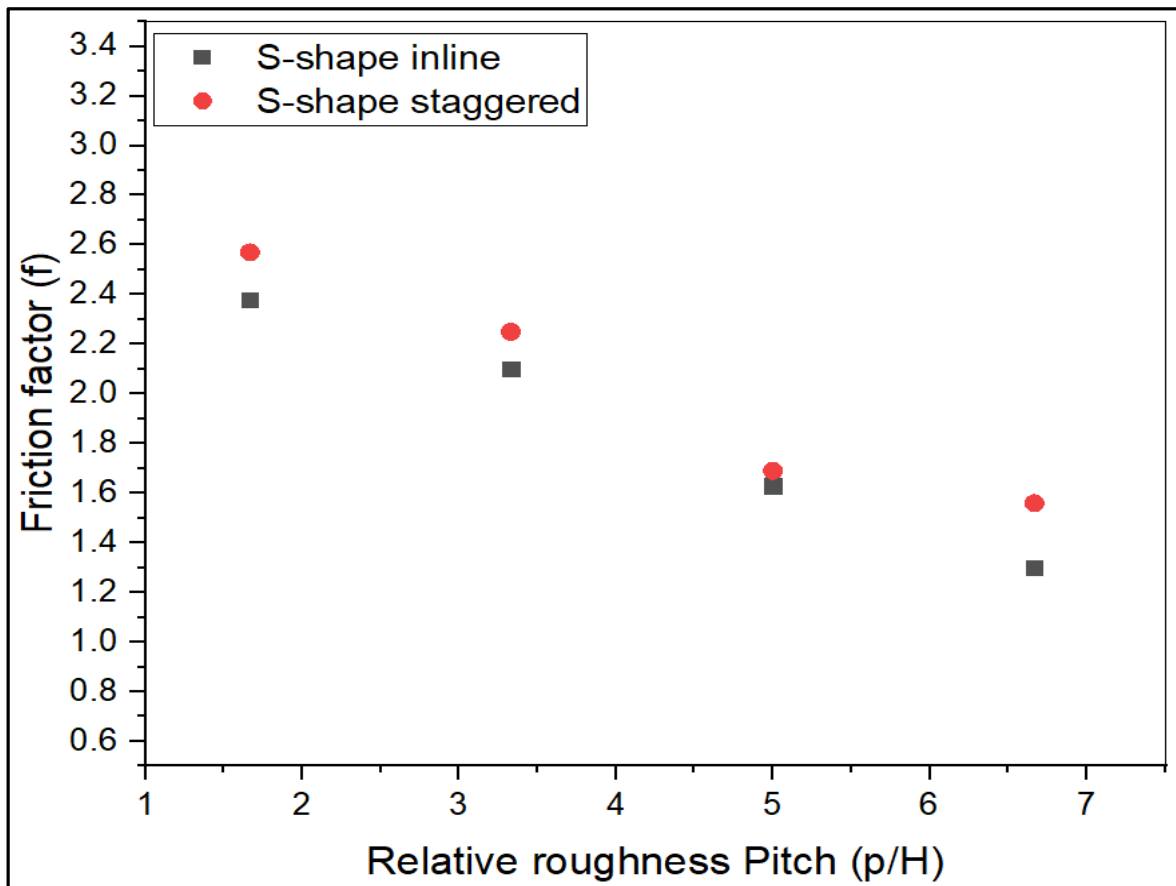
Figure (5-21): Variation of f with the p/H at l/H=1.667

5.6.2 The effect of p/H on Nu and *f* for arc-shape

The effect of the relative roughness step on the heat transfer rate is illustrated in Fig. (5-22) using the arc-shaped artificial roughness in an embedded arrangement. with a Reynolds number of 5545 and p/H = 1.667-6.667 parameters

The figure shows the increase in the heat transfer areas in the arc-shaped ribs with an inline arrangement at p/H = 3.33 in figure (b) and it is noted in figures (c & d) that there is a decrease in temperatures due to the increase in p/H. The reason is that the fluid flow with a sudden expansion leads to a separation zone at the rib downstream. The fluid getting back together in front of the next rib follows this separation. Since the step is getting bigger, the periodic rotation doesn't cause the flow to get back together, so it doesn't create a secondary vortex that speeds up the rate of heat transfer.
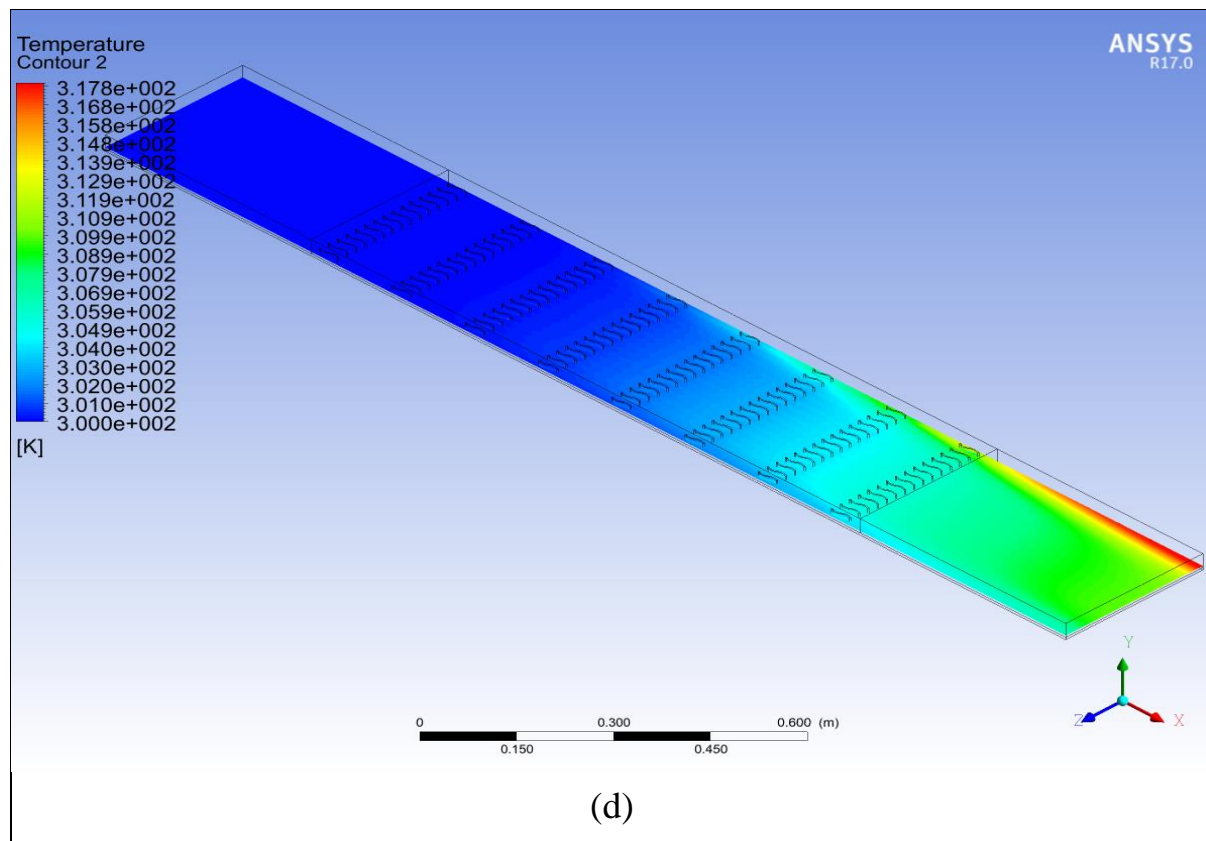

(a)

(b)

(c)

(d)
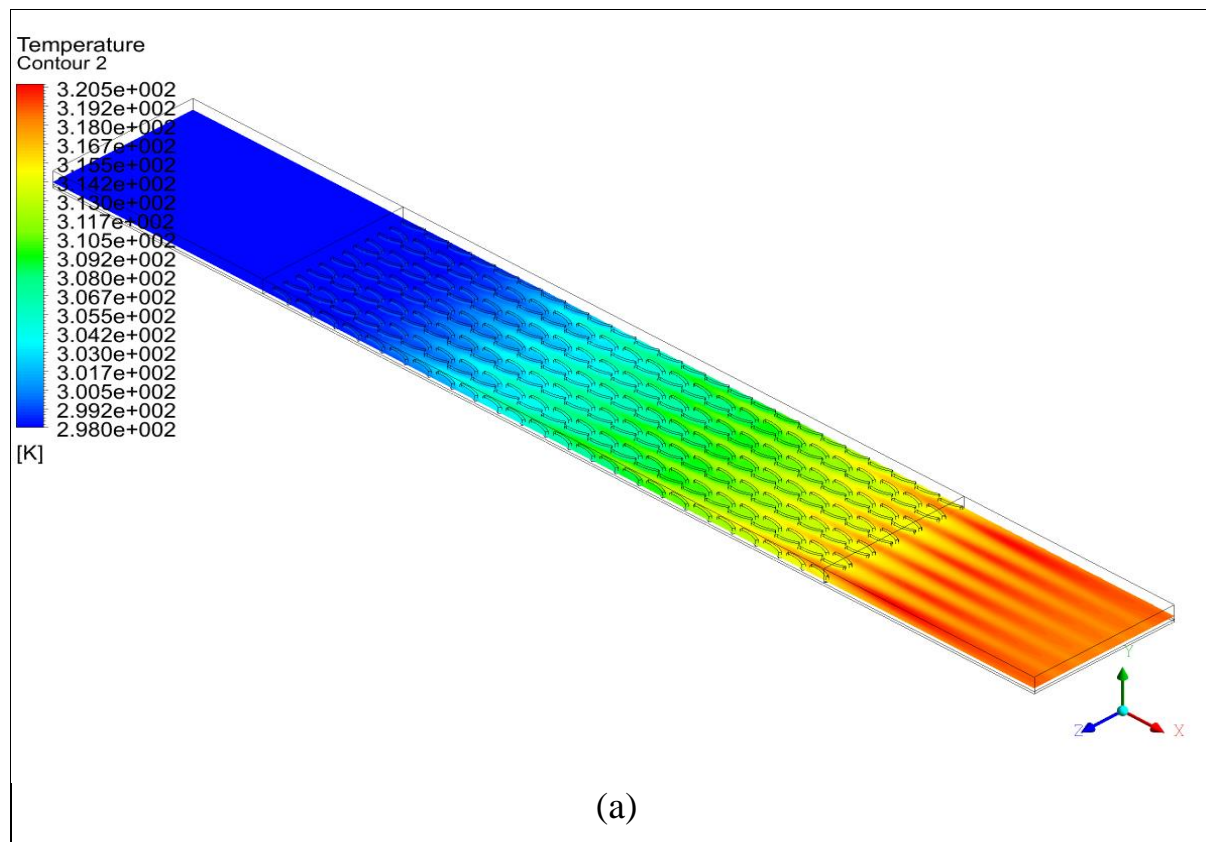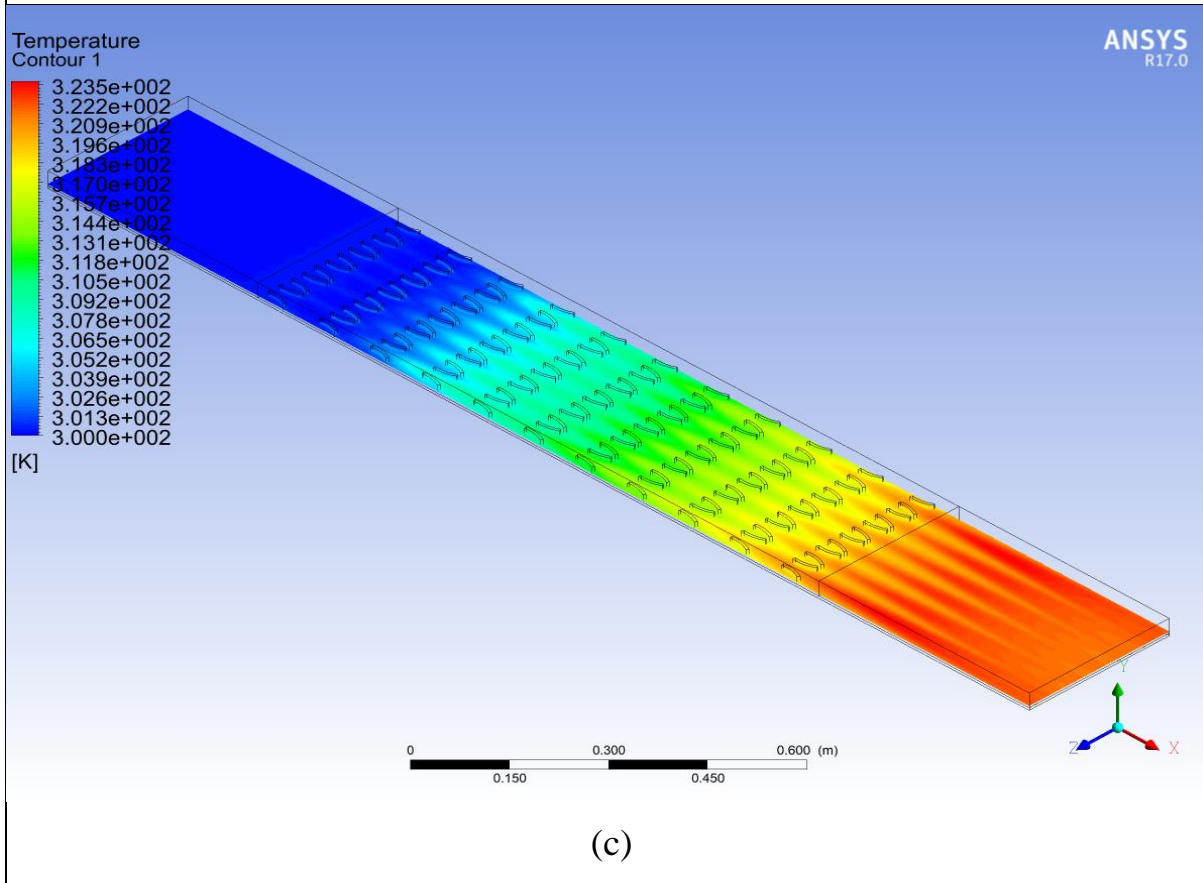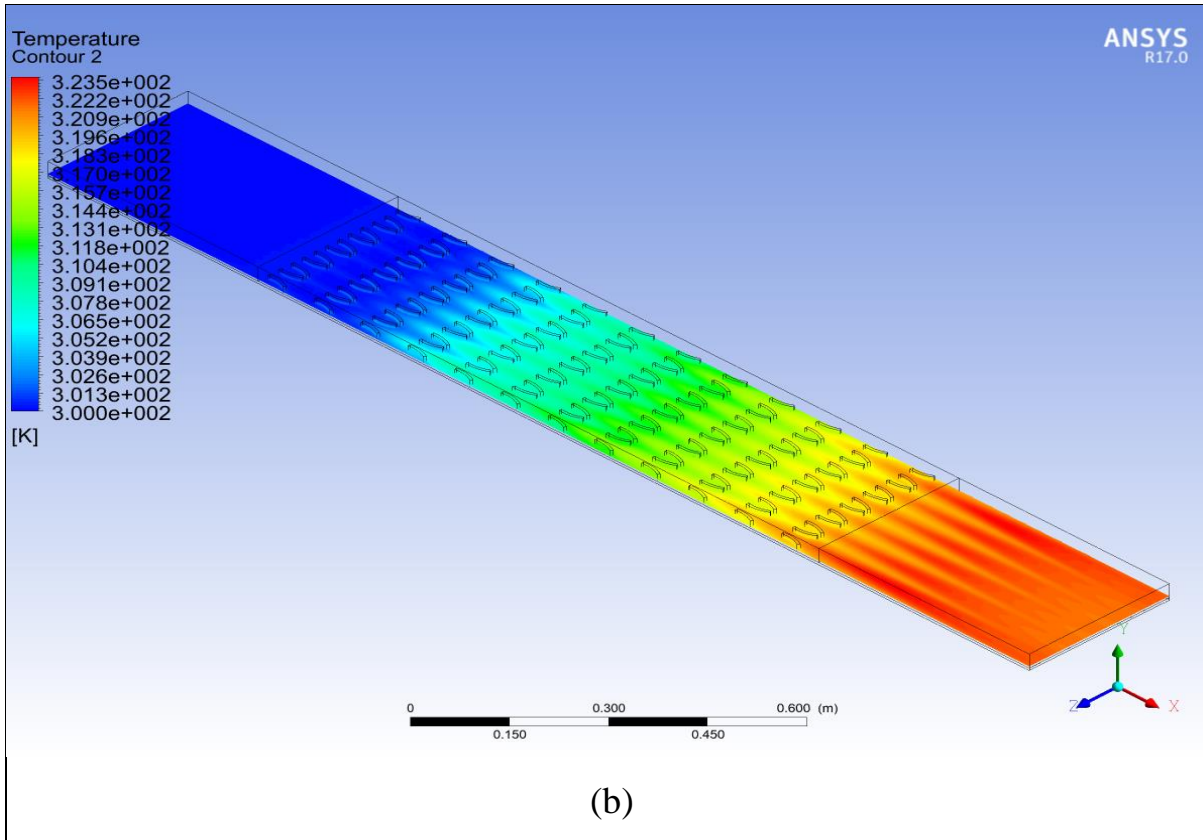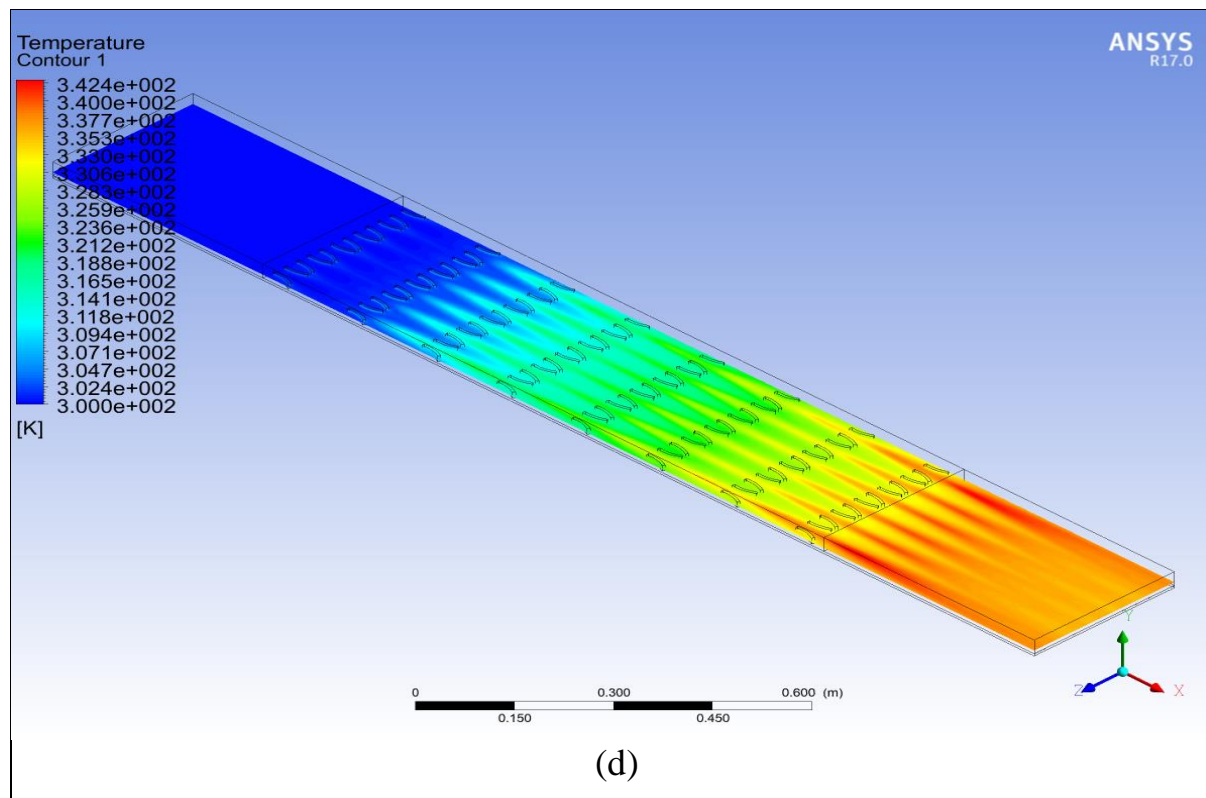
Figure (5-22): Temperature contours for airflow along the SP-SAH for the arc–
shape inline at v=1.5 m/s at (a) p/H=1.667, (b) p/H=3.33, (c) p/H= 5, (d)
p/H=6.667

In Figure (5-23), related to the arc-shaped roughness in staggered order, the effect of the relative roughness step on the heat transfer rate is illustrated using the parameters of the Re=5545 and l/H = 0.835–3.33. The figure shows the increase in the heat transfer areas in the arc-shaped ribs with an embedded arrangement at l/H = 1.667 in figure (b), where it is noticed in the figures that the staggered arrangement gives a better heat transfer rate. Although increasing the value of l/H decreases the heat transfer value, in figure (c & d), a decrease in temperature is due to the increase in l/H. The reason is that the fluid flow with a sudden expansion leads to a separation zone at the rib downstream. This separation is followed by the reconnection of the fluid in front of the next rib, and because of the increase in the step, the cyclic rotation does not lead to

reconnecting the flow and thus does not lead to the formation of a secondary vortex that contributes to an increase in the temperature.

(a)

(b)

(c)

(d)
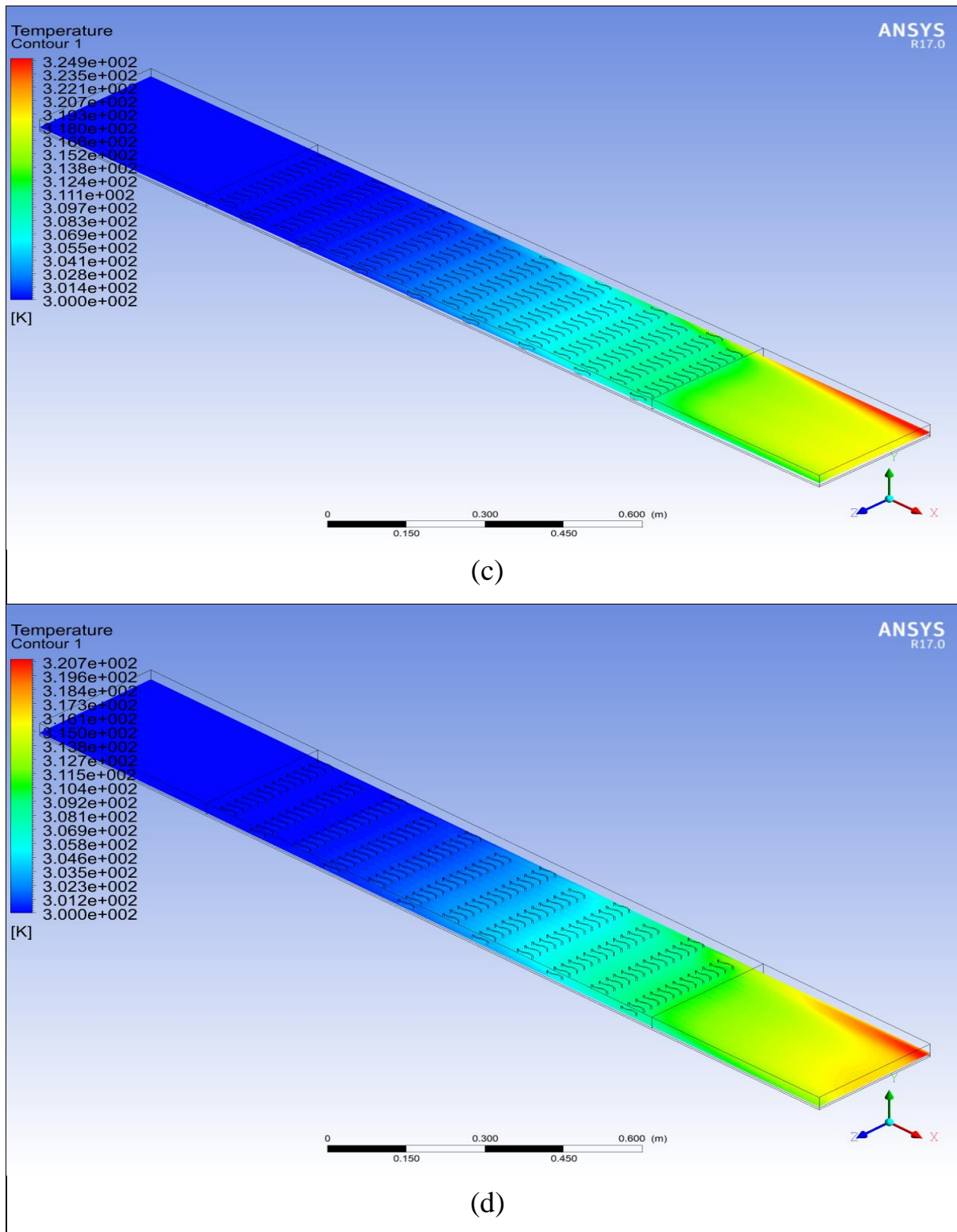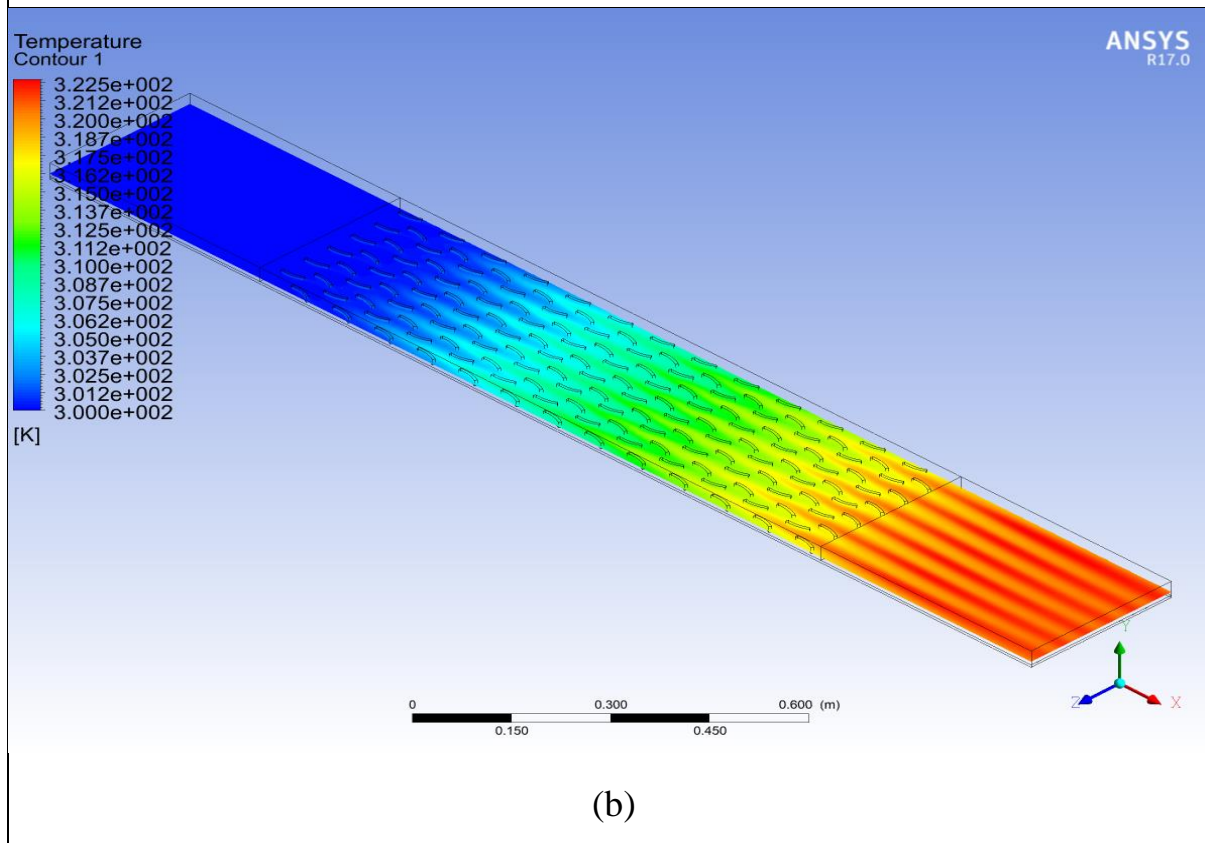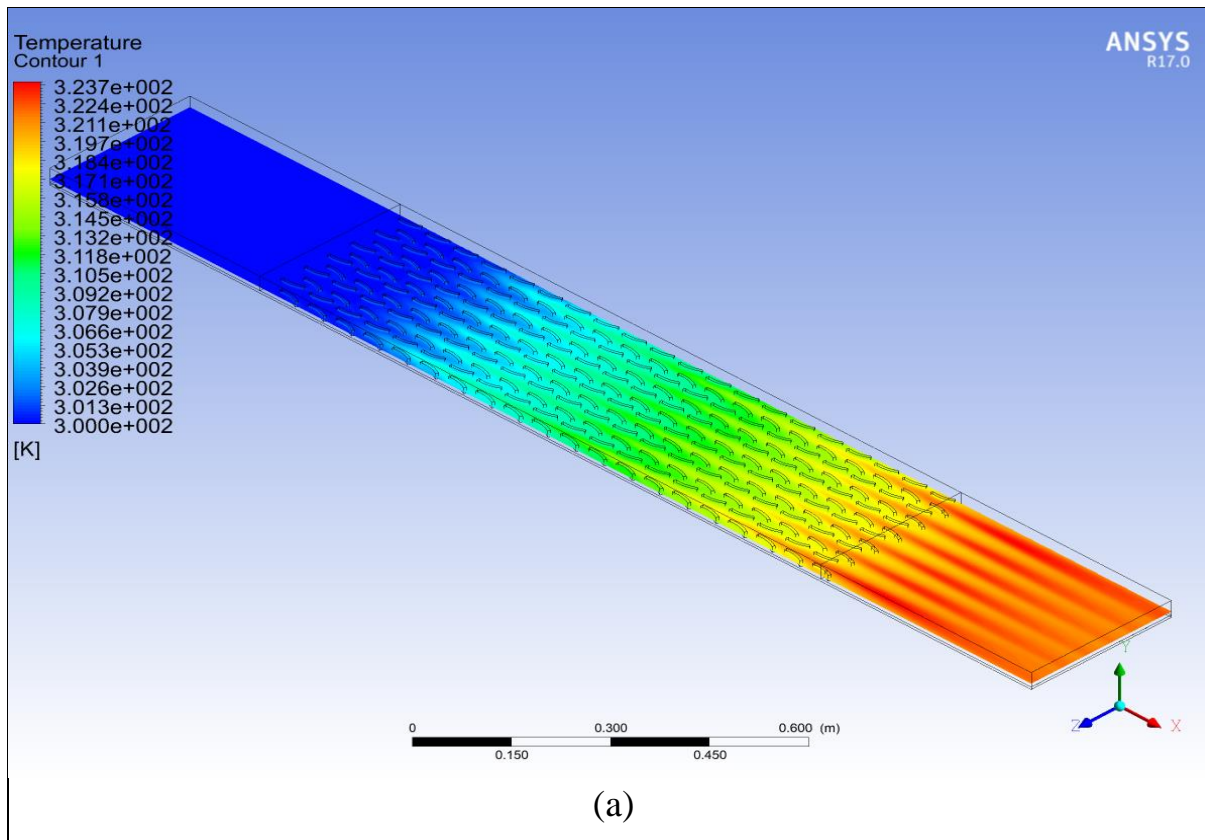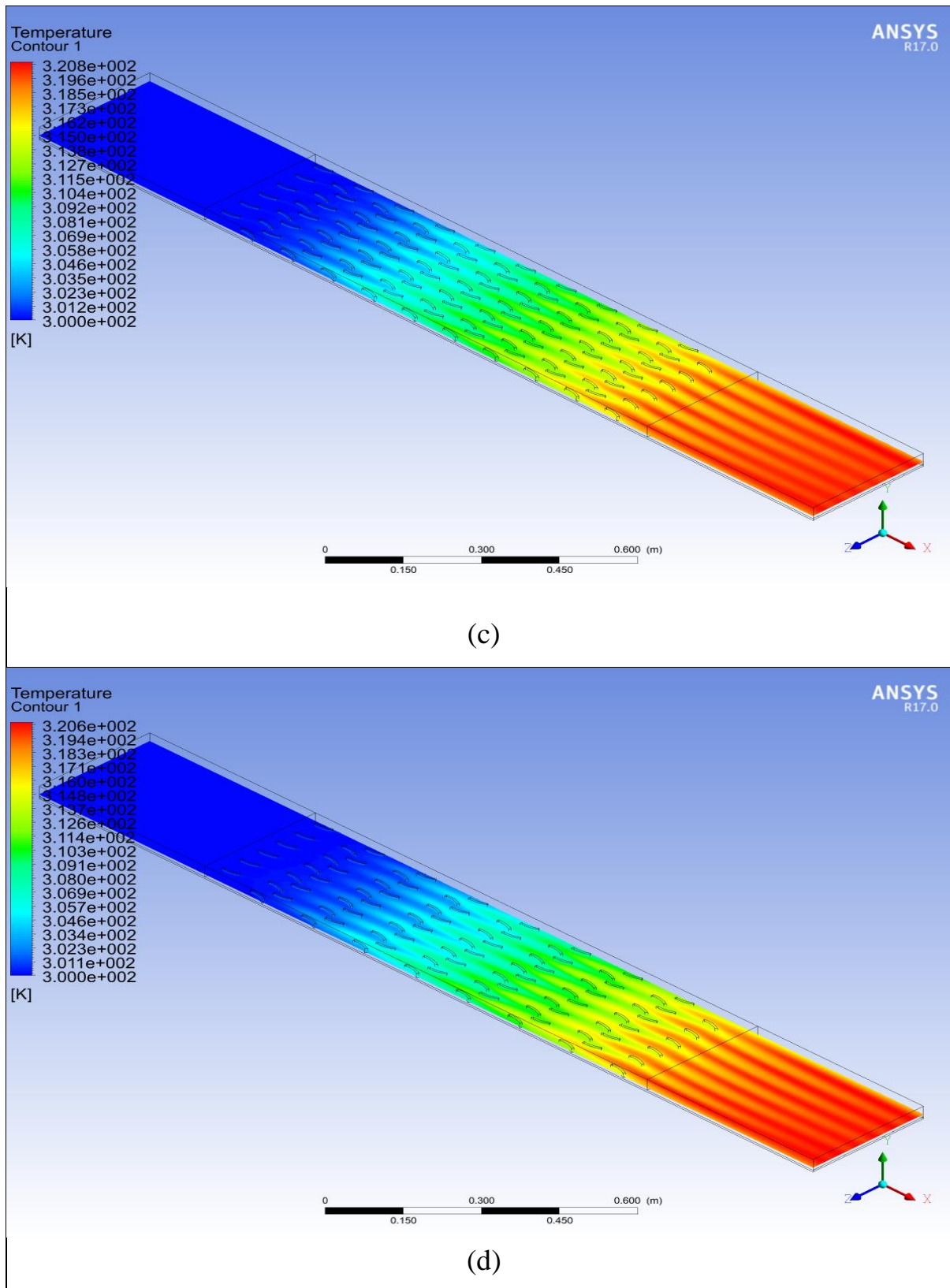
Figure (5-23): Temperature contour for airflow along the SP-SAH for the arc–

shape inline at v=1.5 m/s at (a) l/H=0.835, (b) l/H=1.667, (c) l/H= 2.5, (d)

l/H=3.33

In Figure (5-24), the contrast between the Nusselt number and p/H of the arc-shaped roughness shown in staggered and inline order. It also explains the further improvement of heat transfer with an constant in the Re=5545 in the direction of flow, since boundary layer cleavage results in additional recycling occurring near the wall region. In particular, the arc shape of the rib at p/H = 3.33 caused a larger heat transfer than the other p/Hs. This is because the fluid reconnects in front of the next rib, and because the step increases, the cyclic rotation does reconnect the flow, which leads to the formation of a secondary vortex that makes the Nusselt number go up.
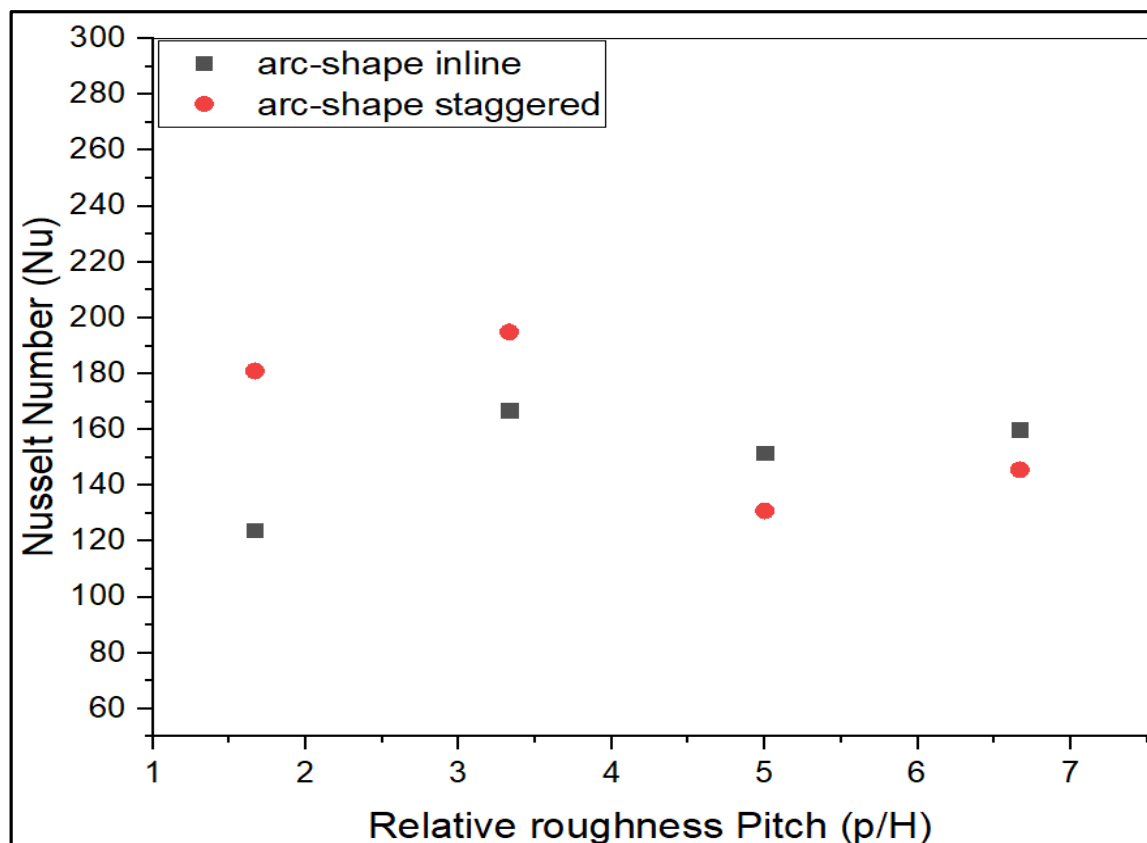
Figure (5-24): Variation of Nu with the p/H at l/H=1.667 at Re=5545

Figure (5-25) illustrates the changes in the friction factor related to the relative roughness step (p/H) for some specific values of Re at α= 60°. The results, therefore, expect the friction factor to reach a maximum at (p/H=1.667). This could be because there are many reinstallation points for the free shear layer between each pair of ribs, which causes strong disturbances at the reinstallation point to speed up the rate of heat transfer. It is noted from the figure that the friction factor decreases as the value of p/H and l/H constant. This happens because of the result obtained, which lowers the obstructions obtained and, consequently, the reconnection points are reduced.
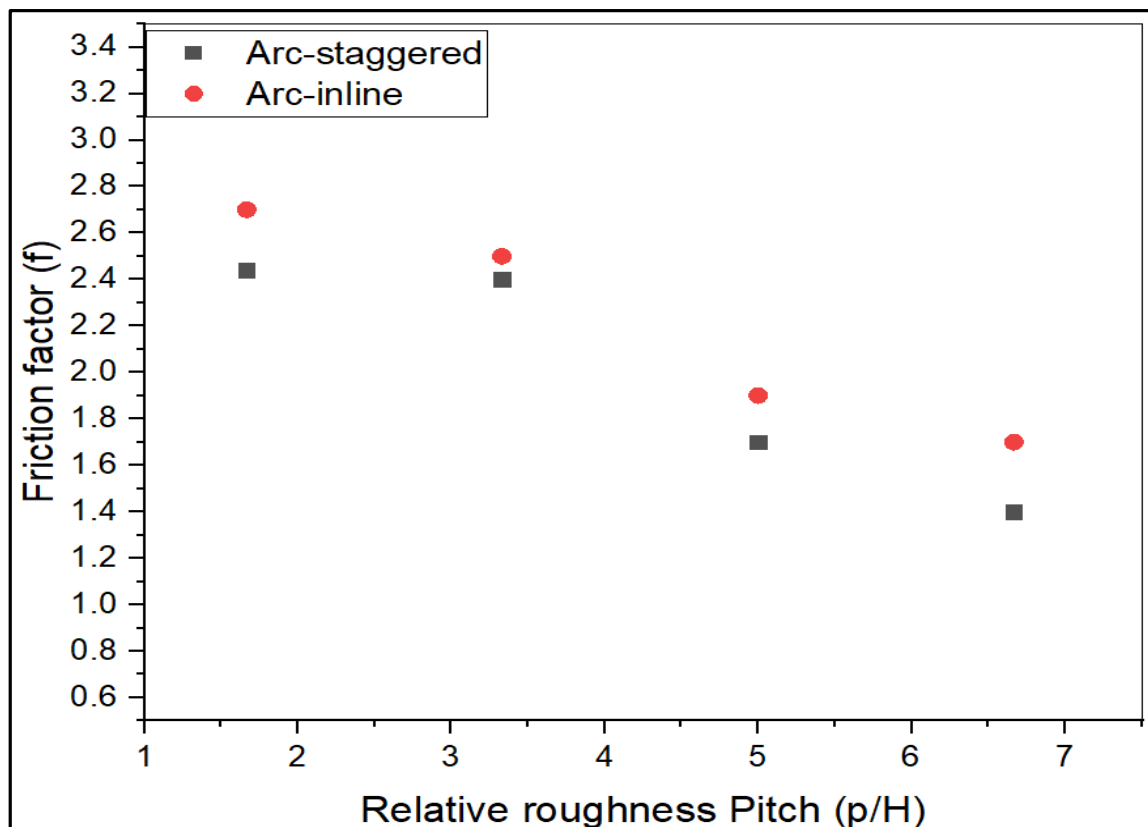
Figure (5-25): Variation of f with the p/H at l/H=1.667

5.7 Heat transfer characteristics

The thermal heat transfer of the proposed shapes was measured in a SAH S-shape and an arc shape with staggered and inline arrangements with a Nusselt number.

Figure (5-26) illustrates the diversity in Nu number to Re number values for inline S-type synthetic roughness for all p/H values. As it is clear that the values of Nu increase with the increase in the values of Re compared to the smooth plate, The figure shows that there is a sign improvement in the Nu for all cases of S-shaped artificial roughness arrangements. Increasing speed at a higher Re leads to an increase in heat transfer The higher values of Nu appear at p/H = 3.33 by 148. In addition, the rationale for this is because a rise in the Re increases the kinetic energy of the disturbance and the rate of disturbance dissipation, leading to an increase in the disturbance's intensity and, thus, an increase in the Nu. As the Re grows, indications of roughness begin to show outside the laminar sublayer because the thickness of the laminar sublayer decreases as Re increases. Additionally, the roughness assists to the evacuation of heat by creating vortices. Compared to a flat surface, this enhances the rate of heat transmission.
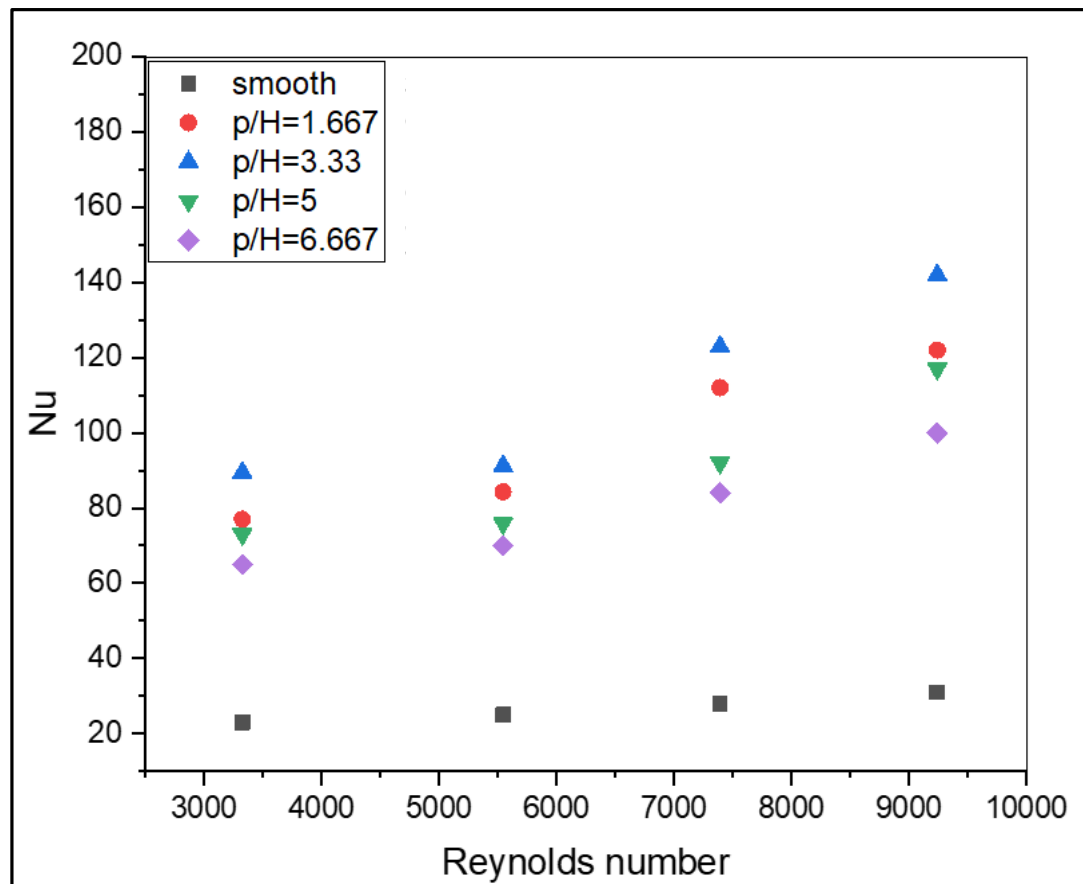
Figure (5-26): The relationship between the Nu and the Re for S-shape in line synthetic roughness.

Figure (5-27) the variance of Nu number to Re number values for S-staggered artificial roughness is shown for all l/H values. It is also evident that the Nu increases with the increase of the Re compared to the smooth plate, on all sides of the roughness due to the force of convection. In addition, the figure shows that there has been a big improvement in Nu number for all cases of S-shaped synthetic roughness arrangements. When the Reynolds number reaches 9241, the Nusselt number reaches its maximum value at l/H = 1.66 by (Nu = 162). A SAH with an S-shaped staggered arrangement shows an increase in Nusselt number values compared to smooth ducts. This can be explained because a higher Reynolds number increases the level of turbulence, and the presence of roughness contributes to heat displacement due to the generated vortices, which enhance the rate of heat diffusion.
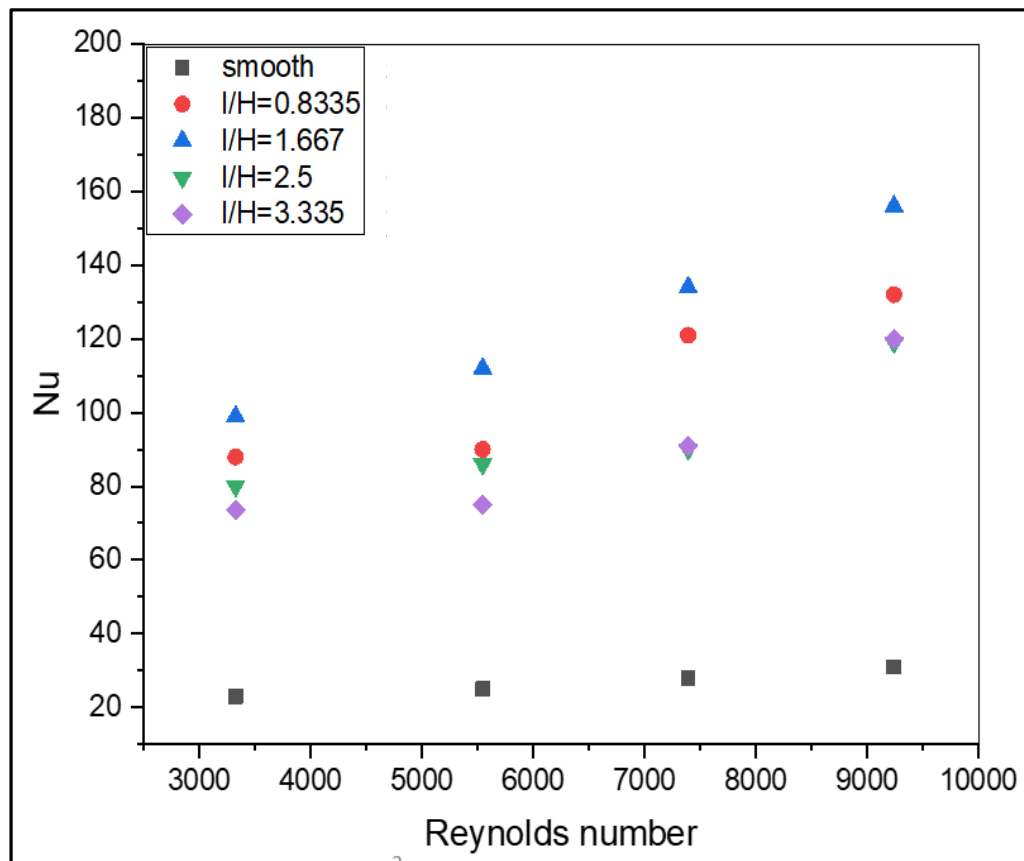
Figure (5-27): Nusselt number with respect to variation Re for S-shape staggered with different l/H.

Figure (5–28) shows the difference in the ratio of the Nusselt number to the Reynolds number, using an arc-shaped artificial roughness in an inline and overlapping arrangement. In Figure (a), the results of the roughness are shown in the included order, where it is noticed that with an increase in Re, there is an increase in the value of the Nu at p/H = 3.33, with a value of 4.67. The intensity of turbulence increases with higher air velocity, resulting in thinner thermal boundary layers and higher heat transfer coefficients. With an increase in Re, fluid exchange between the two sides of the S-shape with staggered arrangement increases. It can be seen that in this case, in figure (b), which presents extreme values for the Nu than in the cases for the rest of the l/H parameters, it provides the best thermal performance for the Re. The maximum Nu ratio of 4.879 for this case is found in the Re of 9324.
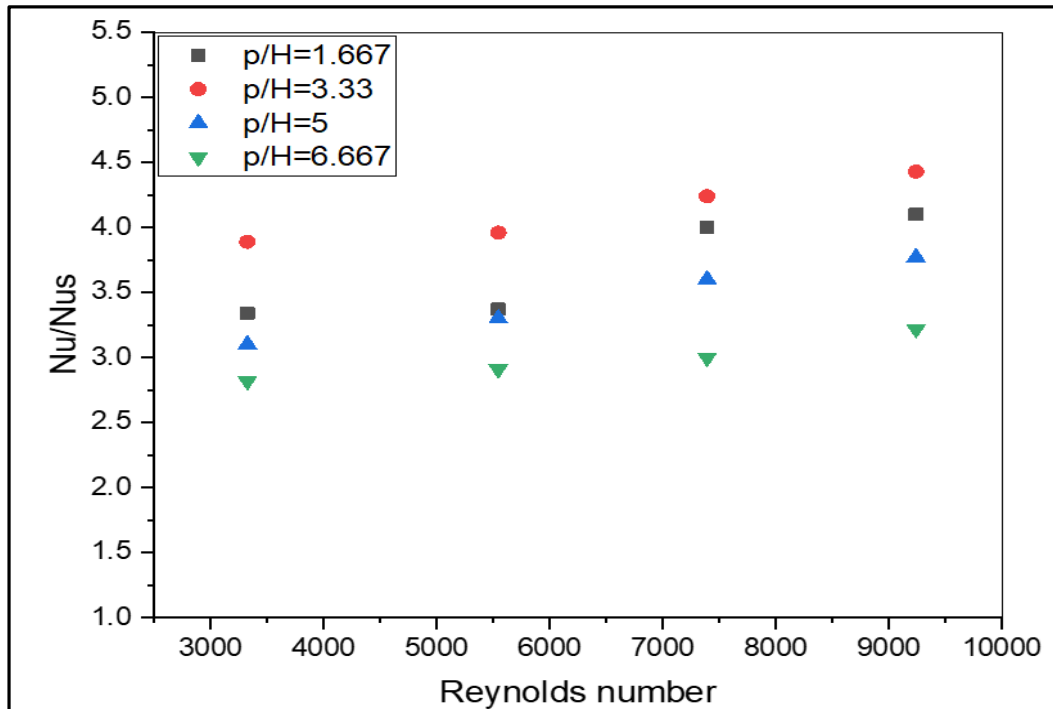
(a)
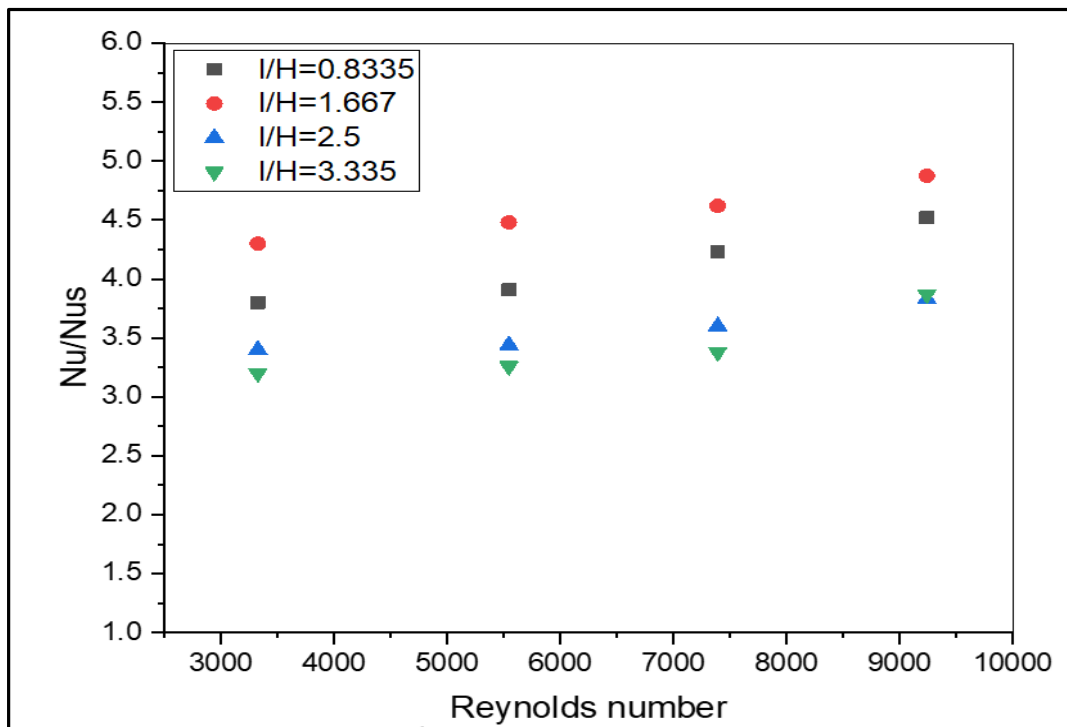
(b)

Figure (5-28): S-shape Nusselt ratio (a) Influence of p/H on Nu ratio (b) Influence of l/H on Nu ratio

The variance in Nu obtained under a perturbed system with Re is shown in Fig. (5-29), in the figure showing a change in Nusselt number with Re at the given

101

values of relative roughness of pitch. The figure shows that arc-shaped with inline arrangement results in significant improvement of heat transfer with similar direction compared to smooth channel and Nu increases with an increase of Re. At p/H = 3.33, it clearly shows an increase in heat transfer. For an arc shape with an inline arrangement at p/H=3.33, the Nu values for the inline are 186 over the smooth channel. This is due to the inline arrangement, which causes flow rotation and separation, resulting in a greater rise in flow turbulence intensity.
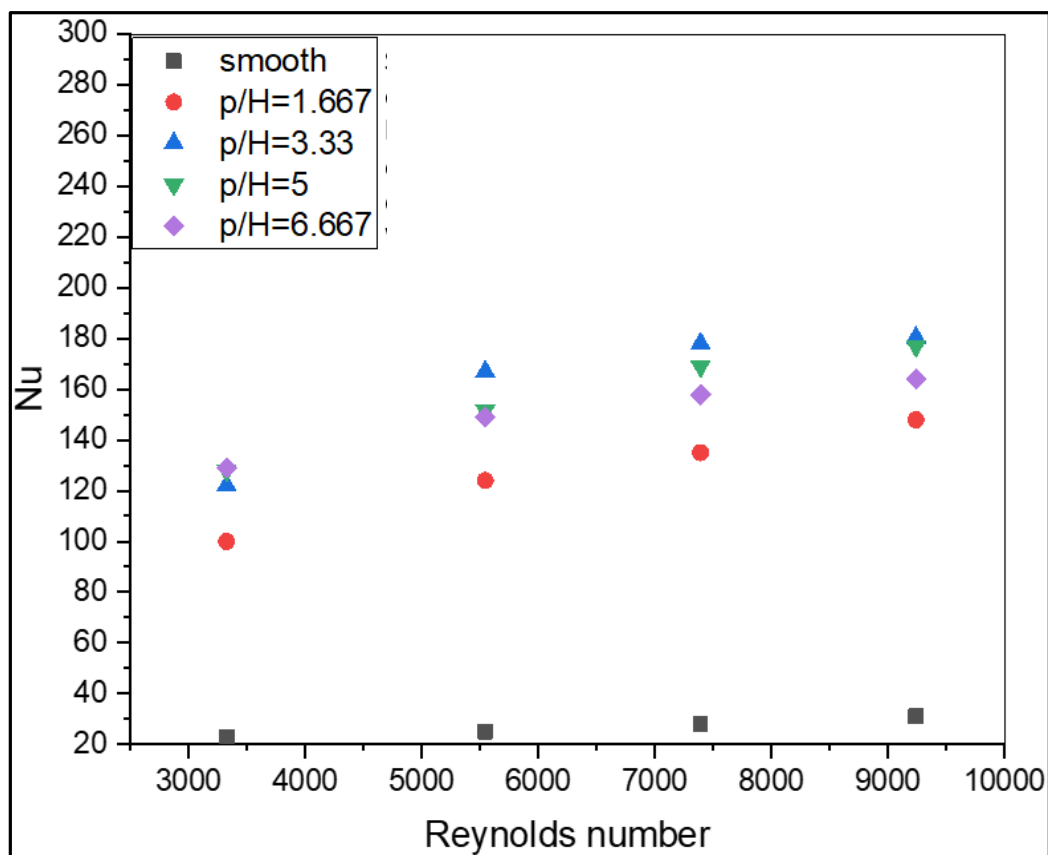
Figure (5-29): Nu with respect to variation Re for arc-shape inline

Figure (5-30) shows the relationship between the Nusselt number and the Reynolds number for the roughness in an arc in an staggered pattern, and it can be seen that the Nu increases with the rise of Re in all conditions. The heat transfer rate increases with the rise in the Re due to the thickness of the sub-layer decreases. The graph indicates that the Nu per l/H is greater than the Nu of a smooth channel. Nusselt number at l/H = 1.667, which is the best improvement of Nu = 219.
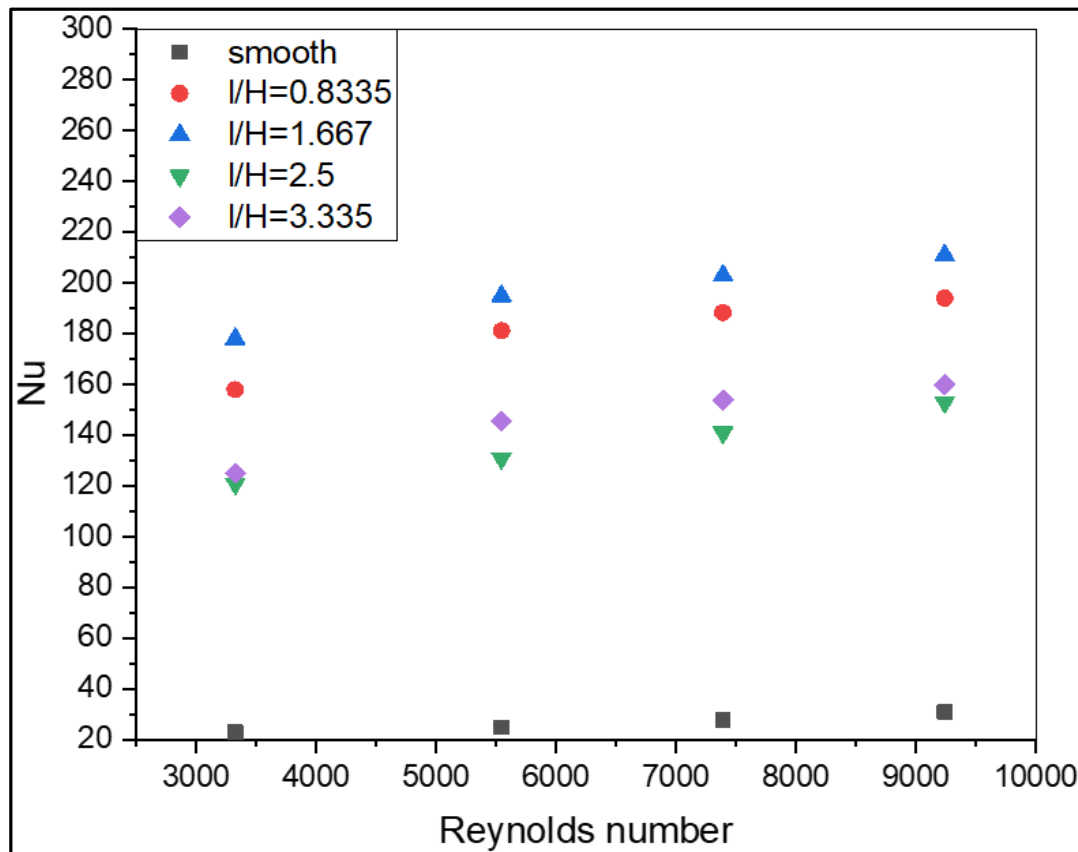
Figure (5-30): Nusselt number with respect to variation Re for arc-shape
staggered

The Nusselt number ratio is defined as the ratio of the Nu increase of the roughness to the Nus of the smooth channel, plotted against Re, in Figures (5-31a and b), respectively. In Figure (a), it is shown that in all cases Nu/Nus tends to increase slightly with the increase of Re. It is noted from the figures that the Nu/Nus of the staggered arrangement is higher than that of the inline arc shape shown in figure (b), and this can be attributed to the blockage of the higher flow and the stronger eddy/vortex flow than the staggered arrangement. Which leads to better fluid mixing between the flows Core and flows close to the wall. Moreover, closer examination reveals that the gradient heat transfer increase at l/H = 1.667 is higher than that at l/H = 0.835, 2.5 and 3.33. Where similar trends are observed for inline use at p/H = 3.33. For the arc shape having l/H = 1.667 and p/H = 3.33, the increments in Nu/Nus for circulating and inline are about 7.4–7.9 and 5.3–6.8, respectively.
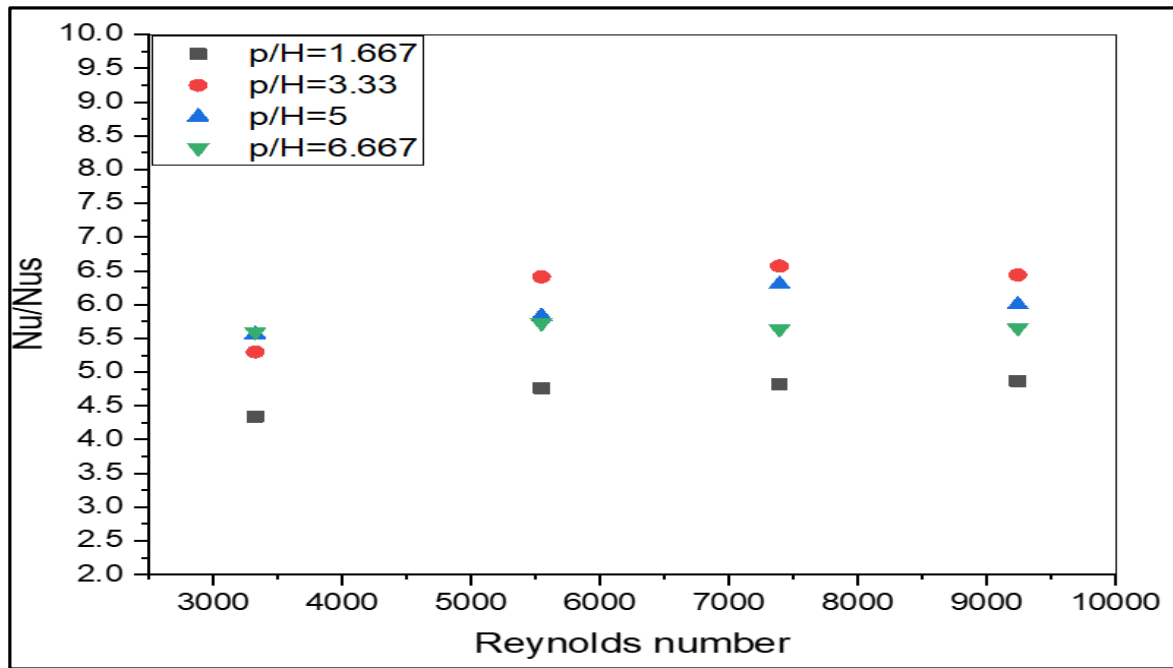
(a)
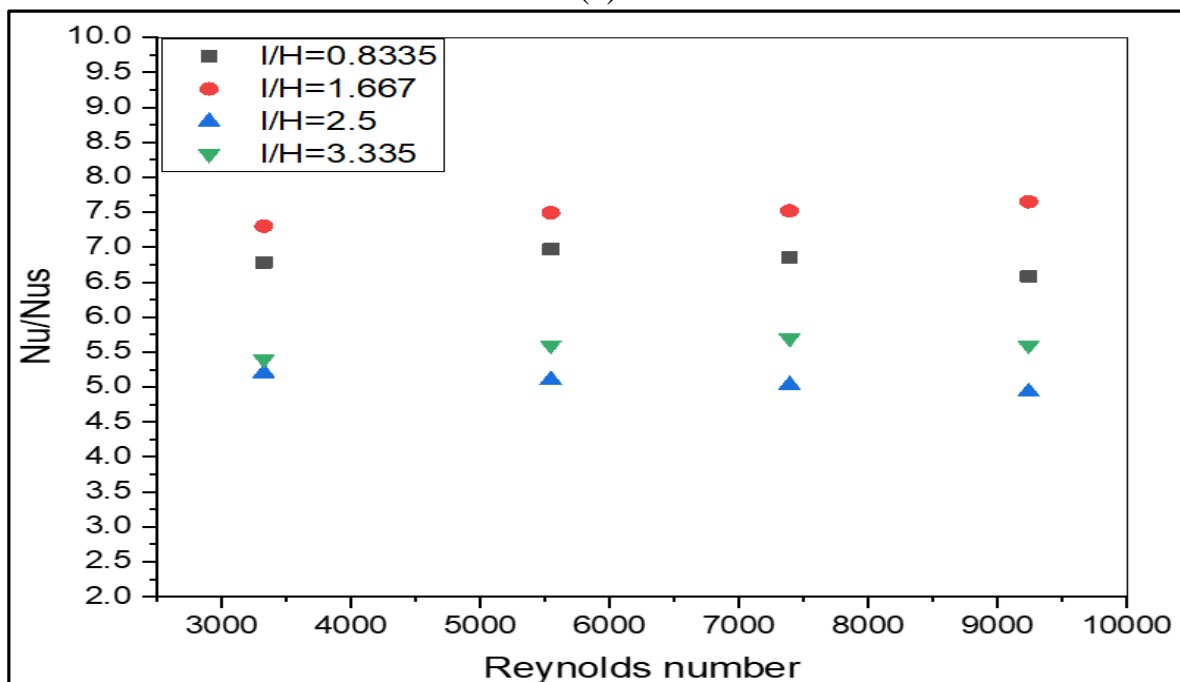
(b)

Figure (5-31): Arc shape Nusselt ratio (a) Effect of l/H on Nu ratio. (b) Effect of

p/H on Nu ratio.

5.8 Friction factor characteristic

The factor of friction (f) represents the influence of two types of artificial

roughness on the pressure drop (Δp) across an absorber plate of a SAH with (S-

shape and arc-shape) with arrangements staggered and inline was represented and a comparison with the smooth surface was made.

Figure (5-32) illustrated the variance of the friction factor to Reynolds number, for different (p/H) and fixed value of angle of attack 60° for S-shaped inline arrangements. It can be seen that the f reduction with an increases Re. The deposition of vortices from the S-shaped artificial roughness top results in extra energy loss, which raises the f. It is also observed that the f reduction with increases Re due to the suppression of the viscous sublayer. When the air enters the rough region of the SAH duct, it begins to accelerate, causing the pressure drop to rise. The pressure drop is more profound for the higher value of the Re. At p/H of 1.667, the maximum value of f is observed.
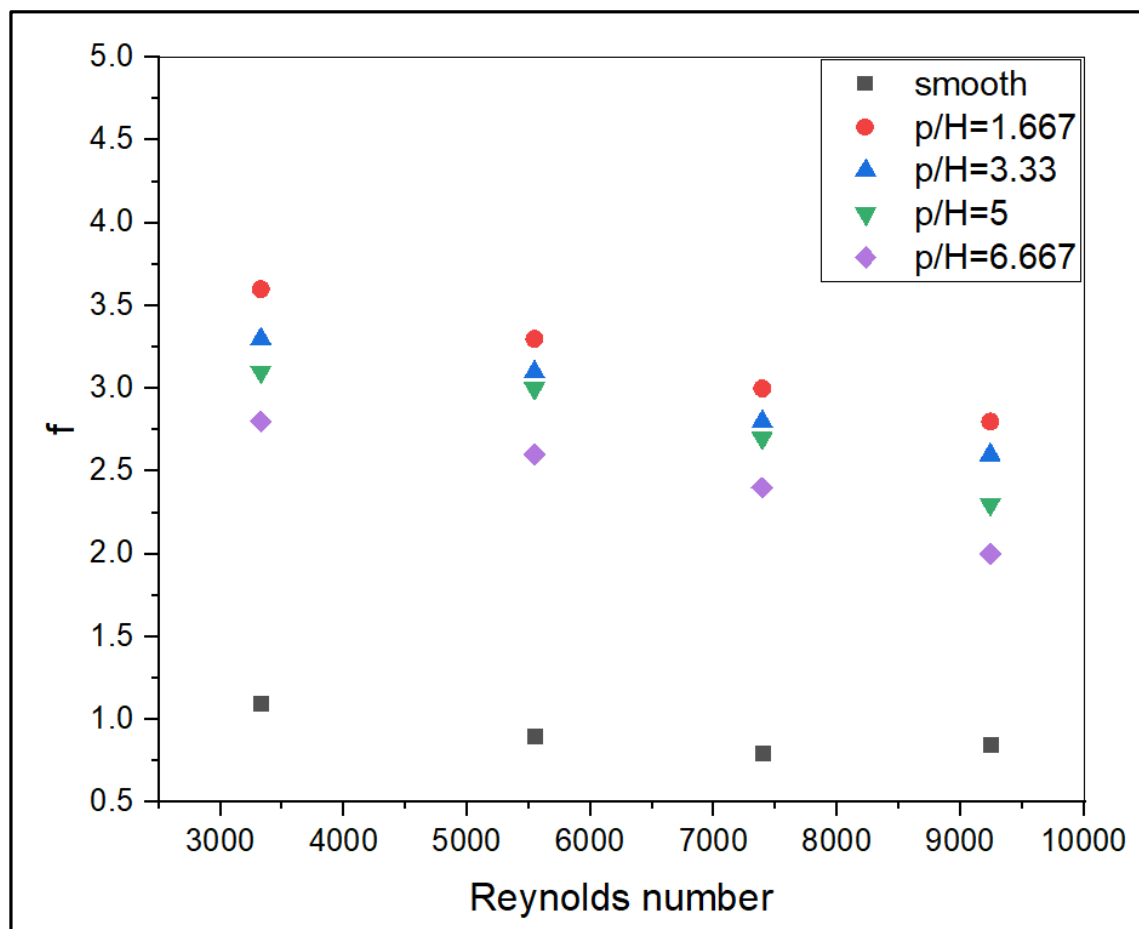
Figure (5-32): f with respect to variation Re for S-shape inline arrangement.

Figure (5-33) show that the f variance to the Re for the S-shape staggered arrangement synthetic roughness for all l/H values. For fixed value of (e/H= 0.271), the angle of attack is 60°. It can be seen that the f decreases with an increasing Re. The shedding of the vortices originating from the top of the circular cut rib causes additional energy loss, which leads to an increase in the f. It is also observed that the f decreases with the increase of the Re due to the fracture of the viscous sub-layer. For fixed value of (e/H), the values of the f decrease as (l/H) increases. It occurs because the SAH duct has lower (l/H) which results in lower flow resistance in the duct.
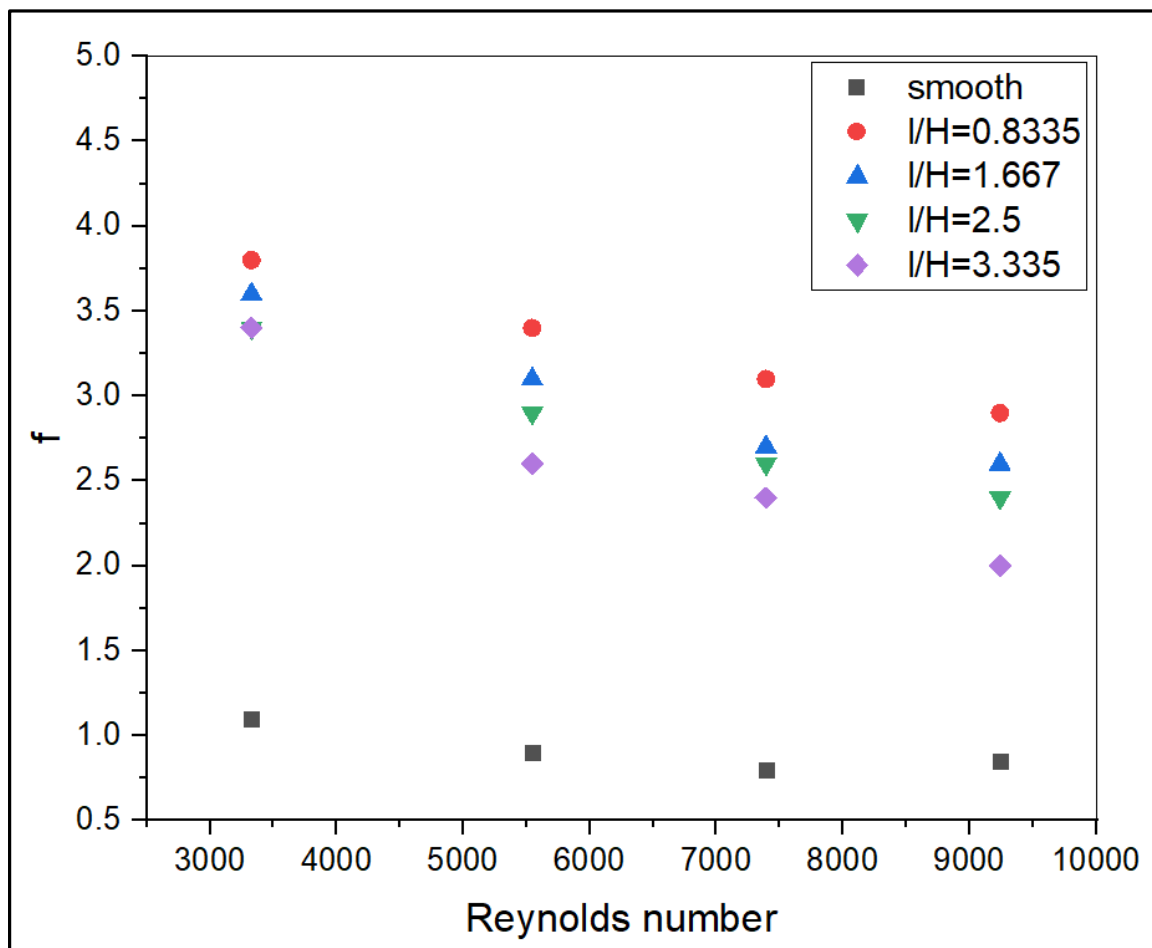
Figure (5-33): f with respect to variation Re for S-shape staggered arrangement.

Figure (5-34 a & b) shows the variance of the friction factor ratio (f / f s) to the Re for different (p/H) and for a constant (e/H) value of 0.271. It shown that the mean ratio of friction factor increases with a decreasing of (p/H) for all cases. It is also observed that the (f / f s) decreases with increasing Re for the range of parameters examined. The reinforcement in the (f / f s) was found to be 3.6 times that of the smooth channel, corresponding to p/H = 1.667, as shown in figure (a). For figure (b), it was found that the maximum enhancement in the average f was 3.7 times that of the smooth channel, corresponding to the l/H = 0.8335 at Re= 3327 for the parameter set examined.

Figure (5-35) illustrates the variance of the f to the Re. The average f decreases with an increase in Re. The figure also depicts the effects of p/H on f, for fixed angle of attack 60° for arc-shaped inline arrangements. Furthermore, higher p/H cause a decrease in the f at the farthest Re of 9241. According to the plotted values, it found the maximum f at p/H=1.667 of value 3.9. It is accepted that f decreases with an increase in Re due to the suppression of the viscous sub-layer for a fully developed turbulent flow.
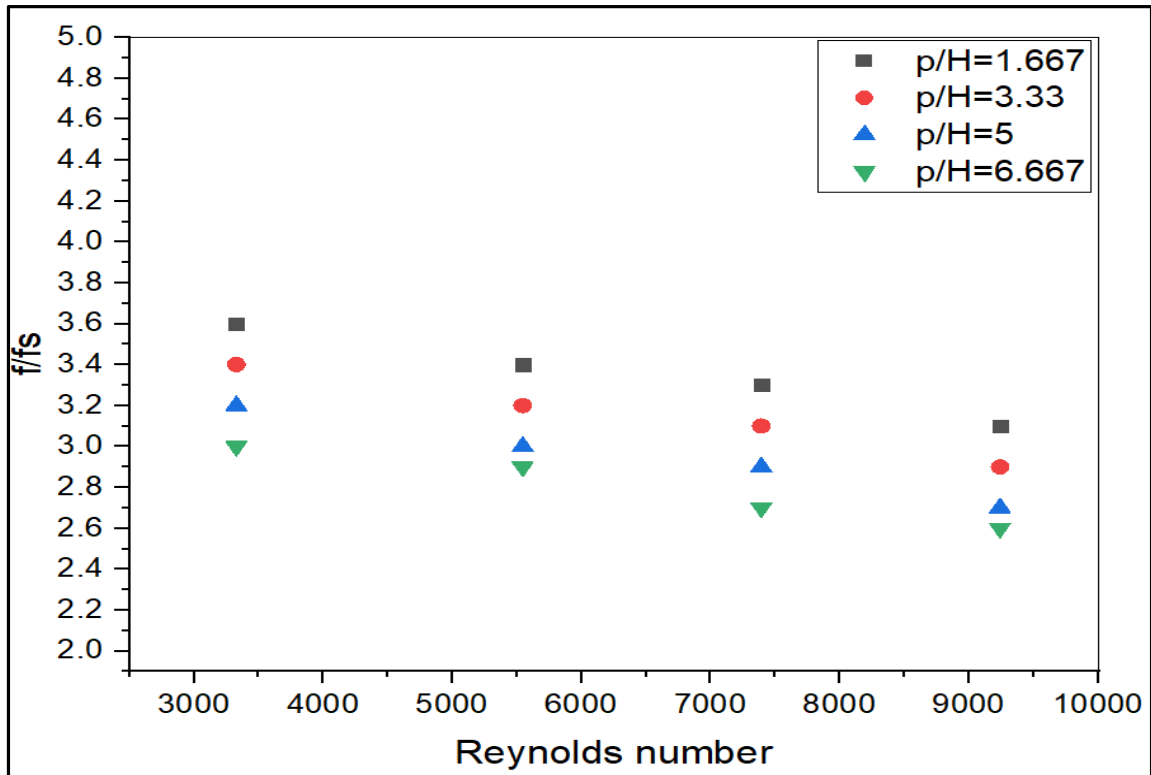
(a)
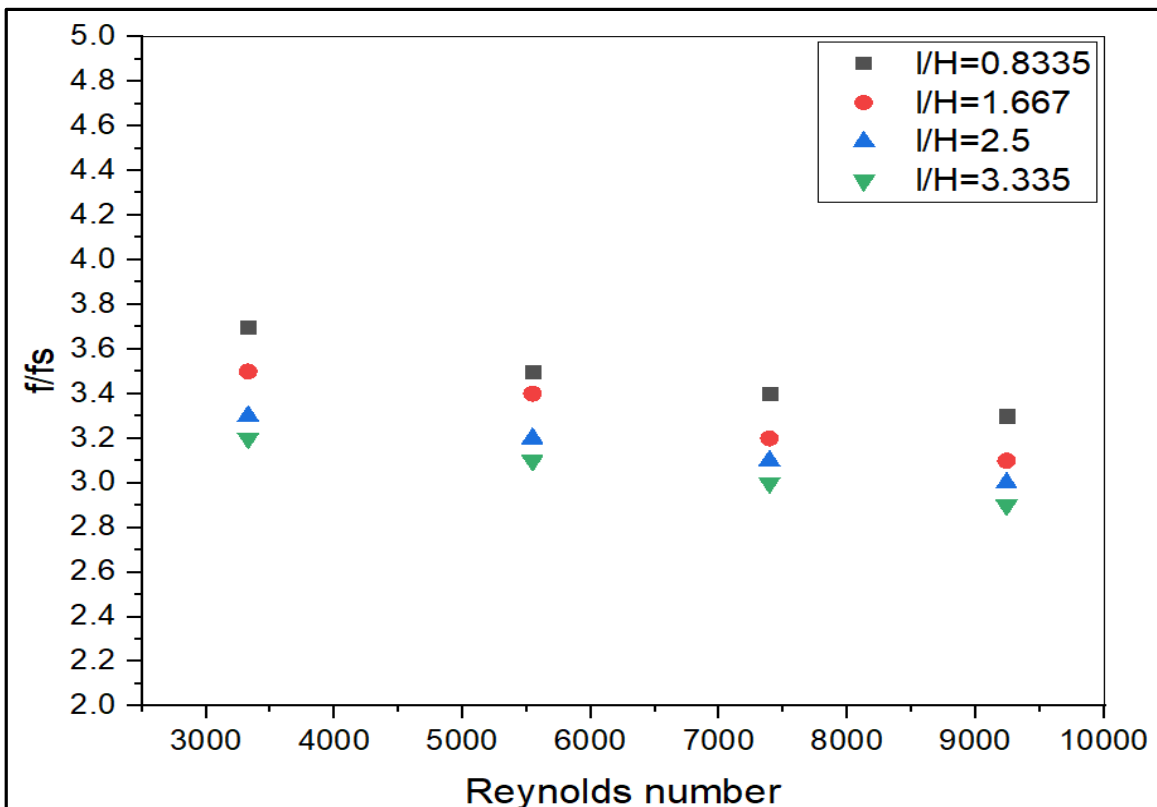
(b)

Figure (5-34 a & b): (a) Influence of p/H on (f / f s) ratio. (b) Influence of l/H on (f / f s) foe S-shaped.
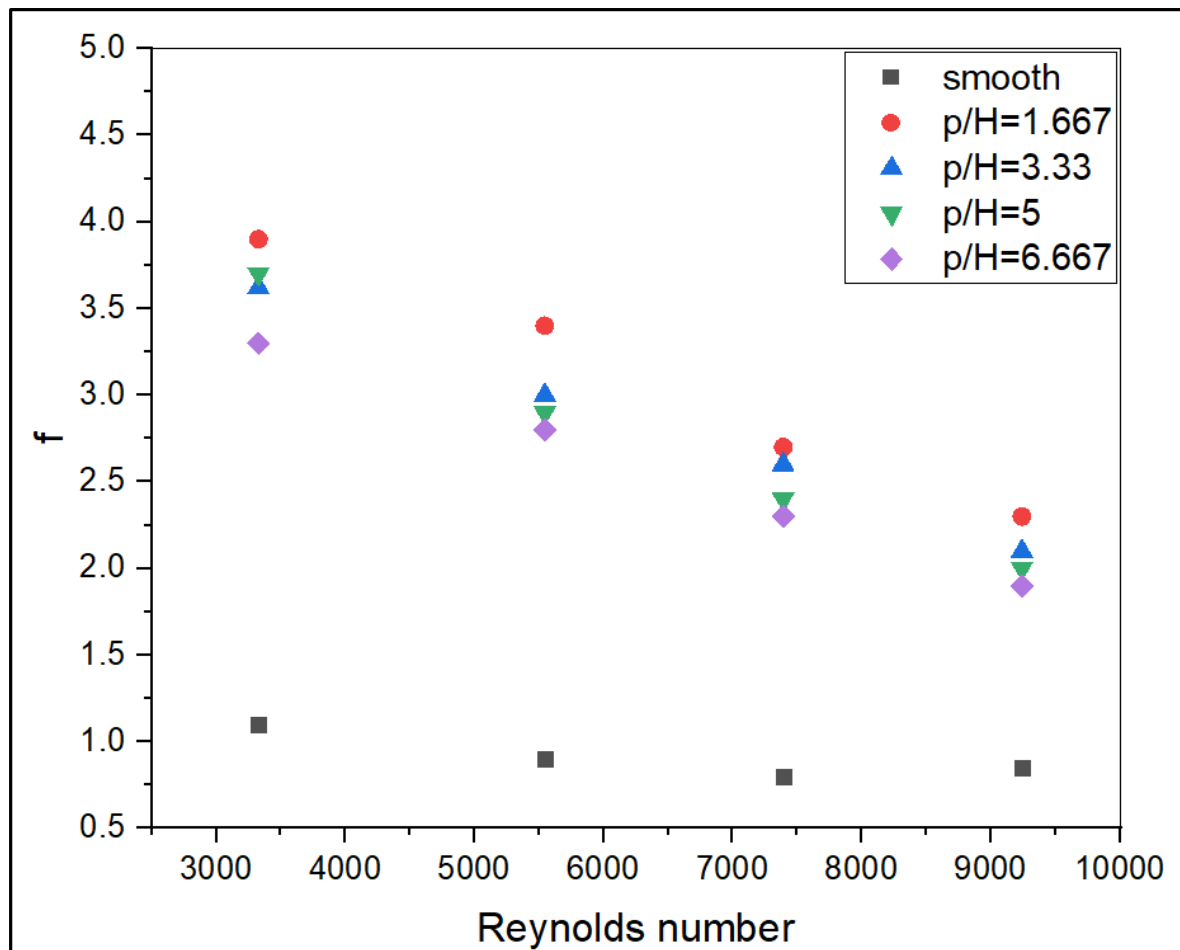
Figure (5-35): f with respect to variation Re for arc-shape inline arrangement.

Figure (5-36) shows the plot of the mean f versus Re for different values of l/H and for constant angle of attack 60°and e/H with a value of 0.271 for the arc-shaped staggered arrangements. Moreover, it has been discovered that the f decreases with an increasing of l/H. The f ratio enhancement with a maximum of 4.1 is found for l/H = 0.8335 and at Re (3323). The number of discontinuities in the flow path over the absorber plate decreases as the l/H increases for a given value of the l/H. It happens because the SAH duct has lower l/H, which results in lower flow resistance in the duct.
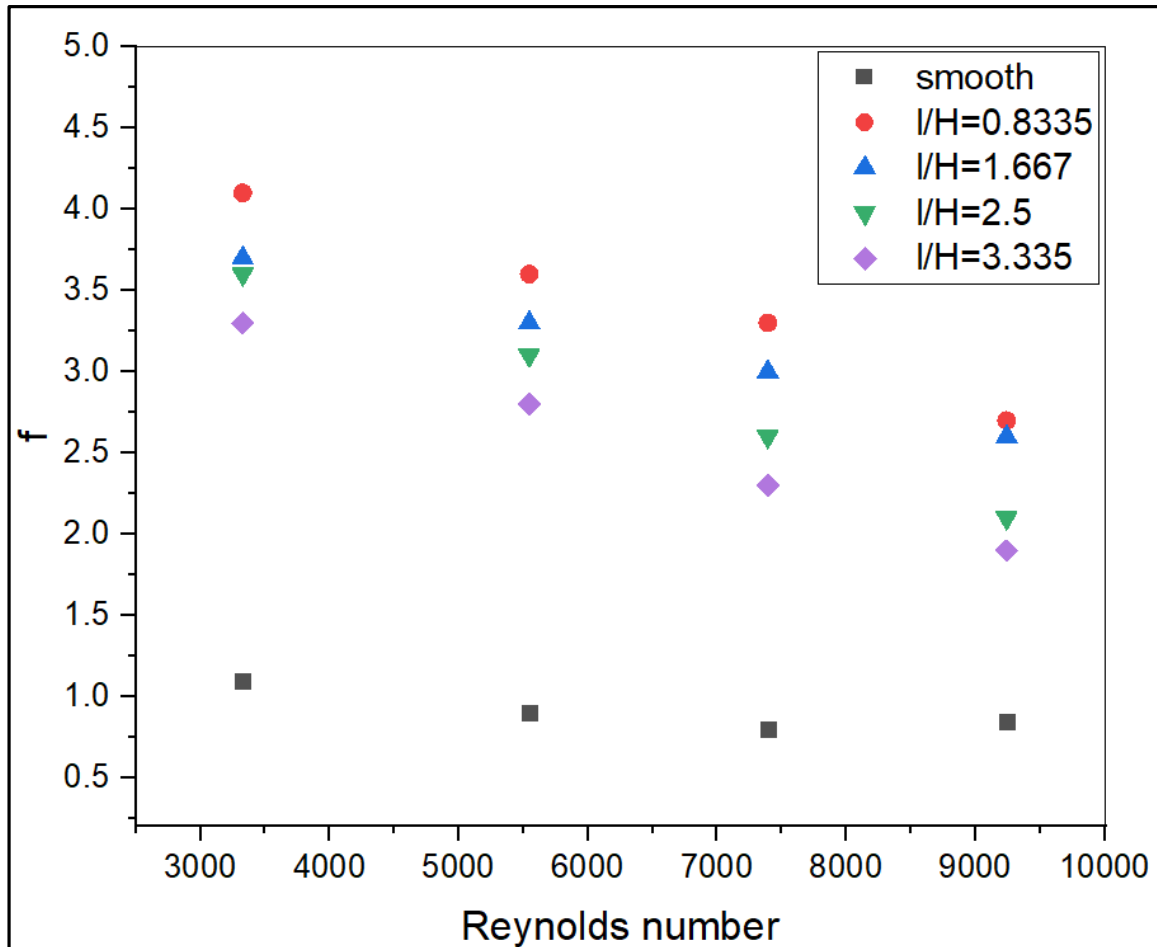
Figure (5-36): f with respect to variation Re for arc-shape staggered arrangement.

Figure (5-37 a & b) shows the plot of the friction factor ratio versus Re for different values of p/H and l/H for e/H with a fixed value of e/H= 0.271 and for a 60° angle of attack, constant values for the arc-shaped inline and staggered arrangements. Figure shown that the f ratio decreases with an increasing of p/H, shown in figure (a), and l/H, shown in figure (b). The f ratio enhancement with a maximum of 3.9 is found for l/H = 0.8335 and 3.7 is found for p/H = 1.667 at Reynolds No. 3323. The number of discontinuities in the flow path over the absorber plate decreases as the p/H increases for a given value of the e/H. It happens because the SAH channel has lower p/H, which results in lower flow resistance in the duct.
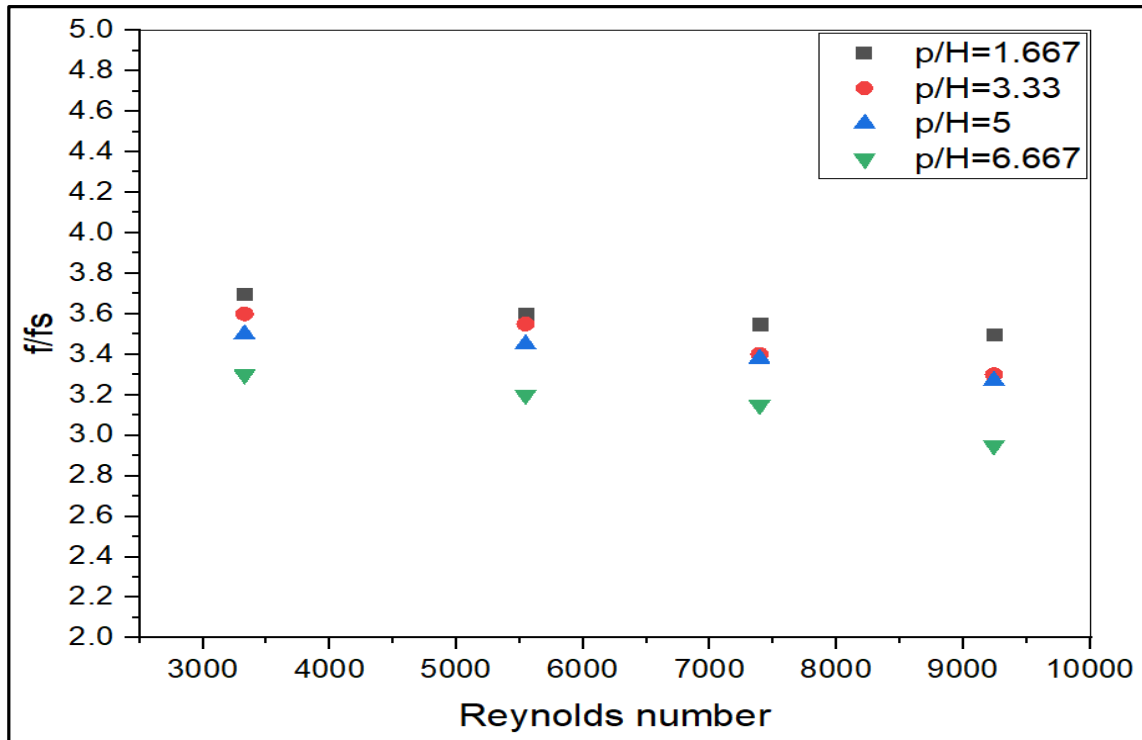
(a)
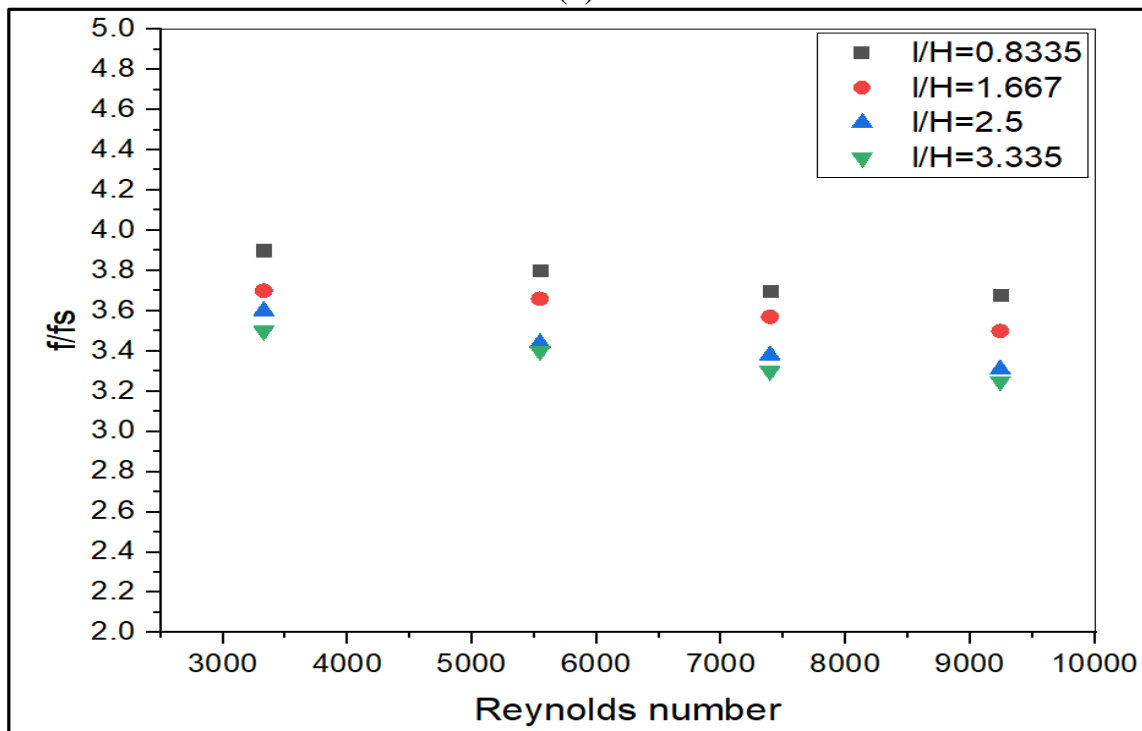
(b)

Figure (5-37 a & b): (a) Effect of p/H on friction factor ratio. (b) Effect of l/H on friction factor ratio

5.9 Thermal performance factor (TPF)

The thermal performance factor it is the ratio of heat transfer and friction factor relative to the smooth case. It also helps to know the optimum arrangement and dimensions of the synthetic roughness, which will correspond to the maximum improvement in heat transfer and minimum frictional force. The change in the thermal enhancement factor with Re is due to the use of the synthetic roughness in arc-shape and S-shape on the absorbent plate.

Figure (5-38) shows the variation of the thermal performance factor with the Re for different values of the (p/H) and for the fixed value of the (l/H=1.667) for the 60° angle of attack fixed values for S-shaped inline. Determine the TPF according to the measured Nu and f values data for both the artificial roughness and the flat plate channel with the same pumping power as defined in the equation (4.11). It was found that the values of thermal performance factor vary from 1.89 to 2.81 for the range of parameters examined. It is noted that the thermal performance factor of the p/H = 3.33 is TPF=2.81 enhanced for the range of parameters examined at the Re of 9241.

Figure (5-39) shows the differences in TPF as a function of Re for all l/H studied. It is noted that the gradient arrangement provides a high f and a high Nu, and thus the values of the thermal performance factor are better. The TPF range of the S-shaped roughness staggered arrangement of the solar air heater is 2.1–3.13. The highest TPF is observed with the S-staggered roughness at l/H = 1.667 of value 3.13, At the Reynolds number of 9241, is the best improved for the variety of variables investigated.
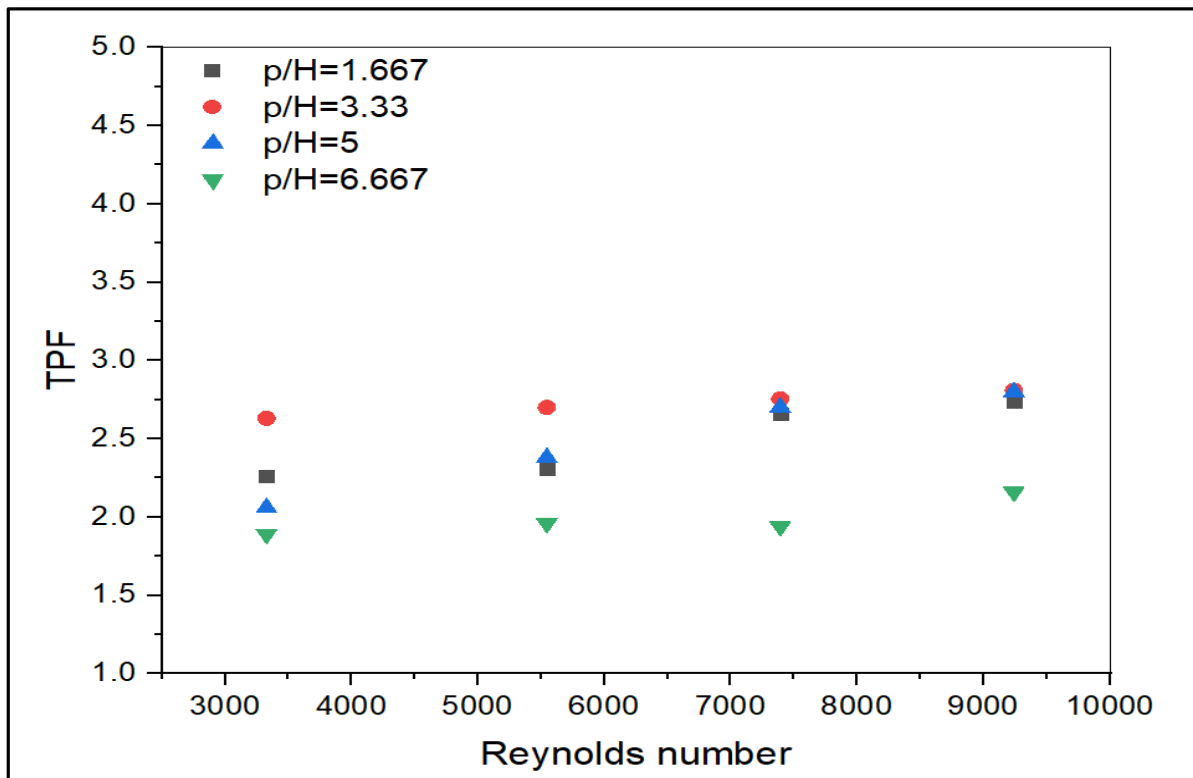
Figure (5-38) TPF variation with Re for different p/H at l/H=1.667 for S-shape inline
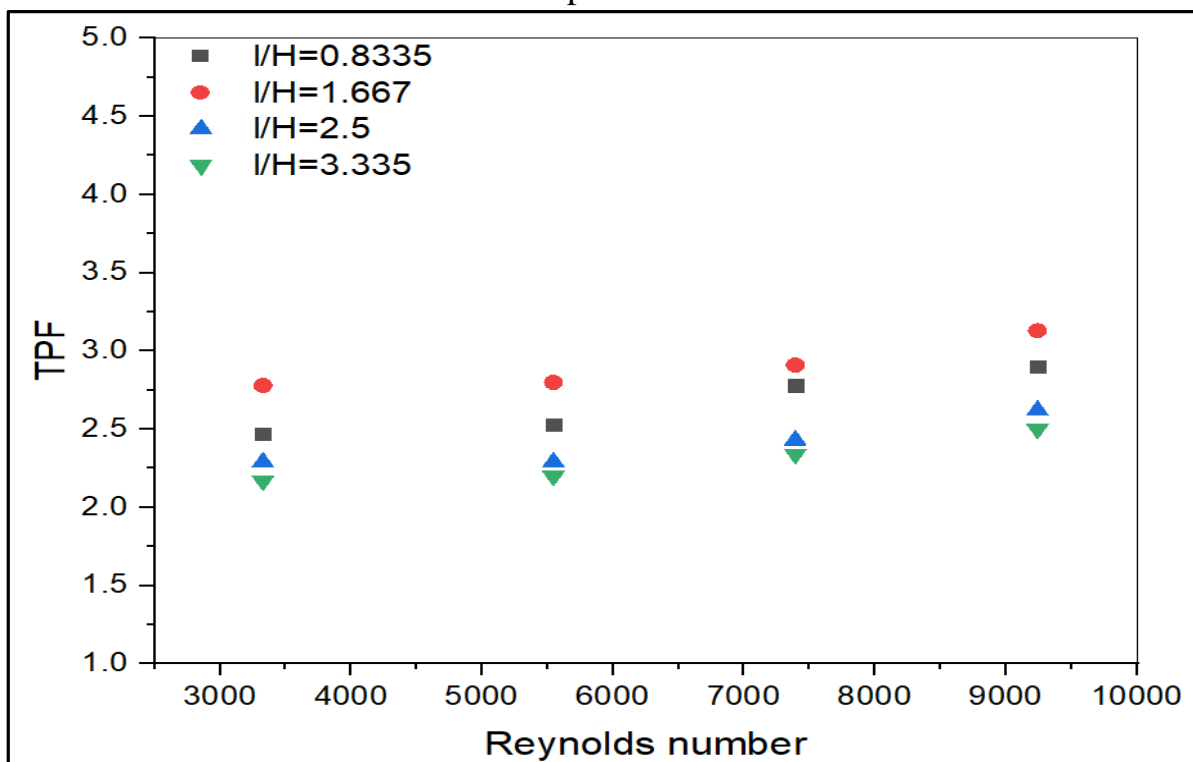
Figure (5-39): TPF variation with Re for different l/H at p/H=3.33 for S-shape

staggered.

The variation of the thermal performance factor with the Reynolds number is shown in Figure (5-40) considering the shape of the inline arc arrangements on the absorber plate alone. A similar pattern of increase in TPF is seen with the Re in the case of an inline rib arrangement. As it was drawn in the figure, the use of arc shape roughness increases heat transfer rate with less friction factor penalty. The improvement using the vortex generator in the arc-shape inline arrangement was found to be 3.38.
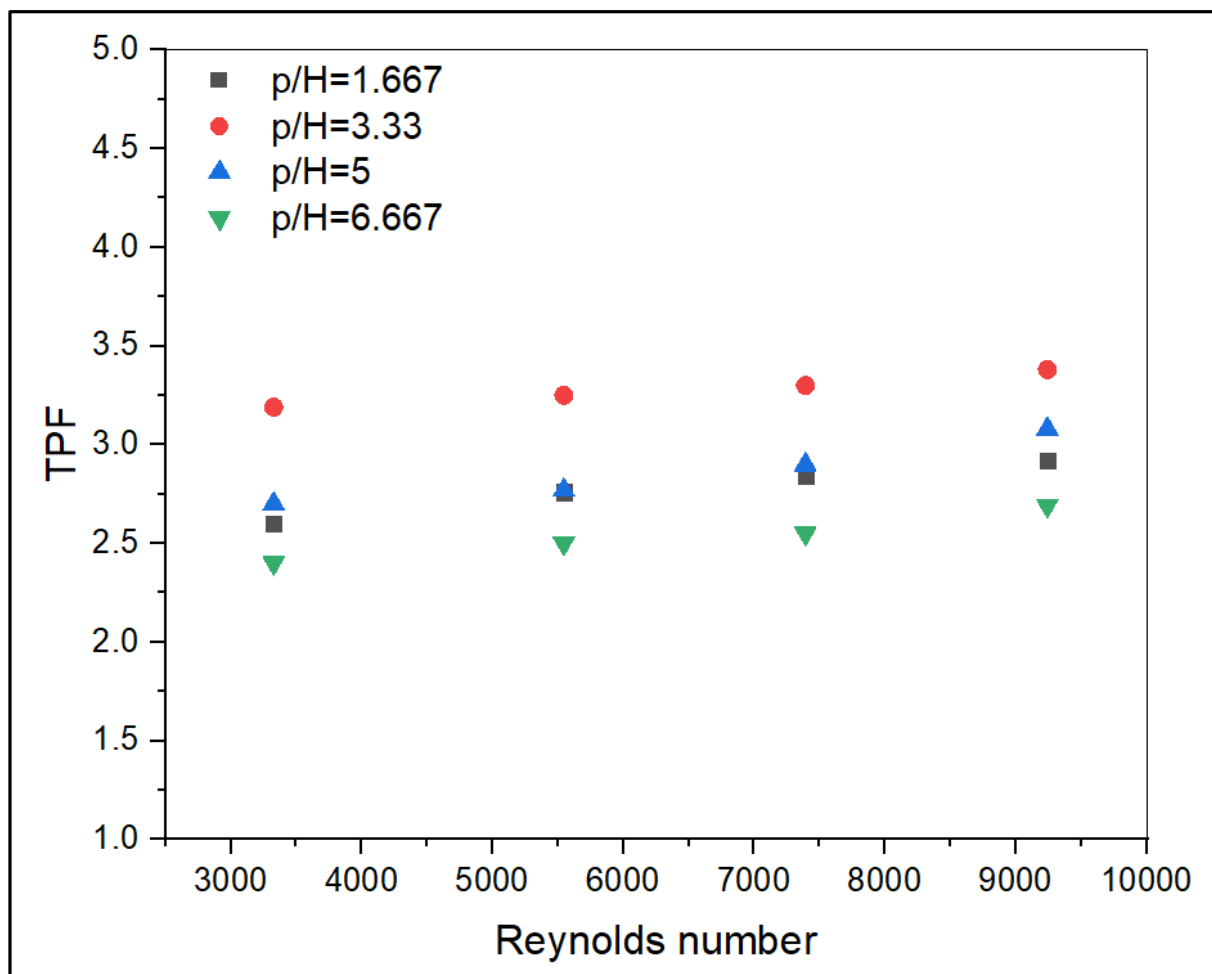
Figure (5-40): TPF variation with Re for different p/H at l/H=1.667 for arc-shape inline.

Figure (5-41) illustrates the relationship between the thermal performance factor and Reynolds number for arc-shaped staggered arrangements. The figure depicts the thermal performance factor of a various relative roughness pitch for Re ranging (3000 - 10000), the use of additional roughness in the staggered arc shape of the heat transfer rate while minimizing the friction factor. Maximum overall performance gain is achieved with the arc-shaped staggered array at Re = 9241 and a TPF value of 3.67.
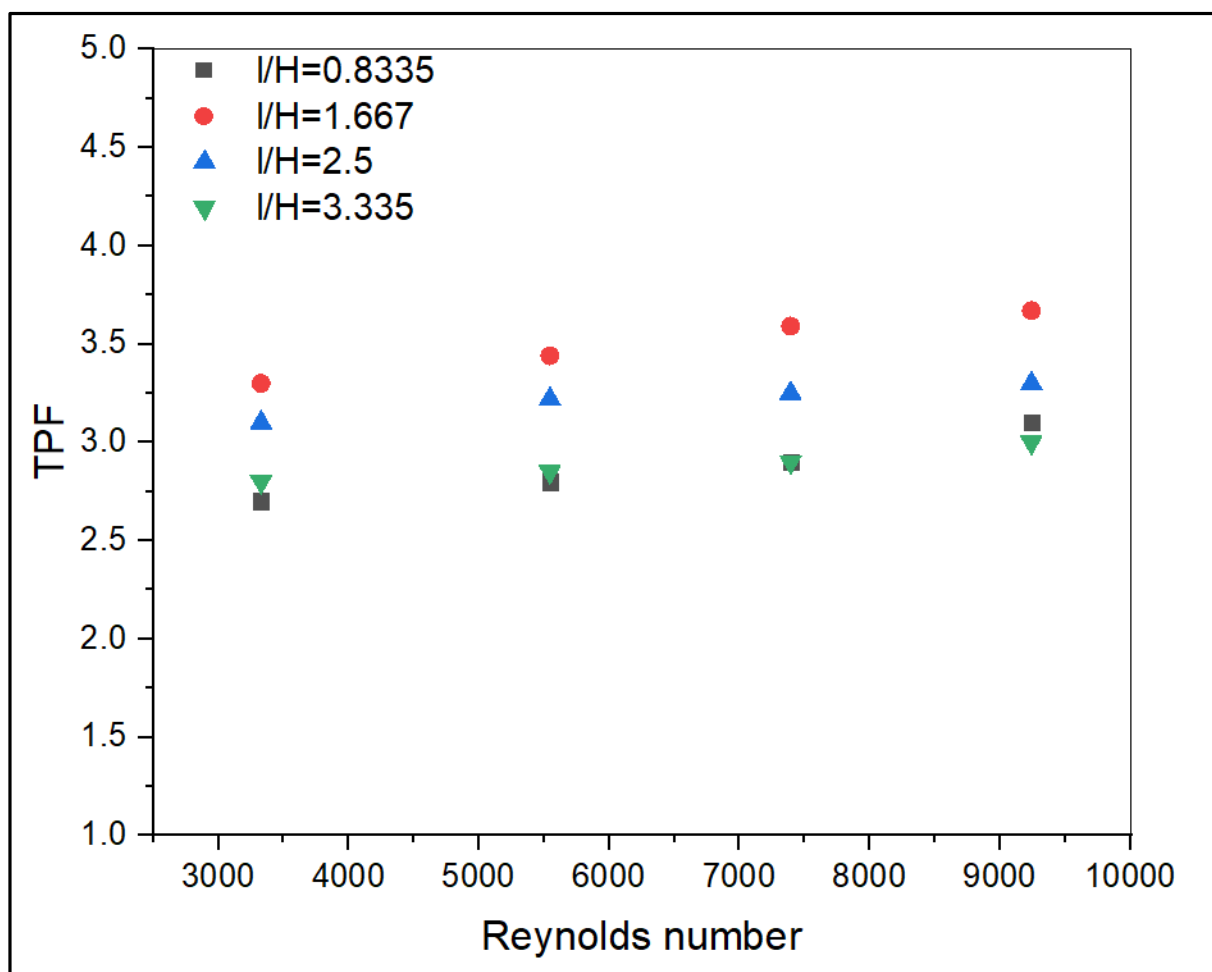
Figure (5-41): TPF variation with Re for different l/H at p/H=3.33 for arc-shape staggered.

115

5.10 Collector efficiency η

Figure (5-42) shows the contrast between efficiency and Reynolds number, where the figure shows the effect of artificial roughness in arc shapes and S in the arrangement of the inline and staggered, where the maximum capacity of efficiency appears at l/H = 1.66 for the arc-shaped staggered arrangement, where the maximum efficiency is found by η =74.5%. Where the improvement in heat transfer is higher than the increase in the factor of intercession and thus leads to increased efficiency.
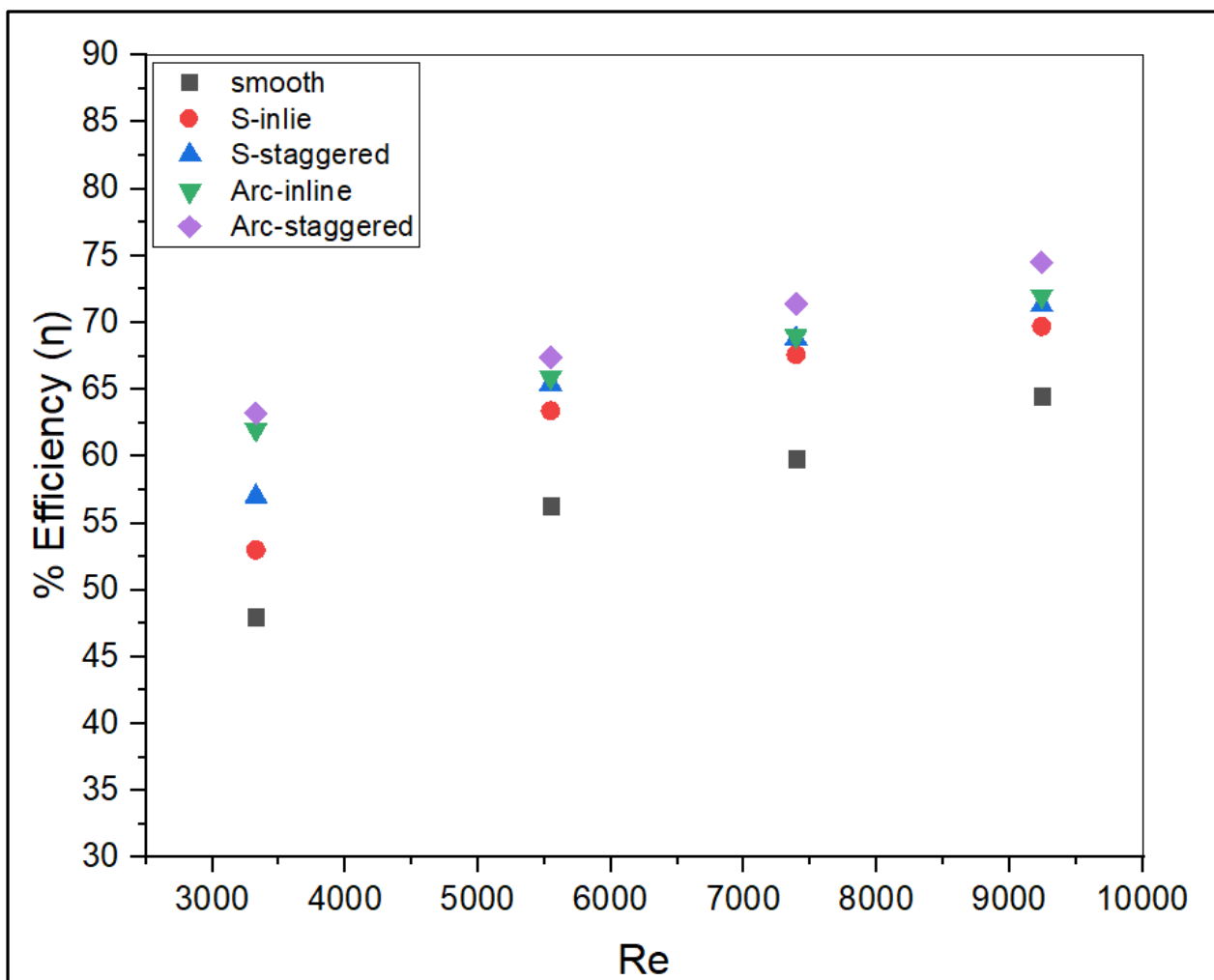
Figure (5-42): The efficiency of SAH variation with Re for l/H=1.667 for S and Arc shape inline and p/H=3.33 for S and Arc-shape staggered.

Chapter Six

Consultation and Recommendations

CHAPTER SIX

6.1 Conclusion

The experimental and numerical study of the thermal performance of a SP-SAH with and in the presence of artificial roughness in the form of an arc and S-shape provides the basis for the conclusion of the present work. Based on the average Nusselt number (Nu) and average friction factor (f) parameters, the ideal artificial roughness shape was determined using the ANSYS FLUENT version 17 Academics platform. From this research, the following conclusions may be drawn:

1. SAH is improve by creating a rough surface on the absorbent plate in the shape of a staggered and inline S and an arc.

2. The average Nusselt number tends to increase as the Reynolds number increases in all cases. The average Nusselt number tends to decrease as the relative roughness pitch increases for a fixed value of relative roughness height and it also tends to increase as the relative roughness height increases for a fixed value of relative roughness pitch.

3. The RNG k-ε turbulence model accurately predicted experimental outcomes, providing confidence in the CFD analysis predictions made in this study. Validation of the k-e perturbed RNG model for a smooth duct.

4. Due to the creation of vortices, the Nusselt number (Nu) and the friction factor (f) increase towards the leading edge of the artificial roughness and drop near the trailing edge due to fluid reconnection.

5. Arc staggered configuration has generated a maximum Nusselt number ratio (Nu/Nus) of 7.65 at Re = 9241 and l/H = 1.667. The S-shaped lining has been seen to have a minimum (Nu/Nus) of 3.2 at p/H 1.667 and Re=3327.

6. The highest value that can be obtained for (f/fs) at Re=9241 is 4.94 and lowest value is obtained by 3.2 at l/H =1.667 for arc shape staggered and l/H =2.5 for S-shape staggered, respectively.

7. When examining all cases for all arc and S-shapes and the effect of the pitch on thermal enhancement, it was determined that p/H=3.33 yields the best results.

8. The greatest value of TPF was obtained at the staggered arc shape of 3.67 at Re=9241 at l/H=1.667.

9. the maximum capacity of efficiency appears at l/H = 1.66 for the arc-shaped staggered arrangement, where the maximum efficiency is found by η =74.5%.

6.2 Recommendations

Several aspects of the Solar Air Heater with artificial roughness could benefit from additional research.

1. Study the effect of using double glass on the enhancement of heat transfer across solar heater.

2. In the future study, can integrating a solar air heater with artificial roughness with thermal storage and analyzing the results.

3. Using the same apparatus and parameter to investigation different shapes of artificial roughness with different arrangement.

4. For further studies on improving the thermal performance of solar air heaters, the effects of the combination of these two considered S and Arc shape here as well as the creating holes in these shapes to reduce pressure drop on heat-transfer enhancement can be studied experimentally and numerically.

References

[1]   K. Hasan, W. Abd al-wahid, and H. Khwayyir, "Flashback and combustion stability in swirl burners: review paper," *IOP Conf. Ser. Mater. Sci. Eng.*, vol. 928, p. 22045, Nov. 2020, doi: 10.1088/1757-899X/928/2/022045.

[2]   M. Of and H. Education, "STUDY OPERATION OF STEAM GENERATION SYSTEM USING DIFFERENT FUELS Asst . Prof . Dr . Wisam A . Abd Al-Wahid June 2020 Lecturer . Dr . Hasan Hadi Salman," 2020.

[3]   K. S. Hasan, H. H. S. Khwayyir, and W. A. Abd Al-wahid, "EXPERIMENTAL INVESTIGATION OF THE FLAME STABILITY MAP (OPERATING WINDOW) BY USING A TANGENTIAL SWIRL BURNER FOR THE CONFINEMENT AND UNCONFINEMENT SPACE," *IOP Conf. Ser. Mater. Sci. Eng.*, vol. 928, no. 2, p. 22016, 2020, doi: 10.1088/1757-899X/928/2/022016.

[4]   A. Yousif, "An Effect of Orientation on Heat Transfer Characteristic from Triangular Cylinder by Using Winglets," *Int. J. Mech. Prod. Eng. Res. Dev.*, vol. 9, pp. 119–131, Jan. 2019, doi: 10.24247/ijmperdfeb201913.

[5]   A. H. Yousif and M. R. Khudhair, "Enhancement heat transfer in a tube fitted with passive technique as twisted tape insert-A comprehensive review," *Am. J. Mech. Eng.*, vol. 7, no. 1, pp. 20–34, 2019.

[6]   A. Yousif, "Numerical analysis for Flow and Heat Transfer in New Shapes Of Corrugated Channels," *J. Babylon Univ. Sci.*, vol. 23, Jan. 2015.

[7]   S. A. Kalogirou, *Solar energy engineering: processes and systems*. Academic press, 2013.

[8] M. Willrich, *Energy & world politics*. Simon and Schuster, 1978.

[9] S. P. Sukhatme and J. K. Nayak, *Solar energy*. McGraw-Hill Education, 2017.

[10] S. Sharma, R. K. Das, and K. Kulkarni, "Performance evaluation of solar air heater using sine wave shape obstacle," in *Current Advances in Mechanical Engineering*, Springer, 2021, pp. 541–553.

[11] T. Zhu, Y. Diao, Y. Zhao, and C. Ma, "Performance evaluation of a novel flat-plate solar air collector with micro-heat pipe arrays (MHPA)," *Appl. Therm. Eng.*, vol. 118, pp. 1–16, 2017.

[12] J. A. Duffie and W. A. Beckman, *Solar Engineering of Thermal Processes*, 2nd ed. New York: John Wiley & Sons, 1991.

[13] H. Öztop, F. Bayrak, and A. Hepbasli, "Energetic and exergetic aspects of solar air heating (solar collector) systems," *Renew. Sustain. Energy Rev.*, vol. 21, pp. 59–83, May 2013, doi: 10.1016/j.rser.2012.12.019.

[14] M. M. Sahu and J. L. Bhagoria, "Augmentation of heat transfer coefficient by using 90 broken transverse ribs on absorber plate of solar air heater," *Renew. energy*, vol. 30, no. 13, pp. 2057–2073, 2005.

[15] R. P. Saini and J. Verma, "Heat transfer and friction factor correlations for a duct having dimple-shape artificial roughness for solar air heaters," *Energy*, vol. 33, no. 8, pp. 1277–1287, 2008.

[16] T. Alam and M.-H. Kim, "Heat transfer enhancement in solar air heater duct with conical protrusion roughness ribs," *Appl. Therm. Eng.*, vol. 126, pp. 458–469, 2017.

[17] H. K. Ghritlahre, P. K. Sahu, and S. Chand, "Thermal performance and heat transfer analysis of arc shaped roughened solar air heater–An

experimental study," *Sol. Energy*, vol. 199, pp. 173–182, 2020.

[18] G. Zhou and Q. Ye, "Experimental investigations of thermal and flow characteristics of curved trapezoidal winglet type vortex generators," *Appl. Therm. Eng.*, vol. 37, pp. 241–248, 2012.

[19] A. S. Yadav and J. L. Bhagoria, "A numerical investigation of square sectioned transverse rib roughened solar air heater," *Int. J. Therm. Sci.*, vol. 79, pp. 111–131, 2014.

[20] K. Kumar and A. Debbarma, "Performance Investigation of Sinusoidal Corrugated Absorber Plate Solar Air Heater," in *Journal of Physics: Conference Series*, 2022, vol. 2178, no. 1, p. 12014.

[21] F. Chabane, N. Moummi, and S. Benramache, "Experimental study of heat transfer and thermal performance with longitudinal fins of solar air heater," *J. Adv. Res.*, vol. 5, no. 2, pp. 183–192, 2014.

[22] S. Skullong, C. Thianpong, and P. Promvonge, "Effects of rib size and arrangement on forced convective heat transfer in a solar air heater channel," *Heat Mass Transf.*, vol. 51, no. 10, pp. 1475–1485, 2015.

[23] S. Skullong, P. Promvonge, C. Thianpong, and M. Pimsarn, "Thermal performance in solar air heater channel with combined wavy-groove and perforated-delta wing vortex generators," *Appl. Therm. Eng.*, vol. 100, pp. 611–620, 2016.

[24] P. Singh and S. Ekkad, "Experimental study of heat transfer augmentation in a two-pass channel featuring V-shaped ribs and cylindrical dimples," *Appl. Therm. Eng.*, vol. 116, pp. 205–216, 2017.

[25] R. S. Gill, V. S. Hans, and S. Singh, "Investigations on thermo-hydraulic performance of broken arc rib in a rectangular duct of solar air heater,"

Int. Commun. Heat Mass Transf., vol. 88, pp. 20–27, 2017.

[26] I. Singh and S. Singh, "CFD analysis of solar air heater duct having square wave profiled transverse ribs as roughness elements," *Sol. Energy*, vol. 162, pp. 442–453, 2018.

[27] A. Kumar and A. Layek, "Nusselt number and friction factor correlation of solar air heater having twisted-rib roughness on absorber plate," *Renew. energy*, vol. 130, pp. 687–699, 2019.

[28] P. Promvonge and S. Skullong, "Heat transfer in solar receiver heat exchanger with combined punched-V-ribs and chamfer-V-grooves," *Int. J. Heat Mass Transf.*, vol. 143, p. 118486, 2019.

[29] P. Promvonge, P. Tongyote, and S. Skullong, "Thermal behaviors in heat exchanger channel with V-shaped ribs and grooves," *Chem. Eng. Res. Des.*, vol. 150, pp. 263–273, 2019.

[30] A. Khanlari *et al.*, "Experimental and numerical study of the effect of integrating plus-shaped perforated baffles to solar air collector in drying application," *Renew. Energy*, vol. 145, pp. 1677–1692, 2020.

[31] C.-E. Bensaci, A. Moummi, F. J. S. de la Flor, E. A. R. Jara, A. Rincon-Casado, and A. Ruiz-Pardo, "Numerical and experimental study of the heat transfer and hydraulic performance of solar air heaters with different baffle positions," *Renew. Energy*, vol. 155, pp. 1231–1244, 2020.

[32] D. Wang, J. Liu, Y. Liu, Y. Wang, B. Li, and J. Liu, "Evaluation of the performance of an improved solar air heater with 'S' shaped ribs with gap," *Sol. Energy*, vol. 195, pp. 89–101, 2020.

[33] M. T. Baissi, A. Brima, K. Aoues, R. Khanniche, and N. Moummi, "Thermal behavior in a solar air heater channel roughened with delta-

shaped vortex generators," *Appl. Therm. Eng.*, vol. 165, p. 113563, 2020.

[34] Y. Mahanand and J. R. Senapati, "Thermal enhancement study of a transverse inverted-T shaped ribbed solar air heater," *Int. Commun. Heat Mass Transf.*, vol. 119, p. 104922, 2020.

[35] H. Olfian, A. Zabihi Sheshpoli, and S. S. Mousavi Ajarostaghi, "Numerical evaluation of the thermal performance of a solar air heater equipped with two different types of baffles," *Heat Transf.*, vol. 49, no. 3, pp. 1149–1169, 2020.

[36] S. Eiamsa-ard, A. Phila, K. Wongcharee, M. Pimsarn, N. Maruyama, and M. Hirota, "Thermal evaluation of flow channels with perforated-baffles," *Energy Reports*, vol. 9, pp. 525–532, 2023, doi: https://doi.org/10.1016/j.egyr.2023.01.064.

[37] P. Promvonge *et al.*, "Effect of arc-shaped twisted-baffles on augmented heat transfer in a rectangular duct," *Case Stud. Therm. Eng.*, vol. 42, p. 102754, 2023, doi: https://doi.org/10.1016/j.csite.2023.102754.

[38] V. B. Gawande, A. S. Dhoble, and D. B. Zodpe, "CFD analysis to study effect of circular vortex generator placed in inlet section to investigate heat transfer aspects of solar air heater," *Sci. World J.*, vol. 2014, 2014.

[39] T. Alam and M.-H. Kim, "Numerical study on thermal hydraulic performance improvement in solar air heater duct with semi ellipse shaped obstacles," *Energy*, vol. 112, pp. 588–598, 2016, doi: https://doi.org/10.1016/j.energy.2016.06.105.

[40] A. D. Gupta and L. Varshney, "Performance prediction for solar air heater having rectangular sectioned tapered rib roughness using CFD," *Therm. Sci. Eng. Prog.*, vol. 4, pp. 122–132, 2017, doi: https://doi.org/10.1016/j.tsep.2017.09.005.

[41] T. L. Bergman, T. L. Bergman, F. P. Incropera, D. P. Dewitt, and A. S. Lavine, *Fundamentals of heat and mass transfer*. John Wiley & Sons, 2011.

[42] C. K. G. Lam and K. Bremhorst, "A Modified Form of the k-ε Model for Predicting Wall Turbulence," *J. Fluids Eng.*, vol. 103, no. 3, pp. 456–460, Sep. 1981, doi: 10.1115/1.3240815.

[43] H. K. Versteeg and W. Malalasekera, *An introduction to computational fluid dynamics: the finite volume method*. Pearson education, 2007.

[44] W. M. Kays, M. E. Crawford, and B. Weigand, *Convective heat and mass transfer*, vol. 4. McGraw-Hill New York, 1980.

[45] Y. A. Çengel and J. M. Cimbala, *Fluid Mechanics: Fundamentals and Applications*. McGraw-Hill Higher Education, 2010.

[46] J. P. Hartnett and W. M. Rohsenow, "Handbook of heat transfer," *Handb. heat Transf.*, 1973.

[47] S. Skullong, S. Kwankaomeng, C. Thianpong, and P. Promvonge, "Thermal performance of turbulent flow in a solar air heater channel with rib-groove turbulators," *Int. Commun. Heat Mass Transf.*, vol. 50, pp. 34–43, 2014.

[48] Varun, R. P. Saini, and S. K. Singal, "Investigation of thermal performance of solar air heater having roughness elements as a combination of inclined and transverse ribs on the absorber plate," *Renew. Energy*, vol. 33, no. 6, pp. 1398–1405, 2008, doi: https://doi.org/10.1016/j.renene.2007.07.013.

[49] A. C. Yunus, *Fluid Mechanics: Fundamentals And Applications (Si Units)*. Tata McGraw Hill Education Private Limited, 2010.

[50] H. Benli, "Experimentally derived efficiency and exergy analysis of a new solar air heater having different surface shapes," *Renew. Energy*, vol. 50, pp. 58–67, 2013, doi: https://doi.org/10.1016/j.renene.2012.06.022.

[51] R. L. Webb, "Performance evaluation criteria for use of enhanced heat transfer surfaces in heat exchanger design," *Int. J. Heat Mass Transf.*, vol. 24, no. 4, pp. 715–726, 1981.

[52] F. P. Incropera, D. P. Dewitt, T. L. Bergman, and A. S. Lavine, "Introduction to Heat Transfer, John Wiley&Sons," *Inc. United States Am.*, pp. 280–284, 1996.

[53] E. M. Sparrow, J. P. Abraham, J. M. Gorman, and W. J. B. T.-A. in H. T. Minkowycz, Eds., "Advances in Heat Transfer," in *Advances in Heat Transfer*, vol. 51, Elsevier, 2019, p. i.

[54] J. Ward-Smith and L. L. Isser, *Mechanics of fluids*. CRC Press, 2005.

[55] M. Murugan, R. Vijayan, A. Saravanan, and S. Jaisankar, "Performance enhancement of centrally finned twist inserted solar collector using corrugated booster reflectors," *Energy*, vol. 168, pp. 858–869, 2019.

Appendices

Appendix (A): Calibration of solar power meter

In this study, a solar power meter was used to measure global solar radiation. This device is used because it is easy to use and has acceptable accuracy. This device can be calibrated, as the Weather Technical College of Najaf, Iraq, to investigate the calibration of the solar power meter, relied on it. As in figure A.1.
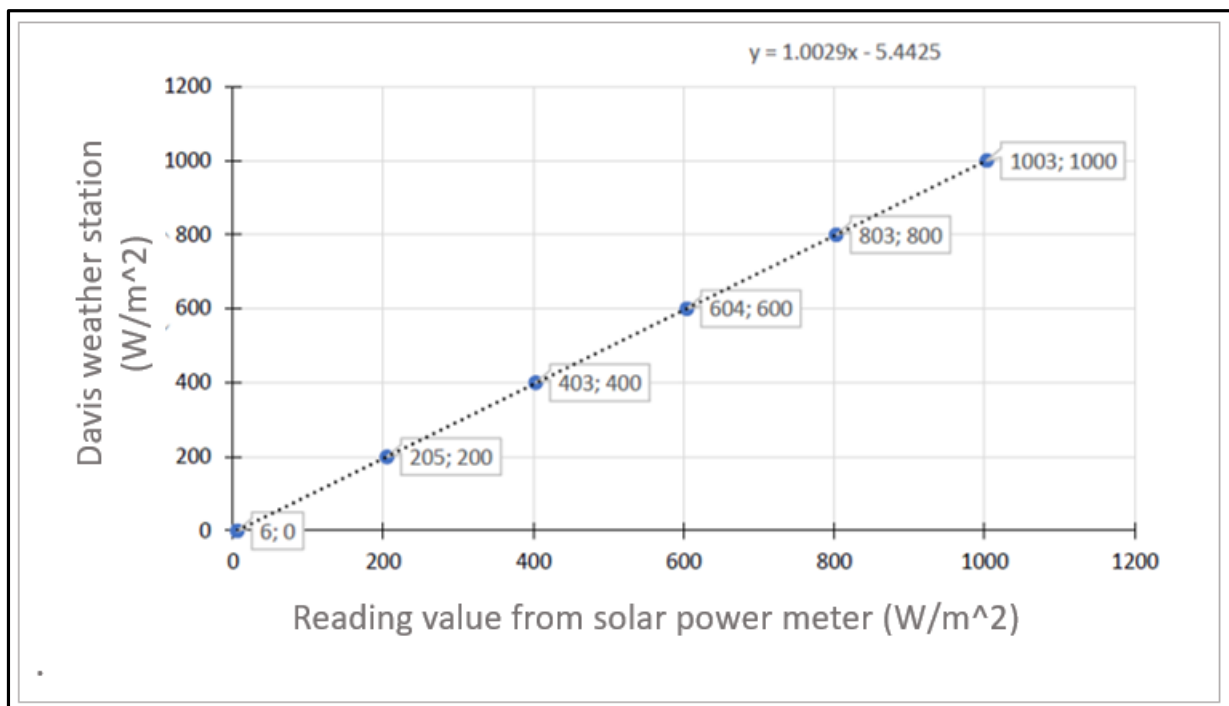
Figure A.1. Solar power meter calibration.

Appendix (B): Calibration of Anemometer

All procedures employ an anemometer to measure wind speed. It is a simple-to-use instrument with an adequate level of precision. The Meteorological Station in Al-Diwaniyah calibrated the anemometer and compared the wind speed measured by the station and the anemometer, with a range of (0.1 to 35) m/s and an accuracy of 5%. As in figure B.1.
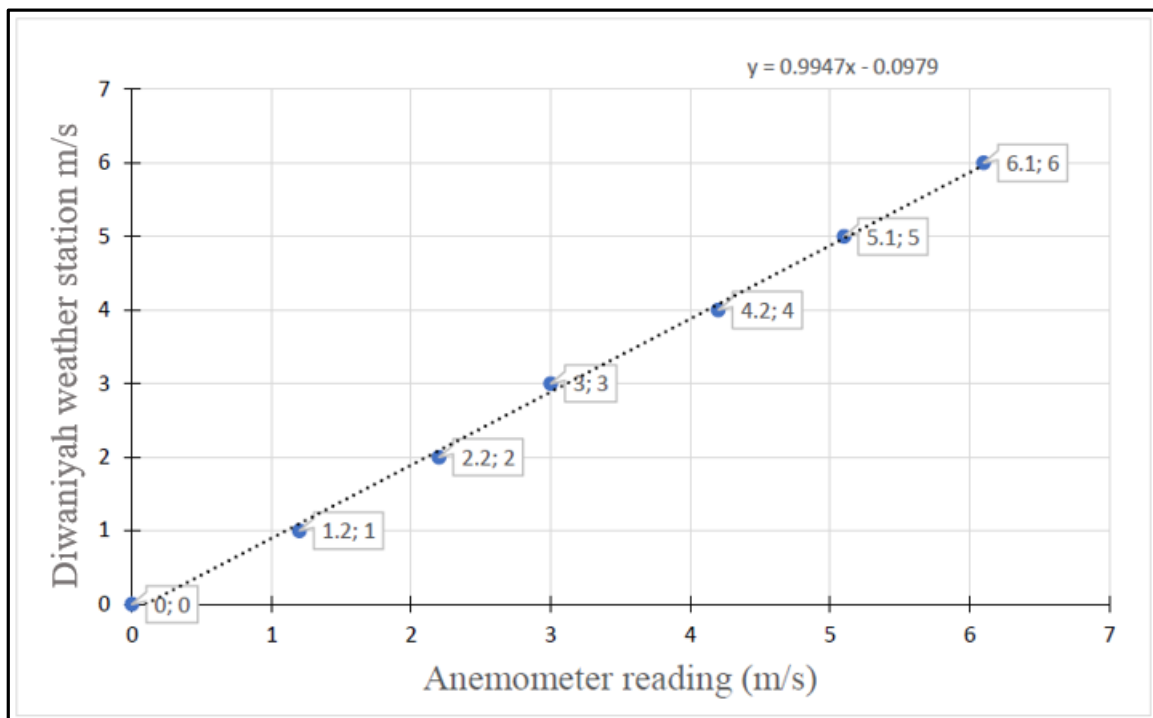
Figure B.1 Anemometer calibration

Appendix (C): Calibration of Thermocouples
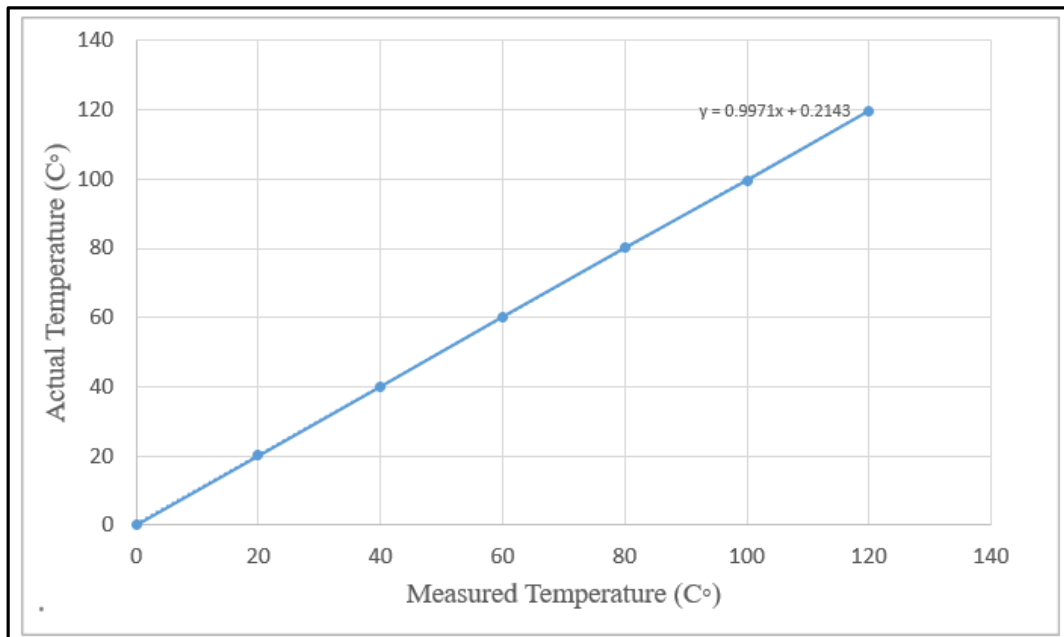
Figure C.1 Calibration of thermocouples

Channel no. Thermocouples	Ice Point (0.0 ° C)	Ambient temperature (38 ° C)	Steam points (100 ° C)
T1	0.3	38.1	99.2
T2	0.2	38.4	98.6
T3	0.4	37.4	98.7
T4	0.6	37.8	99.1
T5	-0.1	37.9	99.6
T6	-0.2	38.1	99.4
T7	0.1	38.2	99.7
T8	0.3	38.4	98.7
T9	0.5	38.6	98.4
T10	0.4	38.1	99.1
T11	0.2	37.8	99.6
T12	0.3	37.4	99.7
T13	0.2	37.6	99.6
T14	0.4	37.9	98.7
T15	0.6	38.2	97.9
T16	-0.3	38.21	97.8
T17	-0.1	38.0	98.7
T18	-0.4	38.0	99.8

Appendix (D): Uncertainty

Verification of Uncertainty the following relationship can be used to indicate a possible error value in the measurement tools: A related formula between the dependent and independent variables can be used to figure out the resultant uncertainty value [55].

$$Y_R = \sqrt{\Sigma_0^i \left(\frac{\partial R}{\partial Z_i} \cdot Y_{Zi}\right)^2} \qquad (D.1)$$

$$R = f(Z_1, Z_2, \ldots, Z_n) \qquad (D.2)$$

Where:

Y_R: Uncertainty regarding the results

$Z_1, Z_2, \ldots, Z_n$: Independent factors

$Y_1, Y_2, \ldots, Y_n$: Associated variables.

In the following sections, the general formula to be employed to assess the uncertainty of the experimentally obtained performance analysis in the current study. (D.1).

Area of the absorber plate (Ap)

The Area of the absorber plate (Ap) was obtained by eq. follow and rewritten below:

$$Ap = W \times L \qquad (D.3)$$

The uncertainty in Ap is attributable to mistakes in W width and L length, according to Eq. (C.1). However, the following broad statement could be create:

$$\delta Ap = \left[\left(\frac{\delta Ap}{\delta L} \delta L\right)^2 + \left(\frac{\delta Ap}{\delta W} \delta W\right)^2\right]^{0.5} \qquad (D.4)$$

$$\delta Ap = [(W\ \delta L)^2 + (L\ \delta W)^2]^{0.5} \tag{D.5}$$

$$\frac{\delta Ap}{Ap} = \left[\left(\frac{W\ \delta L}{W\ L}\right)^2 + \left(\frac{L\ \delta W}{W\ L}\right)^2\right]^{0.5} \tag{D.6}$$

$$\frac{\delta Ap}{Ap} = \left[\left(\frac{\delta L}{L}\right)^2 + \left(\frac{\delta W}{W}\right)^2\right]^{0.5} \tag{D.7}$$

$$\frac{\delta Ap}{Ap} = \left[\left(\frac{\delta L}{L}\right)^2 + \left(\frac{\delta W}{W}\right)^2\right]^{0.5} \tag{D.8}$$

$$\frac{\delta Ap}{Ap} = \left[\left(\frac{1}{1200}\right)^2 + \left(\frac{0.05}{300}\right)^2\right]^{0.5} = \pm 0.000849 = 0.0489\%$$

Hydraulic diameter (D_h)

The Hydraulic diameter (D_h) was obtained by eq.(4.7) follow and rewritten below:

$$D_h = \frac{2ab}{a+b} \tag{D.9}$$

$$\delta D_h = \left[\left(\frac{\delta D}{\delta H}\ \delta H\right)^2 + \left(\frac{\delta D}{\delta W}\ \delta W\right)^2\right]^{0.5} \tag{D.10}$$

$$\frac{\delta D_h}{D_h} = \frac{\left[\left(\frac{\delta D}{\delta H}\ \delta H\right)^2 + \left(\frac{\delta D}{\delta W}\ \delta W\right)^2\right]^{0.5}}{2(W\ H)(W+H)^{-1}} \tag{D.11}$$

$$\frac{\delta D_h}{D_h} = \frac{[(1.652\times0.05)^2 + (1.652\times0.05)^2]^{0.5}}{2(300\times30)(300+30)^{-1}} = \pm 0.00214\ or\ 0.214\% \tag{D.12}$$

Mass flow rate ($\dot{m}$)

The mass flow rate ($\dot{m}$) was compute using eq. (4.12) follow and rewritten below:

$$\dot{m} = \rho\ VAp \tag{D.13}$$

$$\frac{\delta \dot{m}}{\dot{m}} = \left[\left(\frac{\delta\rho}{\rho}\right)^2 + \left(\frac{\delta V}{V}\right)^2 + \left(\frac{\delta Ap}{Ap}\right)^2\right]^{0.5} \tag{D.14}$$

$$\frac{\delta \dot{m}}{\dot{m}} = [(0.0083)^2 + (0.0186)^2 + (0.000849)^2]^{0.5} = \pm 0.0004155 \qquad \text{(D.15)}$$

Useful heat gain (Q_u)

The Useful heat gain (Qu) was compute using eq. (4.2) follow and rewrite below:

$$Q_{u,air} = \dot{m}C_{p,air}(T_{out} - T_{in}) \qquad \text{(D.16)}$$

$$\frac{\delta Q_{u,air}}{Q_{u,air}} = \left[\left(\frac{\delta \dot{m}}{\dot{m}}\right)^2 + \left(\frac{\delta C_{p,air}}{C_{p,air}}\right)^2 + \left(\frac{\delta \Delta T}{\Delta T}\right)^2\right]^{0.5} \qquad \text{(D.17)}$$

$$\frac{\delta Q_{u,air}}{Q_{u,air}} = \left[(0.000415)^2 + \left(\frac{1}{1006}\right)^2 + \left(\frac{0.25}{5}\right)^2\right]^{0.5} = 0.05001 \; or \; 5\% \qquad (D.18)$$

Hear transfer coefficients (h)

The Hear transfer coefficients (h) was compute using eq. (4.6) follow and rewrite below:

$$h = \frac{\dot{m}C_{p,air}(T_{out} - T_{in})}{A(T_{ap} - T_{am})} \qquad \text{(D.19)}$$

$$\frac{\delta h}{h} = \left[\left(\frac{\delta Q_{u,air}}{Q_{u,air}}\right)^2 + \left(\frac{\delta A_p}{A_p}\right)^2 + \left(\frac{\delta \Delta T}{\Delta T}\right)^2\right]^{0.5} \qquad \text{(D.20)}$$

$$\frac{\delta h}{h} = \left[(0.5)^2 + (0.000849)^2 + \left(\frac{0.25}{5}\right)^2\right]^{0.5} = 0.50249 \; or \; 5.02\% \qquad \text{(D.21)}$$

Nusselt Number (Nu)

The Nusselt number (Nu) was compute using eq. (4.8) follow and rewrite below:

$$Nu = \frac{hD_h}{k} \qquad \text{(D.22)}$$

$$\frac{\delta Nu}{Nu} = \left[\left(\frac{\delta h}{h}\right)^2 + \left(\frac{\delta D_h}{D_h}\right)^2 + \left(\frac{\delta k}{k}\right)^2\right]^{0.5} \qquad \text{(D.23)}$$

$$\frac{\delta Nu}{Nu} = \left[(0.50249)^2 + (0.00214)^2 + \left(\frac{0.00001}{0.02659}\right)^2\right]^{0.5} = 0.50249 \; or \; 5.02\%$$

(D.24)

Reynolds number (Re)

The Reynolds number (Re) was compute using eq. (4.9) follow and rewrite below:

$$Re = \frac{\rho v \, D_h}{\mu}$$

(D.25)

$$\frac{\delta Re}{Re} = \left[\left(\frac{\delta\rho}{\rho}\right)^2 + \left(\frac{\delta D_h}{D_h}\right)^2 + \left(\frac{\delta v}{v}\right)^2 + \left(\frac{\delta\mu}{\mu}\right)^2\right]^{0.5}$$

(D.26)

$$\frac{\delta Re}{Re} = \left[(0.0083)^2 + (0.00214)^2 + (0.0186)^2 + \left(\frac{0.001}{1.81}\right)^2\right]^{0.5} =$$

$0.0204 \; or \; 2.04\%$

(D.27)

Friction factor (f)

The friction factor (f) was compute using eq. (4.10) follow and rewrite below:

$$f = \frac{2}{L/D_h}\frac{\Delta P}{\rho v^2}$$

(D.28)

$$\frac{\delta f}{f} = \left[\left(\frac{\delta\rho}{\rho}\right)^2 + \left(\frac{\delta D_h}{D_h}\right)^2 + \left(\frac{\delta v}{v}\right)^2 + \left(\frac{\delta L}{L}\right)^2 + \left(\frac{\delta\Delta P}{\Delta P}\right)^2\right]^{0.5}$$

(D.29)

$$\frac{\delta f}{f} = \left[(0.0083)^2 + (0.00214)^2 + (2 \times 0.0186)^2 + \left(\frac{1}{1200}\right)^2 + \left(\frac{0.001}{51.86}\right)^2\right]^{0.5} =$$

$0.0381 \; or \; 3.81\%$

(D.30)

Appendix (E): List of Accepted for Publication in Journal

1. Gaith Moneem Fedhala, Ahmed Hashem Yousef "**The effect of artificial roughness on performance of solar air heater (SAH): A review study**" 1st International Conference on Achieving the Sustainable Development Goals (ICASDG-2022), Q4 Scopus Journal.

1st International Conference on Achieving the Sustainable Development Goals
(6th – 7th) June 2022 in Istanbul- Turkey

Final Acceptance Letter

Manuscript Number: 124

Dear: Gaith Moneem Fadala

Co-Authors: Ahmed Hashem Yousef

Congratulations!

It's a great pleasure to inform you that, after the peer review process, your manuscript entitled

(The effect of artificial roughness on performance of solar air heater (SAH): A review study)

had been **ACCEPTED** for participating in the 1st **International Conference on Achieving the Sustainable Development Goals,** and considered for publication in **(AIP Conference proceeding).**

Thank you for your valuable participation in the ICASDG2022 conference.

Prof. Dr. Ahmed G. Wadday
ICASDG2022 Scientific Committee Chair | AIP Conference Proceeding Editor
6th – 7th June 2022 | Istanbul | Turkey

E-1

2. Gaith Moneem Fedhala, Ahmed Hashem Yousef **"Experimental and numerical investigation of Solar Air Heater with rectangular arc-shaped artificial roughness on absorber plate"** 6th International Conference on Engineering Sciences (ICES-2022), Q4 Scopus Journal.

ID-Code: ICES-52
Authors: Gaith Monem Fadala and Ahmed Hashem Yousef
Date: 20/11/2022

Dear Authors,

On behalf of the scientific and organizing committees of the 6th International Conference on Engineering Sciences (ICES 2022), I am pleased to inform you that your manuscript entitled "Experimental and numerical investigation of Solar Air Heater with rectangular arc-shaped artificial roughness on absorber plate." has been accepted for publication in the conference proceedings of ICES2022. The accepted paper will be published in the AIP Conference Proceedings which is indexed in the Scopus Journals database. The 6th ICES will be held on 21-22 December 2022. Thank you for your interest in participating in the 6th ICES.

Best Regards,

Prof. Dr. Laith Sh. Rasheed
Chair of the Organizing Committee -ICES
Dean of Engineering College at Kerbala University

+964-771-5907020   ices@uokerbala.edu.iq   https://sites.google.com/view/ices-2022/home

3. Gaith Moneem Fedhala, Ahmed Hashem Yousef **"Experimental and numerical investigation of Solar Air Heater with rectangular S-shaped artificial roughness on absorber plate"** Journal of Thermal Engineering, Q3 Scopus Journal.

JTEN-2022-434: Your manuscript evaluation period has finished Inbox

Journal of Thermal En...   16 Jan

to me

Journal of Thermal Engineering

Title: Experimental and numerical investigation of Solar Air Heater with rectangular S-shaped artificial roughness on absorber plate

Manuscript Id: JTEN-2022-434
Authors: Gaith Moneem, Gaith Fadhala
Article Type: Research Article

Dear Ms. Gaith Fadhala,

Peer review of your manuscript (above) is now complete and we are delighted to accept the manuscript for publication in **Journal of Thermal Engineering**
Before publication, our production team needs to check the format of your manuscript, to ensure that it conforms to the standards of the journal. They will get in touch with you shortly to request any necessary changes or to confirm that none are needed.

الخلاصة

الطاقة الشمسية واحدة من اهم مصادر الطاقة المتجددة والمستدامة، حيث تعد من مصادر الطاقة النظيفة والصديقة للبيئة ويعد مصدر الاشعاع الشمسي القادم الى الارض واحد من اهم مصادر الطاقة غير قابل للنضوب. ويعد تحويل هذا الاشعاع الى طاقة حرارية واستغلالها في حاجة الارض من طاقة حيث يعد سخان الهواء الشمسي واحد من التطبيقات المهمة في هذا المجال. تمت دراسة الاداء الحراري لسخان شمسي هوائي احادي الممر بوجود وعدم وجود خشونة صناعية عمليا وعدديا باستخدام برنامج ANSYS FLUENT version 17 كان الهدف الرئيسي من هذه الدراسة هو تحسين انتقال الحرارة باستخدام الخشونة الاصطناعية والتي استخدمت نوعين من الخشونة الصناعية (على شكل S وكذألك شكل قوس(وكان ترتيبها على خطي ومتعاكس لإيجاد أفضل نوع وأفضل ترتيب.

تم تصميم المجرى بأبعاد (طول*عرض*ارتفاع) (30 * 300 * 2100) مم. ضمن مدى الرقم رينولدز (10000-2000) وبمقدار وزاوية هجوم ۰ 60 = α كما تم دراسة تـأثير المسافة بين اجزاء الخشونة الصناعية.

في الدراسة العددية تم استخدام برنامج ANSYS FLUENT version 17 لمحاكاة السخان الشمسي الهوائي ضمن خوارزمية البسيطة (SIMPLE) بطريقة الحجوم المحدودة لحل المعادلات ثلاثية الابعاد (الاستمرارية، الطاقة، الزخم) بالإضافة الى معادلات نموذج الاضطراب (k-ε) وضمن نفس الظروف الحدية المستخدمة في الجانب العملي.

تم اجراء التجارب العملية في الجو الحر تحت اشعة الشمس بعد بناء نموذج لجهاز يتم فيع قياس درجات الحرارة الجريان ومقارنة النتائج مع الجانب العددي التي كانت متطابقة بشكل كبير.

اظهرت النتائج ان عدد نسلت يزداد بزيادة رقم رينولدز ومعامل الاحتكاك يقل بزيادة رقم رينولدز حيث تم الحصول على أفضل رقم نسلت Nu/Nus=7.8 عند l/H=1.667 في شكل

القوس بالترتيب المتعاقب وكان معامل الاحتكاك f/fs=3.8. وان الاداء الحراري لهذا الترتيب هو الافضل بمقدار 3.67 بكفاءة مقدارها 74.5%.

جمهورية العراق

وزارة التعليم العالي والبحث العلمي

جامعة الفرات الاوسط التقنية

الكلية التقنية الهندسيةـ نجف

أداء سخان الهواء الشمسي احادي المجرى المستطيل باستخدام خشونة صناعية متعددة الانواع

رسالة مقدمة الى

قسم هندسة تقنيات ميكانيك القوى

كجزء من متطلبات نيل درجة الماجستير في تكنلوجيا الحراريات

في هندسة تقنيات ميكانيك القوى

تقدم بها

غيث منعم فضاله

بكالوريوس هندسة تقنيات السيارات

اشراف

الاستاذ الدكتور

أحمد هاشم يوسف

صفر ١٤٤٤ هـ

141